Charles University in Prague

Faculty of Mathematics and Physics

DOCTORAL THESIS

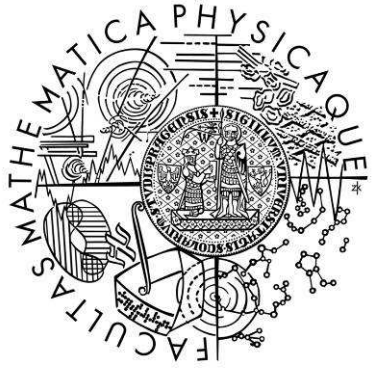

Martin Hanuš

Preparation and optical properties of scintillation oxide layers

Institute of Physics of Charles University

Supervisor of the doctoral thesis: doc. RNDr. Miroslav Kučera, CSc.

Study programme: Fyzika
Specialization: 4F 6 Kvantová optika a optoelektronika

Prague 2016

Here I would like to thank all the people who helped and supported me. First and foremost, I would like to express my deep gratitude to my supervisor, doc. Miroslav Kučera for guiding me through the whole work on dissertation thesis. His expert advice was indispensable. Under his supervision I obtained plenty of experimental experience and learned a lot about presentation of scientific results.

I am also very grateful to my other advisors, Dr. Martin Nikl from the Institute of Physics AS CR for advice in the field of scintillation materials. I would like to thank to Ing. Karel Nitsch for early samples preparation and for crystal growth guidance he gave me. Next, I would like to express my thanks to my coworker RNDr. Zuzana Onderišinová for photoluminescence spectra and photoluminescence decay times measurements. Then I would like to thank to all colleagues from the Department of optical crystals of the Institute of Physics AS CR who helped me and supported me, especially to Ing. Alena Beitlerová, Mgr. Romana Kučerková and Ing. Vítězslav Jarý, for the photoluminescence decay times and radioluminescence measurements, and Dr. Petr Průša and Dr. Jiří A. Mareš for the light yield measurements. In addition, my gratitude belongs to Ing. Tomáš Mocek and Dr. Antonio Lucianetti for giving me an extra time I could spend on finishing this thesis.

I gratefully acknowledge the financial and organizational support that I received from the Charles University in Prague and the Czech Academy of Sciences. Substrates were prepared by Crytur Ltd., Turnov, Czech Republic

Last, but not least, I would like to thank my parents and others who supported me.

I declare that I carried out this doctoral thesis independently, and only with the cited sources, literature and other professional sources.

I understand that my work relates to the rights and obligations under the Act No. 121/2000 Coll., the Copyright Act, as amended, in particular the fact that the Charles University in Prague has the right to conclude a license agreement on the use of this work as a school work pursuant to Section 60 paragraph 1 of the Copyright Act.

In…..... date..... signature

Název práce: Příprava a optické vlastnosti oxidových scintilačních materiálů
Autor: Martin Hanuš
Katedra: Fyzikální ústav Univerzity Karlovy
Vedoucí doktorské práce: doc. RNDr. Miroslav Kučera, CSc., Fyzikální ústav Univerzity Karlovy
Abstrakt:

V této práci jsme se zaměřili na zkoumání vlastností scintilačních vrstev granátů ($R_xLu_{3-x}Al_5O_{12}$, $R_xY_{3-x}Al_5O_{12}$) dotovaných ionty vzácných zemin (Ce, Pr, Tb) a ortosilikátů ($R_xY_{2-x}SiO_5$; R = Ce, Tb) připravených metodou kapalné epitaxe, vlivem kodotace ionty Sc na emisi Pr^{3+} a Tb^{3+} iontů v granátech a vlivem iontů Zr na Ce^{3+} emisi v ortosilikátech. Oba systémy scintilačních materiálů se vyznačují vysokou kvantovou účinností a dobrou chemickou i mechanickou odolností. Jsou ideálními materiály pro stínítka v 2D zobrazovacích zařízeních. Konkrétně jsme studovali optické (absorpční, excitační a emisní spektra), scintilační (radioluminescence, světelné výtěžky) a strukturní vlastnosti. Cílem bylo prozkoumat tyto vlastnosti připravených vrstev a porovnat je s vlastnostmi monokrystalů připravených Czochralského metodou. Snahou bylo určení vlivu složení taveniny a technologických parametrů. Dále pak také stanovení optimálního množství dopantů ve vrstvě. Byla použita tavidla $PbO - B_2O_3$ a $BaO - BaF_2 - B_2O_3$. Tavidla umožňují růst granátových vrstev s nízkým obsahem intrinsických defektů krystalové mříže. Pěstované vrstvy o tloušťce 1 až 30 μm dosahují vyšších koncentrací dopantů oproti monokrystalům.

Klíčová slova: *Scintilátor, tenké vrstvy, LPE, LuAG, YAG, YSO, Ce, Pr, Tb*

Title: Preparation and optical properties of scintillation oxide layers
Author: Martin Hanuš
Department: Institute of Physics of Charles University
Supervisor of the doctoral thesis: doc. RNDr. Miroslav Kučera, CSc., Institute of Physics of Charles University, Charles University
Abstract:

In this work we studied properties of garnet scintillator layers ($R_xLu_{3-x}Al_5O_{12}$, $R_xY_{3-x}Al_5O_{12}$) doped by rare earth ions (Ce, Pr, Tb), orthosilicates (Y_2SiO_5; R = Ce, Tb) and influence of Sc codoping on Pr^{3+} and Tb^{3+} emissions. The Zr codoping on Ce^{3+} emission in orthosilicates was also studied. The samples were prepared by liquid phase epitaxy. The studied materials show high quantum efficiency and good chemical and mechanical stability. They represent ideal materials for 2D imaging devices. We studied optical absorption, excitation and emission spectra and scintillation properties (radiolunescence and photoelectron yield). The aim was to determine the properties of grown layers and their comparison to Czochralski grown single crystals. We looked for the impact of melt and growth conditions on measured layer properties. We also tried to determine optimal amount of dopants in layer. We used $PbO - B_2O_3$ and $BaO - BaF_2 - B_2O_3$ fluxes. Using these fluxes, we succeeded in growing layers with less intrinsic defects in crystal lattice in comparison to single crystals. In grown layers of thickness from 1 to 30 μm higher dopant concentration was achieved than in single crystals.

Keywords: *Scintillator, thin layers, LPE, LuAG, YAG, YSO, Ce, Pr, Tb*

Contents

1. Introduction

Scintillation materials are used since the discovery of the ionizing radiation for its detection. These materials transform the energy of the ionizing radiation into UV or visible light. There is wide variety of scintillation materials used based on properties and cost-efficiency ratio. They are scintillators based on plastic, glass or liquid, organic and inorganic single-crystalline materials.

Detectors based on scintillation material are followed by a photo detector. After absorption of the ionizing radiation (particle or X- or γ-ray photon) in the mass of the scintillator, ultraviolet or visible light photons are emitted due to scintillation conversion and consequently transformed by the photo detector to electrical signal that is collected and further processed. Scintillators nowadays are widely applied. They represent irreplaceable part of human life. They are used in high-energy physics, medical imaging, security, lights (see Figure 1), etc [1, 2].

This work focuses on materials with anticipated use in imaging applications, mainly as scintillation screens. Thin single crystal garnet layers doped by rare earth activator ions such as Ce [3], Pr, Eu, Tm and Tb are very suitable for use in scintillation screens, because the garnet lattice is physically, thermally and chemically very stable.

There are two basic alternatives how to achieve high spatial resolution. First is pixelation of bulk scintillator. It is commonly used in high-energy physics as it utilizes great volume of material and spatial resolution is given by pixel dimensions. Second way is creation of thin screen, which has spatial resolution close to 1 μm [4]. Such screens are best for low energetic particles (electron microscopes, soft X rays).

In the thesis, the thin film scintillator screens are studied. The layers were prepared by the liquid phase epitaxy (LPE). Main goal is development and fundamental research of such scintillators. Subject of interest is quantitative comparison to the Czochralski (CZ) grown single crystals. CZ single crystals are grown from stoichiometric melt (components in the melt are in the same ratio as in the crystal). Growth process involves very high temperatures (melting point of grown crystal is at approx. 2000°C). Unlike the LPE films that are grown from a flux at much lower temperatures (approx. 1000°C) and the structural disorder and number of intrinsic defects caused by growth temperature is significantly diminished. The garnet layers do not have antisite defects, where part of the Lu ions occupies the Al octahedral sites [5]. Normally, these defects form shallow traps in the bandgap and induce slow components in the scintillation decay times of single crystals [6]. On the other hand, various impurities from the flux and new defects are introduced into the crystal lattice. That is specific to the LPE growth and is further studied. Furthermore, many other factors, such as flux properties (composition, viscosity), growth temperature and supercooling, growth rate, substrate properties (layer–substrate

lattice match, defects in substrates) also significantly influence the quality and properties of epitaxial layers. Consequently, various point defects are created in layers that may cause loss of energy due to nonradiative transitions and decrease of emission intensity. For materials studied in this thesis, we optimized growth process. We strived for best possible layer composition, based on measured performance

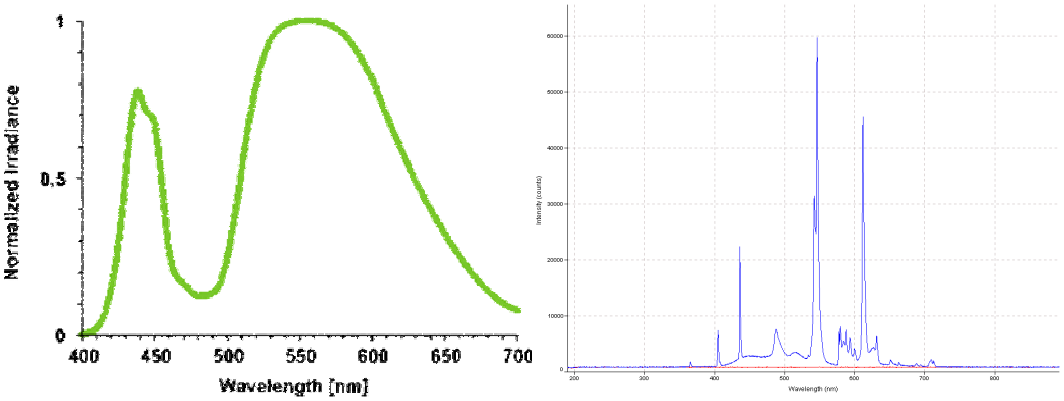

Figure 1: Left graph is white light emitting diode (LED) spectra, cited from [7], blue peak at 440 nm comes from excitation and wide peak with maxima at around 550 nm is Ce:YAG luminescence; The right graph is spectra of compact fluorescent light (CFL) declared as white equivalent to a blackbody temperature of 4200 K, UV peaks are remnants from Hg discharge light that was not transformed by scintillators or blocked by glass tube. Other peaks belong to phosphors deposited to inner side of glass discharge tubes.

1.1. Authors contribution

Majority of presented samples was grown by the author. Some were prepared by Ing. Karel Nitsch. Most of the experimental data, mainly absorption, photoluminescence excitation and photoluminescence emission spectra in the UV, VIS and IR spectral regions shown in the experimental part of the presented thesis were obtained by authors own measurements. Part of presented photoluminescence spectra, as well as most of photoluminescence decay times was measured by fellow colleague RNDr. Zuzana Onderišinová. The rest of the photoluminescence decay times and all radioluminescence and light yield measurements were carried out in the Institute of Physics, Czech Academy of Sciences in Prague (ASCR), Czech Republic, in the Department of Optical materials. There, the photoluminescence decay times and radioluminescence were measured by Ing. Alena Beitlerová and Mgr. Romana Kučerková, light yield measurement by Dr. Jiří A. Mareš and Dr. Petr Průša. Further evaluation was done by author as well as data processing for presented graphs. Together with his supervisor and other coauthors of joint publications, author participated in the results interpretation, description and corresponding manuscripts preparation.

2. Scintillation materials basics

Deep knowledge about light and matter interaction with focus on luminescence and scintillation processes is presented in [8-13]. This whole chapter is a brief summary of basics from the literature.

2.1. Interactions with matter

2.1.1. Absorption

The radiation is absorbed in the material. It creates an excited state. The excited state can than return to the ground state by emission of radiation. This suggests that ions in material are capable of luminescence. Radiative emission processes compete with nonradiative transitions. In nonradiative transitions, the energy of the excited state is transformed to the vibrations of the host lattice, i.e. to generate heat. Efficient luminescent materials have suppressed nonradiative processes. The ratio of radiative to nonradiative transition rates determines the conversion efficiency of the material. If we excite with high energetic radiation (X-rays, electron beams, etc.), the host lattice is excited the most. In many cases the host lattice transfers its excitation energy to the activator. The host lattice then acts as the sensitizer.

The absorption coefficient describes how a light beam becomes attenuated after passing through a material. Experimentally proven formula (2.1) of the beam intensity attenuation shows that the light intensity at a distance x into the medium is exponentially reduced. In the case of negligible scattering, α is the absorption coefficient of the material.

$$I = I_0 e^{-\alpha x} \tag{2.1}$$

The intensity I relates to the incoming light intensity I_0 and to the distance it travels x. This law is known as the Lambert-Beer law.

2.1.2. Reflectivity

Reflectivity spectra provide similar and complementary information to the absorption [10]. For instance absorption coefficients that can only be measured by using very thin samples (thin films). In these cases, the reflectivity spectra R(λ) can be very advantageous, as they manifest the singularities caused by the absorption process but with the possibility of using bulk samples. The reflectivity is defined by:

$$R = \frac{I_R}{I_0} \tag{2.2}$$

where I_R is the reflected intensity. Reflectivity spectra can be registered in two different modes, direct reflectivity or diffuse reflectivity. Direct reflectivity measurements are made with well-polished samples at normal incidence. Diffuse reflectivity is generally used for unpolished or powdered samples with collecting of all reflected light.

2.1.3. Luminescence

Luminescence can be interpreted as an inverse process to the absorption. Excited atomic systems that absorbed light at resonant energy of the transition can return to the ground state by spontaneous emission of photons. This relaxation process is called photoluminescence. However, the absorption of light is only one of the multiple mechanisms by which a system can be excited. In a general, luminescence is the emission of light from a system that is excited by some form of energy. Luminescence can be obtained by excitation with an electron beam in case of cathodoluminescence. Excitation by high-energy electromagnetic radiation (ionizing radiation) such as X-rays, α-particles (helium nuclei), β-particles (electrons), or γ-rays causes radioluminescence. Scintillation materials are based on this luminescence mechanism. Thermoluminescence occurs when a substance emits light because of the release of energy stored in traps by thermal heating. Thermoluminescence can be used to study traps when the material is slowly heated from cryogenic temperatures.

If we speak about luminescence, the important part represents influence of the host lattice. If we have a luminescent centre in different host lattices, the optical properties of this center are also different. This is due to change of the forces in surroundings. Main reasons are covalence and crystal field [8]. For increasing of covalence, the interaction between the electrons is reduced, since they spread out over wider orbitals. This results in electronic transitions between energy levels with

an energy difference, which is determined by electron interaction to be shifted to lower energies as the covalency increase. Higher covalency also means lower electronegativity difference between ions and so charge-transfer transitions between these ions are shifted to lower energies. Crystal field is the electric field at the site of the ion under consideration and spectral position of any optical transition is determined by the strength of this field. (well-known and clear example is green emission of Cr^{3+} in Cr_2O_3 compared to red in $Cr:Al_2O_3$) [8]. The crystal field is also responsible for the splitting of certain optical transitions.

An important characteristic of the luminescence center is called Stokes shift. It is a shift in wavelength between luminescence and absorption. If we consider rigid lattice for simple two-level system, the absorption and emission spectra peak appear at the same energy (see the energy levels diagram at Figure 2). In general, the emission spectrum is shifted to lower energies relatively to the absorption spectrum. This can be explained in solids by theory about ions that are oscillating around equilibrium positions. Neighboring ions are in a harmonic motion. This allows us to modify the two level energy diagram shown in Figure 2 and approximate both levels with parabolas as shown in Figure 3 in the left diagram. The ground and excited states of such luminescent centers can be described by configurational coordinate diagram (see Figure 3). The system is excited from the ground state. The relaxation follows excitation. The lowest vibrational level of the excited state is populated. From there, the emission takes place with transition to the higher vibrational levels of the ground state (see [9] for more details). The larger the distance of the minima of the parabolas between ground and excited state $\Delta Q = Q_0 - Q_0'$, the larger the Stokes shift and broader the emission and excitation bands. The difference ΔQ is determined by the electron-lattice coupling characterized by Huang-Rhys coupling constant S. The constant is proportional to $(\Delta Q)^2$ and ranges from 1 to 5 for weak or medium coupling regime and exceeds 5 in the strong coupling regime. If the two parabolas have the same force constant (same shape), the amount of the energy loss during the relaxation can be described as $Sh\nu$, where $h\nu$ represents spacing of two vibrational levels. Then the Stokes shift amounts to $2Sh\nu$ [8]. Efficient scintillation material should have large enough Stokes shift to prevent reabsorption of the emitted light by another luminescence center. At higher temperatures, if there is an intersection of both parabolas, the system can return from excited state through this intersection

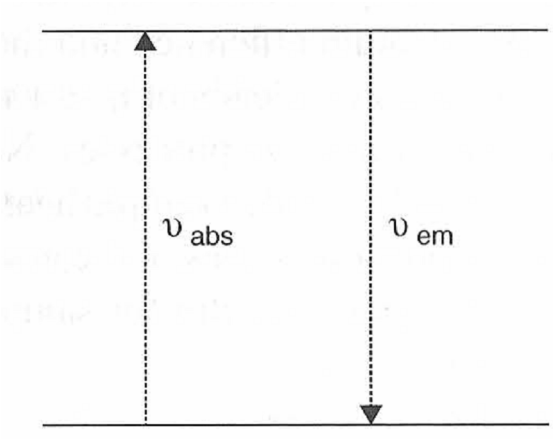

Figure 2: The absorption and emission energies for a two-level system (rigid lattice) [9]

point back to the ground state without emission. This phenomenon is called thermal quenching [8].

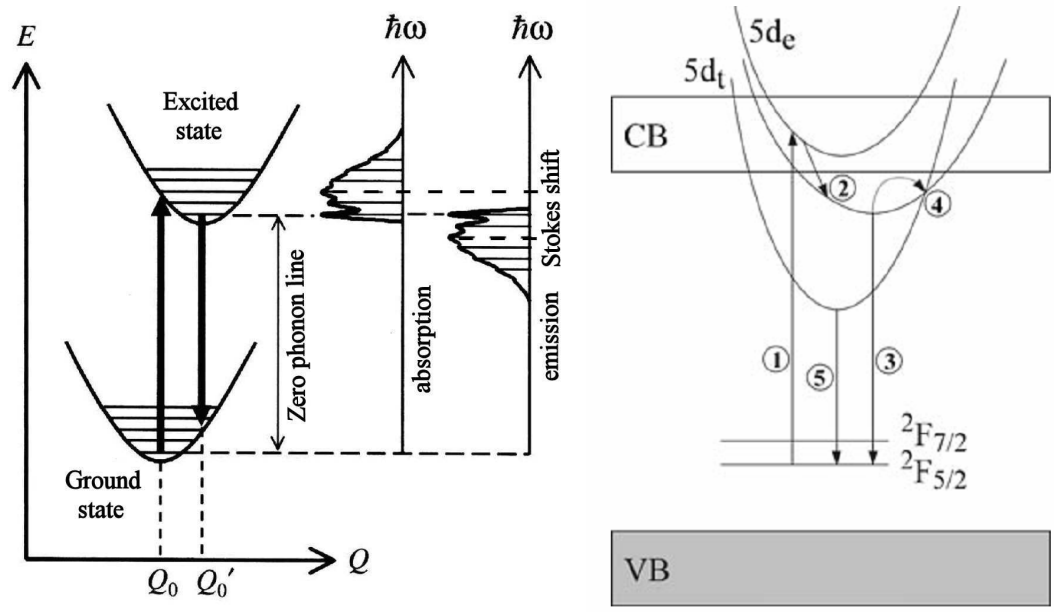

Figure 3: On the left is depicted configurational coordinate diagram that is, in general illustrating transitions from ground to excited state (parabolas with indicated vibrational states) and back, with corresponding absorption and emission spectra and their Stokes shift indicated [10]; on the right, there is an energy-level scheme illustrating the anomalous Ce^{3+} emission occurring under 250K in $Ce:Cs_2LuCl_6$ and $Ce:LaI_3$ (CB = conduction band, VB = valence band). After excitation from the $^2F_{5/2}$ ground state to a $5d_e$ level within the conduction band (1), a radiationless transition to a further $5d_e$ state occurs (2); there is then either the anomalous emission (3) or a radiationless transition (4) with subsequent normal emission from the $5d_t$ levels (5) [2]

2.1.3.1. Color centers

There are many crystallographic defects occurring due to fabrication process limitations. These defects are specific for every type of crystal and growth conditions. They are also called F centers, and they belong to a group of intrinsic defects. Color centers are intrinsic defects that are optically active. Good approximation for characteristic pattern in absorption spectra can be described in the same way as that of the hydrogen atom because of their structure. They consist of a system incorporating one or more electrons bound to a vacancy. Impact of color centers on luminescent properties grows with material bonding strength. Therefore ionic compounds (such as halides like KCl) are the best known for distinctive color centers. For example, crystal of KCl with F centers is of vividly blue color (see Figure 4), because the absorption maximum in the red [8].

In garnets, the main cause for color centers is due to oxygen vacancies [14, 15]. They are product of reducing atmosphere used during growth process. The amount of color centers is reduced by post processing through oxygen annealing at

high temperature for prolonged time. The remnant color centers discovered in used garnet substrates are shown in Figure 38 and are in agreement with cited literature. Observed slight shift is due to crystal field change induced by Lu substitution of Y. In the depicted graph is visible broad emission originating from color centers at 400 nm and 650 nm.

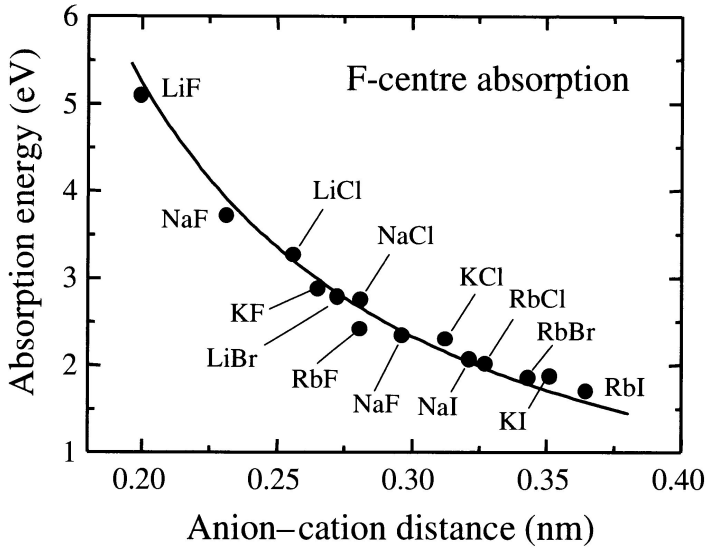

Figure 4: Energy of the peak absorption of the color centers for several face-centered cubic alkali halide crystals. The energies are plotted against the anion-cation distance a. The solid line is a fit proportional to $(1/a)^2$. [10]

2.1.3.2. Rare earth ions

Most commonly, rare earth (RE) ions from the lanthanides group are used as phosphors, in lasers, and amplifiers. Their properties are in great detail described in literature [8]. Lanthanides are in periodic table located after the lanthanum. From the cerium (atomic number 58, a simplified diagram of energy level splitting for the ground state and the first excited 5d states of Ce^{3+} in crystal field of garnets is shown in Figure 5) to the ytterbium (atomic number 70). These atoms are usually incorporated in crystals as divalent or trivalent cations. A summary of basic properties of wide variety of host materials and ions is collected in [16]. In trivalent ions 5d, 6s, and some 4f electrons are removed

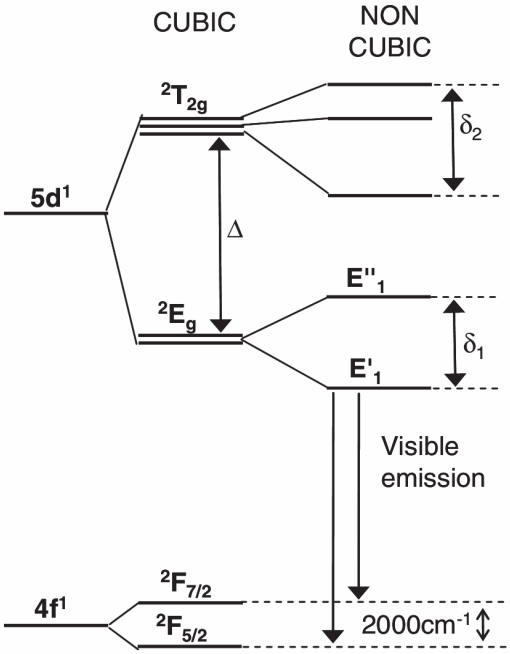

Figure 5: Simplified diagram of energy level splitting for the ground state and the first excited 5d states of Ce^{3+} in crystal field of garnets. The cubic crystal field splitting is indicated by Δ and noncubic splitting by δ, cited from [17]

and so we observe transitions between sublevels of the 4f shell. Some of them, namely Ce, Pr and Tb, are in the center of focus in this work. They prefer f - d interconfigurational optical transitions (graph of energetic level distribution is shown in Figure 6).

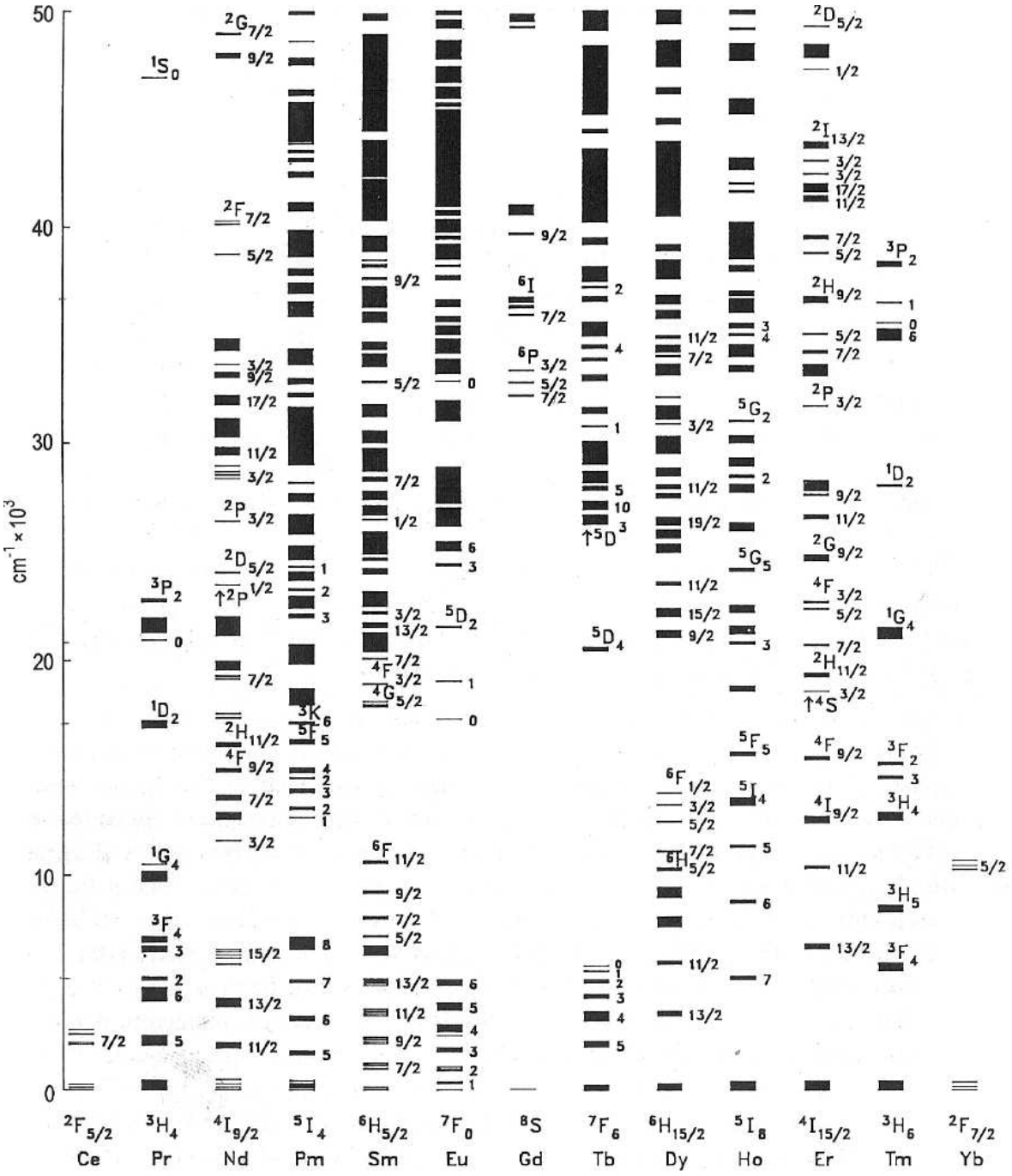

Figure 6: Energy levels of the 4f ^{n} configurations of the trivalent lanthanide ions cited from [8]

2.2. Scintillation process

The origin of the scintillation light is the energy loss of ionizing radiation (X-, γ-ray, α-, β-particles, etc.) passing through matter. The scintillation process is a conversion mechanism. It can be divided into five main consequent stages. The first one starts with the production of primary excitations by interaction of ionizing particles with the material. These are followed by production of large number of secondary electrons by inelastic electron scattering and Auger processes with consequential population of the conduction band with electrons and valence band with holes. In the second stage thermalization of electrons dominates (phonon production). That leads to population of the bottom of the conduction band with electrons and the top of the valence band with holes. In the third stage, there is localization of the excited states on defects and impurities. In last two steps the relaxed excitations migrate and recombination occurs either radiative or nonradiative (see in Figure 7) [11].

These three fundamental mechanisms of electromagnetic interactions are responsible for absorption of high-energy radiation:

- ***photoelectric effect (photon interacts with an electrons in an inner shell),***
- ***Compton scattering (the photon interacts with an electron in the outer shell of an ion in the material and transfers part of its energy to this electron),***
- ***pair production (creation of electron-positron pair)***

The interaction cross-section for each of these mechanisms is dependent on energy of incident radiation. Photoelectric effect and Compton scattering are dominant at lower and medium energy range and pair formation at energies higher than 1.02 MeV where the energy is sufficient to produce electron-positron pair (see in Figure 8). Neutral particles lose energy mainly through direct interactions with nuclei. As long as the energy of particles is high enough for multiple scattering and electron-positron pair creation, their energy is distributed to a number of secondary particles of lower energy, which form an electromagnetic shower. Below the threshold of electron-positron pair creation, electrons will continue to lose energy through Compton scattering. The shower will start to couple with the electrons and atoms of the lattice. It will excite the electrons from the occupied electronic states of the material (valence or deeper bound states). Each interaction creates an electron-hole pair.

Scintillator material contains luminescent centers. They are either extrinsic (generally dopants), or intrinsic. In the above-mentioned transport process, electrons and holes (eventually excitons) travel through the material (for time scale of these processes see Figure 7). They are repeatedly trapped on defects (energy levels created inside the material forbidden gap), energy losses may occur due to nonradiative recombinations etc. Considerable delay to the decay time can be

introduced due to this charge trapping. This is the least predictable material property as point defects, flaws, surfaces and interfaces randomly introduce energy levels into the forbidden gap and strongly influence scintillation performance. The traps are dependent on technology of material preparation [18]. Trapping states are studied by means of thermally stimulated luminescence (TSL) measurements.

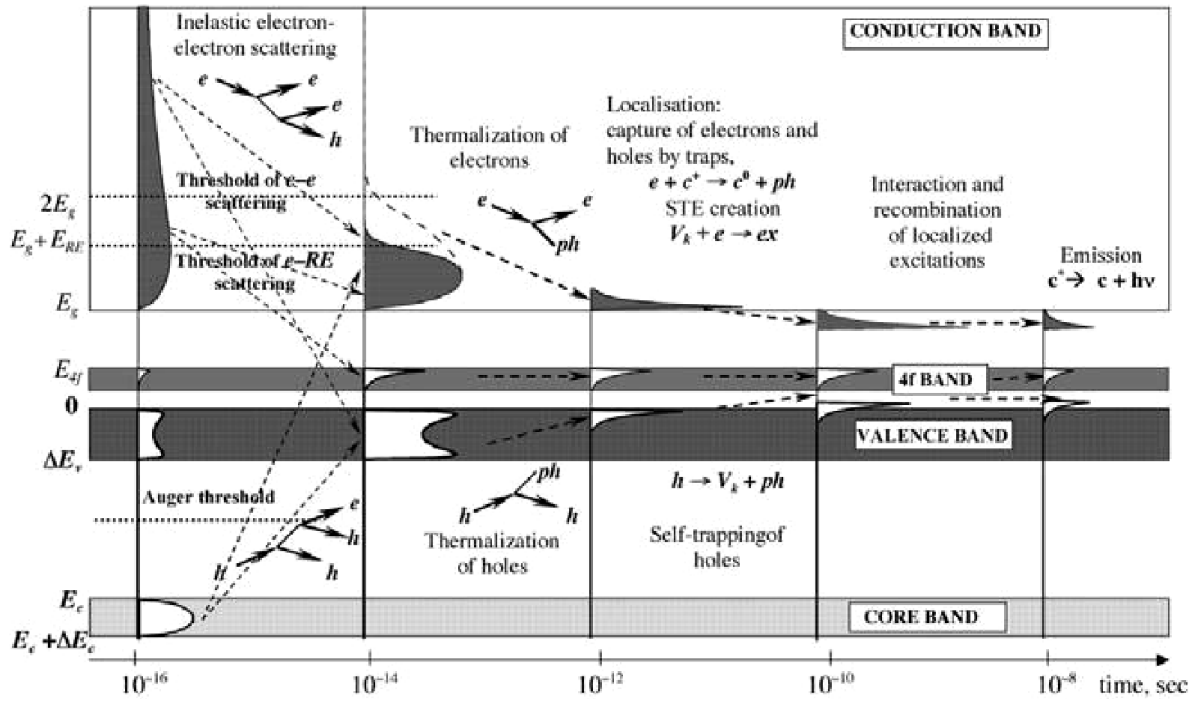

Figure 7: A general scheme of relaxation of electronic excitations in rare earth containing crystals with approximate timescale (Only one core band is represented with top energy E_c and bandwidth ΔE_c. The valence band with top energy E_v = 0 and bandwidth ΔE_v and the conduction band with bottom energy E_g. They are separated by the forbidden band of the insulator (band gap width E_g). [11]

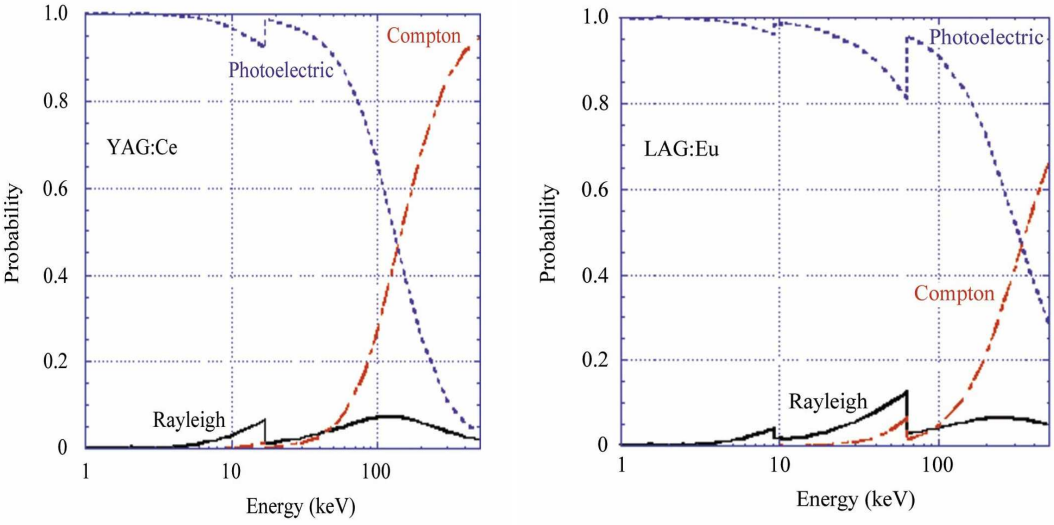

Figure 8: Main processes of attenuation and their probability in material of Ce:YAG (left) and Eu:LuAG (right). Photon energy is in logarithmic scale (cited from [3])

2.3. General characteristics of scintillation materials

For general use of scintillation materials are important following characteristics [19] (depending on purpose, some are more relevant to others):

- Conversion efficiency and scintillation light yield
- X-ray stopping power and effective atomic number
- Scintillation response – decay time
- Spectral matching between the scintillation material emission spectrum and photo detector spectral sensitivity
- Chemical stability and radiation hardness
- Linearity of light response with incident x (γ) – ray photon energy
- Energy resolution

2.3.1. Conversion efficiency and scintillation light yield

The overall efficiency of the conversion of ionizing radiation to scintillation photons is determined by both intrinsic (lattice) and extrinsic (defects, dopants) material characteristics. One particle with high energy may create many electron - hole pairs. For instance, in $CaW0_4$, one X-ray quantum may yield 500 quanta of emission. In order to create average electron-hole pair (with energy equal to E_g), a much greater amount of energy is needed. This energy was experimentally estimated by Shockley to be roughly $3E_g$ for semiconductors (so maximum possible conversion efficiency is therefore reduced to one third). Generally, we can describe the average energy E required to create an electron - hole pair [8]:

$$E=\beta E_g \tag{2.3}$$

The parameter β can be from about 3 (GaP ZnS, Csl, Nal), 4(La_2O_2S), 5.6 ($Y_3AI_5O_{12}$) to 7 ($CaWO_4$, YVO_4) [8]. The expression for the radiant efficiency η is:

$$\eta = (1-r)\frac{h\nu_e}{E}Sq \tag{2.4}$$

Losses caused by radiation penetration without absorption represents r, ν_e is averaged frequency of the emission. Average energy E is defined by Equation (2.3). S is the efficiency of electron - hole pair energy transfer to the luminescent centre, and q is the quantum efficiency of luminescent centre [8]. Assuming from the above formula (2.4), to obtain a material producing large number of scintillation photons, the forbidden bandgap must be small. Contradictory, the bandgap must be large, to efficiently transmit the emitted light. Additionally it is preferable that the luminescent center exhibit large Stokes shift to avoid re-absorption of the emission.

The conversion efficiency is related to the light yield (LY) of a scintillation material. LY is defined as a fraction of photons emitted from scintillator that were detected within a certain time window (usual range is from 100 ns up to 10μs) after irradiation by ionizing radiation with an energy of 1 MeV. This means that LY shows an inferior information with respect to the equation (2.4) [18]. LY measurements are carried out by exciting the material with a pulsed X-ray source or more often γ-radiation of various radioisotopes. Emitted light is detected in a photon counting mode. This means that sufficiently low excitation rates are needed to allow complete regeneration of the detection system before each event. The LY values are usually expressed in the number of photons generated in respect to energy of absorbed X or γ-ray photons (mostly expressed in photons / 1 MeV). However, there is a large spread in measured data in the literature. This is mainly caused by different quality of the crystals from different suppliers [20]. In general applies, the higher the LY, the better the energy resolution of the scintillation detector. It is necessary to mention, that the LY is energy dependent. It results in the non-proportionality of the scintillation response and degrades the energy resolution.

2.3.2. X-ray stopping power and effective atomic number

For high-energy radiation apply the same law as for the absorption. Generally, we derive from formula (2.1) a more general law as we take into account occurring effects (see Figure 8 and Figure 9). The transformation of the attenuation coefficient α to total attenuation coefficient μ follows [12]:

$$\mu = \tau + \sigma + \kappa \tag{2.5}$$

τ denotes photoelectric effect, σ Compton Effect and κ pair production. The total attenuation coefficient observed over wide range of wavelengths show characteristic

absorption edges. These edges occur as soon as the X-ray energy reaches the binding energy of particular electron shell [12].

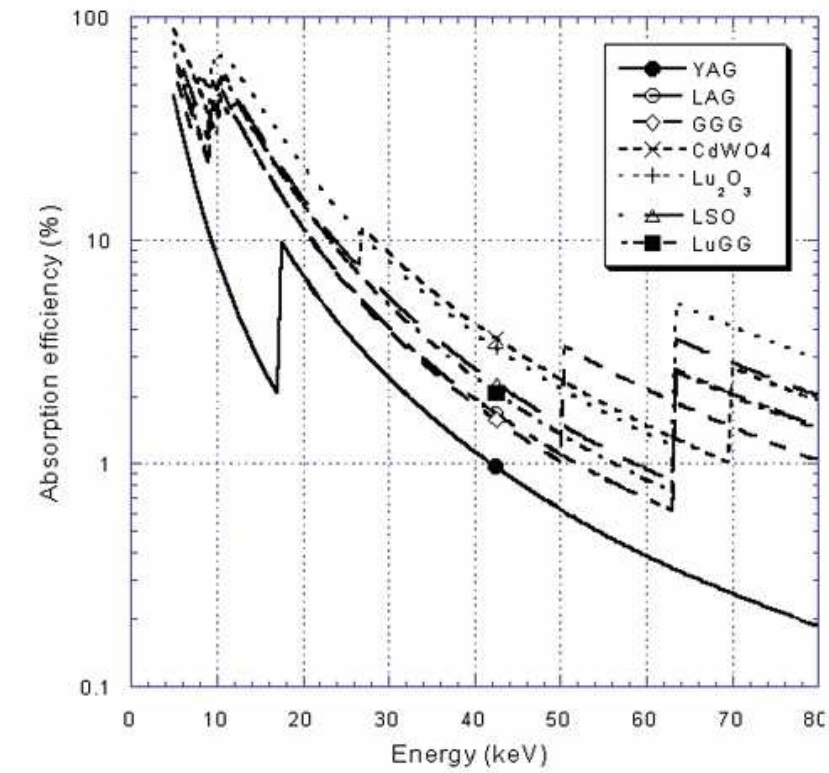

Figure 9: Absorption efficiency of some current scintillators used for high resolution X-ray imaging, measured for 5 mm thick layers: $Lu_3Al_5O_{12}$ (LuAG/LAG, 6.6 g.cm^{-3}), $Gd_3Ga_5O_{12}$ (GGG, 7.09 g.cm^{-3}), $Lu_3Ga_5O_{12}$ (LuGG, 7.5 g.cm^{-3}), Lu_2O_3 (8.4 g.cm^{-3}), Lu_2SiO_5 (LSO, 7.4 g.cm^{-3}), $Y_3Al_5O_{12}$ (YAG, 4.55 g.cm^{-3}) and $CdWO_4$ (7.9 g.cm^{-3}) (cited from [3])

Efficient scintillation material for X or γ-rays detection should have high density ρ and high effective atomic number Z_{eff}. The probability of absorption by photoelectric effect is proportional to the value of ρZ_{eff}^{3-4} [21]. The effective atomic number can be obtained from equation:

$$Z_{eff} = (W_A Z_A^4 + W_B Z_B^4 + W_C Z_C^4)^{1/4} \quad (2.6)$$

This is true for material of $A_xB_yC_z$ composition, where Z_{A-C} denotes the atomic numbers of the constituent elements A, B, C and W_{A-C} denotes the corresponding weight fractions of the elements in the compound [19].

2.3.3. Scintillation response and decay time

The kinetics of luminescence is crucial additional information about luminescent centers. We obtain intensity relations that give us correspondence to the excited state decay rates after the optical feeding stops. The decay rates are determined by the characteristics of the transport and luminescence stages as they are much slower than the initial conversion mechanisms (see Figure 7). A non-stationary density of centers N in the excited state is observed under repeatedly interrupted excitation. These excited centers can decay to the ground state by radiative (light-emitting) and non-radiative processes. The decay time τ is longer for the emission at longer wavelengths and obeys the law $\tau \sim \lambda^2$ [8]. The evolution of the excited state population N follows a very general rule:

$$N(t) = N_0 e^{-A_T t} \tag{2.7}$$

where N_0 is the density of excited centers at time t = 0, that is just after the light pulse absorption and A_T is the total decay rate, which means:

$$A_T = A + A_{nr} \tag{2.8}$$

where A state for the radiative rate and A_{nr} the nonradiative rate. The decay rate of the luminescence center is defined by its transition dipole momentum from the excited to ground state and can be further enhanced by nonradiative quenching, or energy transfer processes. The relaxation process can be experimentally observed by decay of the emitted light. The emitted light intensity I_{EM} at a given time t is proportional to the number of centers de-excited per unit of time, and it can be written in simplest way as:

$$I_{EM}(t) = I_0 e^{-A_T t} \tag{2.9}$$

where I_0 is the intensity at t = 0. This equation is an exponential decay law for the emitted intensity. Decay time τ is equal $(A_T)^{-1}$ and represents the time in which the initial emitted intensity I_0 decays to e^{-1}. Decay time can be obtained from the dependence of intensity on time measured from a pulsed luminescence experiment.

For more complex cases, where luminescent centers with different decay times are present, measured decay curve can be described as a sum of decay curves:

$$i(t) = \sum_{j=1}^{m} i_j(0)\, e^{-\frac{t}{\tau_j}}$$

(2.10)

Decay time value gives the total decay rate (radiative plus nonradiative rates). Consequently the quantum efficiency η can be written as:

$$\eta = \frac{A}{A + A_{nr}} = \frac{\tau}{\tau_0}$$

(2.11)

2.3.4. Chemical stability and radiation hardness

Based on application, the scintillation crystals are to be stable mechanically and chemically inert. They are mostly used under normal atmospheric conditions and under ionizing irradiation. Some scintillation materials are hygroscopic, which makes them unusable without shielding from moist. This applies to halides generally (such as NaI:Tl, CsI). Application of such scintillation materials is less versatile and increases the production costs [22].

Radiation hardness is very important feature. Use in the ionizing radiation introduces strain to bonds in lattice. Newly induced trapping states cause problems in the scintillation process. The transport of the thermalized charge carriers is hindered. This may lead to a light yield decrease, slowing of the scintillation decay kinetics, and material deterioration. Radiation induced color centers and deep traps emerge as a result of restoring a charge balance in the lattice. Color centers change the absorption spectrum of the crystal. This can cause reabsorption of the emitted light and further decrease of the light yield. It is called induced absorption. Radiation hardness is most crucial if the material is under severe radiation doses.

3. Studied materials

3.1. Garnets

Primarily, the epitaxial layers were of garnet crystal structure. Specifically they were lutetium aluminum garnet with chemical structure formula $Lu_3Al_5O_{12}$ (LuAG), yttrium aluminum garnet $Y_3Al_5O_{12}$ (YAG) and transitioning LuYAG with various lutetium and yttrium content. These lattices were doped by rare earth ions (namely Ce, Pr and Tb) and occasionally with an additional doping element, Sc, Ga and Gd.

3.1.1. Crystallographic structure

The garnet structure has cubic symmetry space group O_h^{10} that has a complicated elemental cell consisting of 8 molecules of total amount of 160 atoms (96 oxygen atoms and 64 cations). There are three different cation sites defined by polygons consisting of oxygen atoms (see Figure 10). Largest cations are surrounded by 8 oxygen ions that are forming the dodecahedral site. Smaller cations have 6 oxygen ions as neighbors in the octahedral site. The smallest cations on the tetrahedral site are surrounded by 4 oxygen ions. Ions occupying these sites determine lattice constant of the garnet. A way to calculate the lattice constant based on these cations will be shown later. The density of LuAG is 6.72 g/cm^3, of YAG is 4.53 g/cm^3 [23]. Pure LuAG and YAG crystal is colorless.

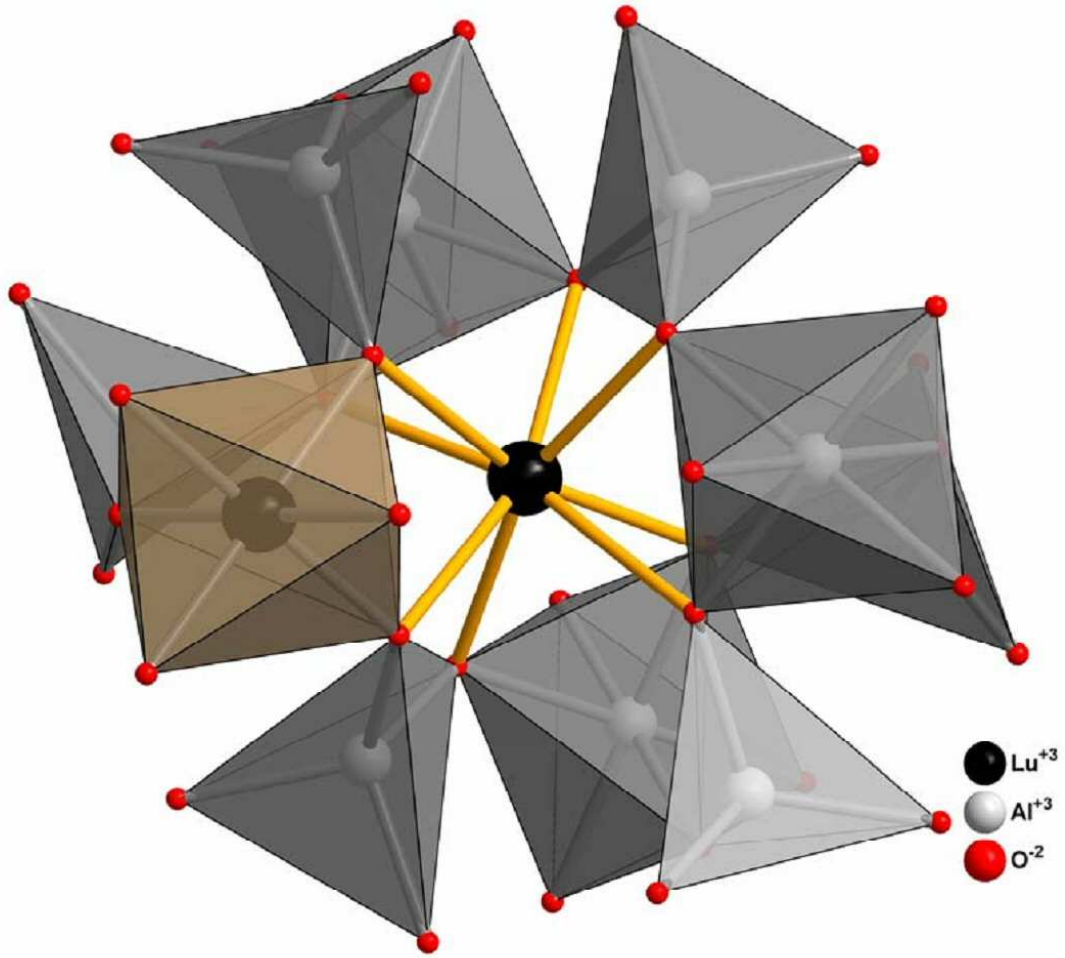

Figure 10: Geometrical representation of the LuAG lattice structure with highlighted anti-site defect (brown octahedron on the left side); cited from [19]

3.1.2. Cerium doping

The Ce:YAG material was first developed in 1967 by Blasse and Bril [24-26] and it was used in cathode ray tubes since. Ce ions in YAG exhibit intense luminescence, have fast scintillation response, high light yield, along with favorable mechanical and chemical properties [27]. The Ce ions replace Y or Lu in dodecahedral sites. Fast emission, about 60 ns, of cerium (Ce^{3+}) in host lattice of LuAG / YAG makes these garnets perspective for fast detectors. The ground state of the Ce^{3+} ion contains single electron in the well-shielded 4f - shell, which is optically active. The ground state is split into two levels by spin orbital coupling [8]. It can be excited to the 5d configuration and at most five distinct 4f - 5d excitation transitions (see Figure 5) are observed, depending on the site symmetry [28-31]. The emission occurs from the lowest crystal field split level of the $5d^1$ configuration to two levels of the ground state. These are typical for Ce^{3+} ions and correspond to the allowed

optical transitions from the ground state multiplet $^2F_{5/2}(4f_1)$ to $^2D(4f_05d_{1,2})$ excited states (see Figure 5 and Figure 13). The ^2D term is split into 5 states in the crystal field of D_2 symmetry of dodecahedral Ce ions [26]. The Stokes shift is never large and varies from a thousand to a few thousand wave numbers (medium coupling case) [8]. Slow components found in the decay curve probably occur due to the anti-site defects, when Lu resides in the Al position (Lu_{Al}) and vice versa (see Figure 10) [6, 32]. Mathematically formulated reasons for this assumption are studied in great detail by Kuklja in [33] and further researched in [34-36]. Anti-site defects are the cause of rich thermally stimulated luminescence (TSL) signal below room temperature [37]. In addition, energy levels related to shallow or deep traps (anti-sites or impurities) commonly participate in delayed radiative recombination at the Ce^{3+} centers and negatively influence the scintillation response. Liquid phase epitaxy growth effectively eliminates these defects [38]. The reason is growth temperature. It is considerably lower when compared to the Czochralski crystal growth from the stoichiometric melt. However, such LPE films are contaminated by flux components, especially Pb ions, which results in exciton localization around them and possibly also in creation of another trapping levels [39-41].

3.1.3. Praseodymium doping

Even faster emission, about 20 ns, can be obtained from the praseodymium (Pr^{3+}) ion [42]. These garnet systems are potential candidates in fast scintillation applications [43, 44]. In garnet host matrices with the medium-strong crystal field, the lowest 5d state is shifted below the $^1S_0$ level of Pr^{3+} and makes the 5d - 4f radiative transition possible [43]. The emission is shifted to higher energies with respect to the Ce^{3+} [8]. The 5d - 4f emission decay time obeys relationship $\tau \sim \lambda^2$ (mentioned above in chapter 2) and as the Pr emission wavelength is shorter than that of Ce, the decay time is also shorter. Interesting properties of Pr:LuAG material was recently found. The relative scintillation light yield calculated from the photopeak of the pulse height spectrum was at least two times higher when compared to a standard BGO sample. However, slow components were present in the scintillation decay curves [45]. There is a room for material optimization [46-48]. Slow components found in Pr:YAG were explained by the presence of the anti-site defects like in Ce doped garnets mentioned above and were studied further in [5].

3.1.4. Terbium doping

Another interesting ion is Terbium. Tb^{3+} ions emission is in the visible range. It has an efficient luminescence [49]. The Tb:LuAG RL comes from host-to-activator energy transfer mechanisms and it is characterized by slow emission [50]. The luminescent spectra largely depend on the concentration of Tb [51, 52]. The

absorption band at 277 nm and associated 233 and 323 nm bands with less intensity can be attributed to the inter-shell electronic transitions connecting the ground state $^7F_6$ (4f) to the split 5d energy levels [53, 54]. Second group of absorption bands has three relatively weak peaks located around at 355 nm, 380 nm and 487 nm. They are related to intra-shell 4f - 4f transitions [42]. All are shown in excitation spectra in Figure 11. Example of highly doped Tb:YAG emission spectra are shown in Figure 12. There are also included corresponding energy levels of transitions responsible for given emission bands.

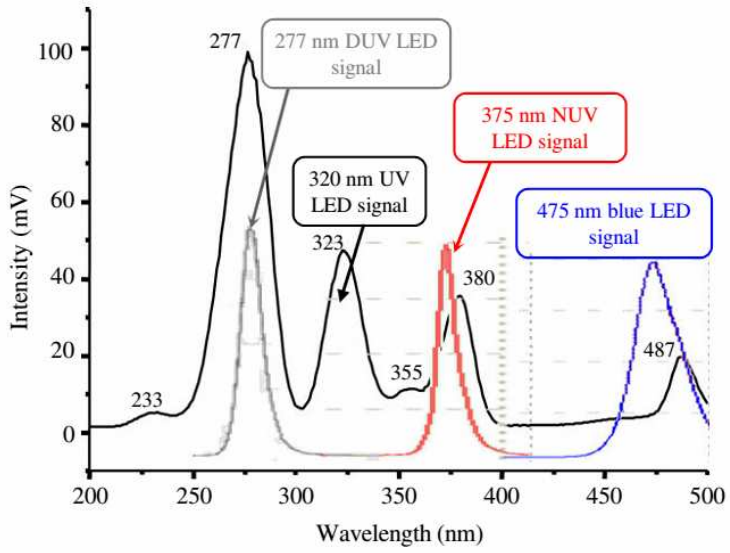

Figure 11: Excitation spectrum of a Tb:YAG (20 mol %) powder sintered for 4 h at 1100°C. Accompanied with UV and blue LEDs emission spectra for reference. Cited from [51]

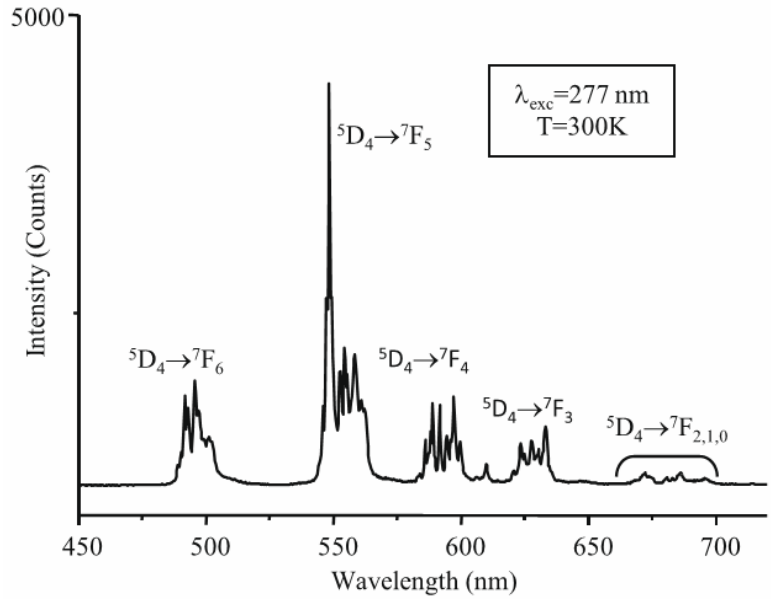

Figure 12: Emission spectrum of a Tb:YAG (20 mol %) powder sintered for 4 h at 1100°C. With corresponding energy levels of transitions responsible for given emission bands. Cited from [51]

3.1.5. Co-doping

Combination of Ce, Pr [55] and Ga, Gd [56, 57] doping in multicomponent CePr:$(GdLu)_3(GaAl)_5O_{12}$ garnet show promising results when it comes to color tailoring of the emission wavelength [58, 59]. Aside from success in improving of optical and scintillation properties of Ce^{3+} doped LuAG [60, 61], this material composition was also studied as a perspective LED phosphor, thus additional measurements in visible and UV range were carried out. Use of this multicomponent material is driven by color rendering properties, because pure Ce:YAG has red spectral deficiency. This predicament can be settled by adding red luminescent center such as Pr^{3+} (see Figure 13) and by changing lattice crystal field adding Gd [58].

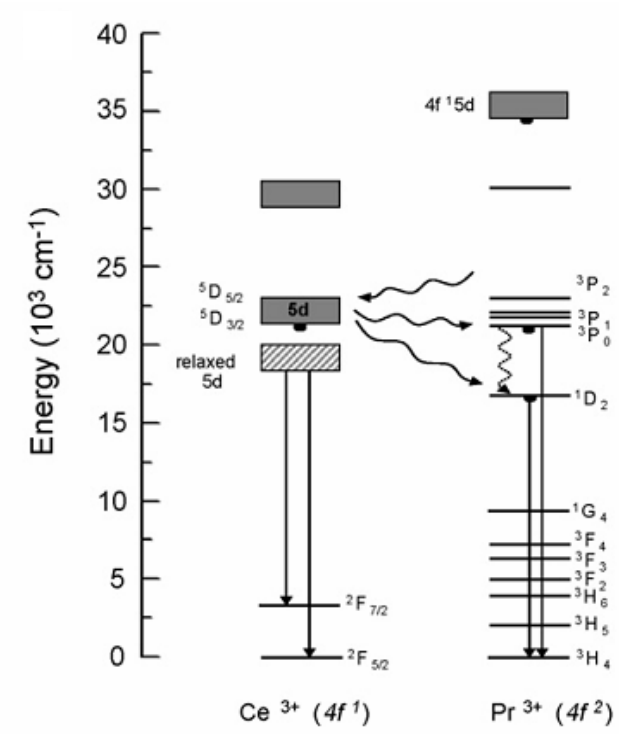

Figure 13: Schematic energy level diagrams of Ce^{3+} and Pr^{3+} ions. With sketch of energy transfer and transitions. Cited from [58]

It seems that Ga substitution in multi-component Gd garnets play key role in improving scintillation properties. Shallow traps related to the unspecified structural defects present in the material are reduced, because Ga doping [62] lowers the bottom of the conduction band. This way, the shallow traps are buried in the conduction band. Unfortunately, the Ce centers are affected too [56]. The luminescence quenching begins at

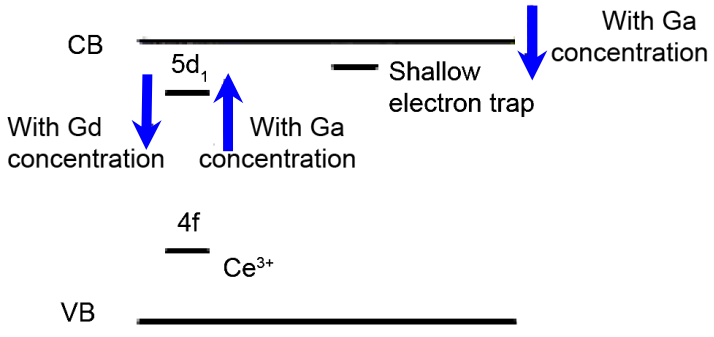

Figure 14: Schematic diagram of bandgap engineering in multicomponent garnets for Ce^{3+} ion. Cited from [56]

lower temperatures, or it is completely quenched. The Gd substitution increases crystal field (practical example in Figure 15) and lowers the split excited states of Ce ions (see the graphical representation in Figure 14), thus effectively returns the Ce centers inside the bandgap [17]. In work of Fasoli [63], even deeper electron traps were reported missing thanks to Ga admixture.

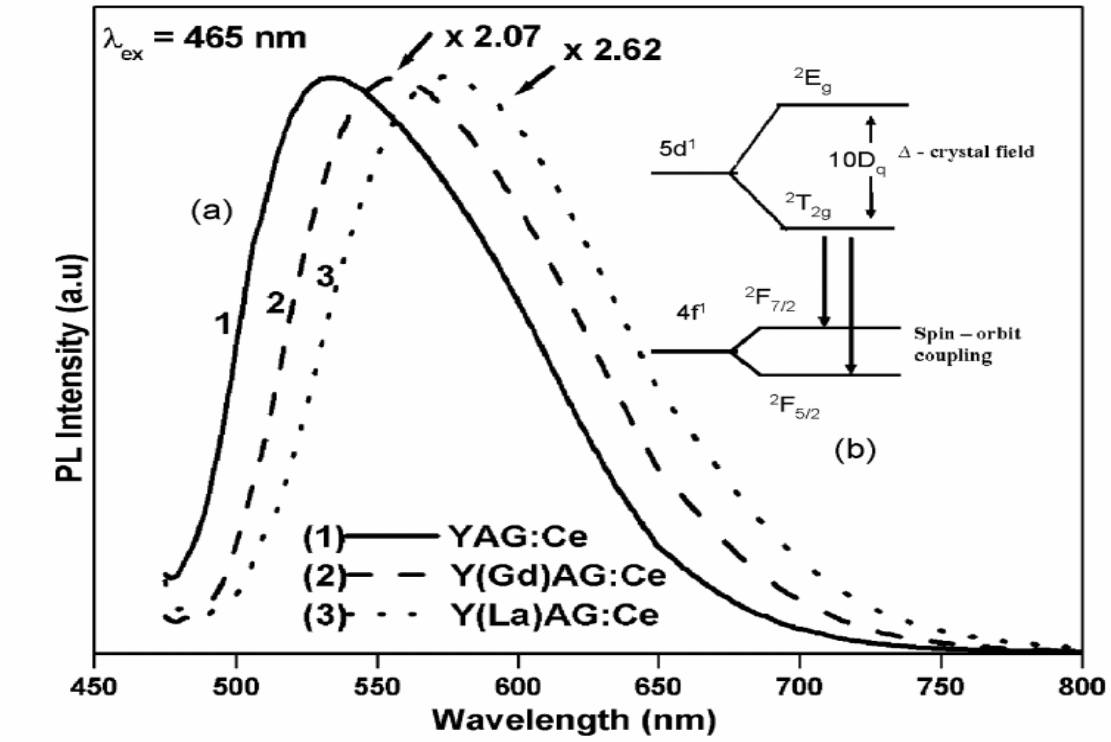

Figure 15: PL emission spectra of Ce:YAG compared to multicomponent garnet with either Gd or La codoping; The inset shows scheme of energy level environment dependence of Ce^{3+} ion in crystal field) Cited from [59]

For high power, high radiant flux LEDs, it is desirable to separate the PN junction from the luminescent material. The heat produced by the junction reduces the luminescence efficiency and consequently the overall intensity, as it is shown in Figure 16 (cited from work of Bachmann [64]). Thin screen illuminated by the diode is ideal in terms of thermal separation. In such case, the angular distribution of spectra becomes a problem and it will be studied.

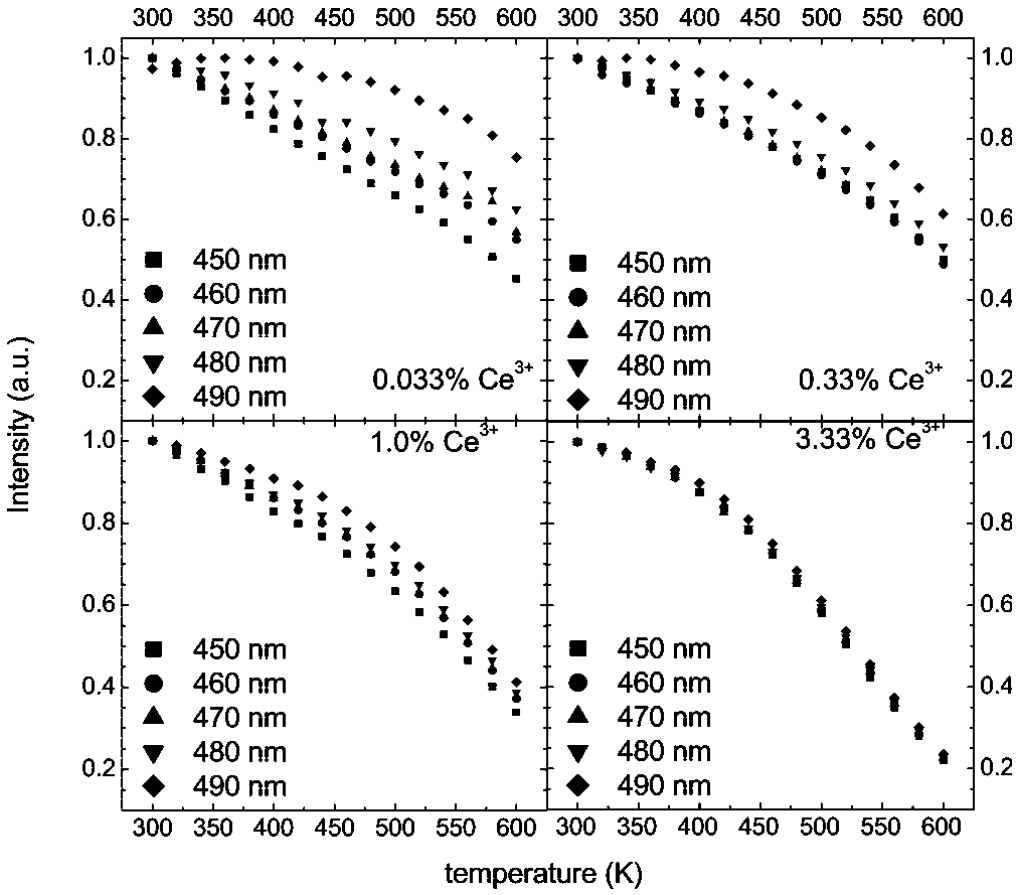

Figure 16: Temperature dependence of the integrated emission intensity for Ce:YAG with Ce content 0.033%, 0.33%, 1.0%, and 3.33% taken at the five excitation wavelengths indicated. Cited from [64]

3.1.6. Lattice constant

Lattice constant plays key role for epitaxial growth of crystal. It is very important to closely match lattice constant a of the substrate and layer. The lattice constant for the garnet substrate can be easily measured or found in literature. However, lattice constant of the layer must be estimated based on the desired composition. It was shown, that the constituent ions radii have great impact on lattice constant [65] (example molecular models with real lattice constant can be seen in Figure 17). Estimation calculations were based on work of Strocka [66]. There was derived an empirical formula for the assessment of lattice constants of oxide garnets. For a garnet with general molecular formula $(C_{3-x}\, C'_x)\ (A_{2-y}\, A'_y)\ (D_{3-z}\, D'_z)\ O_{12}$ is assumed, that the average cation radii for dodecahedral site occupation r^{VIII}, for octahedral site occupation r^{VI}, and for tetrahedral site occupation r^{IV} can be derived from equations:

$$r^{VIII} = r_C^{VIII} + \frac{x}{3}\left(r_{C'}^{VIII} - r_C^{VIII}\right)$$

(3.1)

$$r^{VI} = r_A^{VI} + \frac{y}{2}\left(r_{A'}^{VI} - r_A^{VI}\right)$$

(3.2)

$$r^{IV} = r_D^{IV} + \frac{z}{3}\left(r_{D'}^{IV} - r_D^{IV}\right)$$

(3.3)

and the lattice constant, if substitution occurs simultaneously on different lattice sites, depends on the average cation radii r^{VIII}, r^{VI} and r^{IV} and on the compositional parameters x, y, and z, respectively:

$$a = b_1 + b_2 r^{VIII} + b_3 r^{VI} + b_4 r^{IV} + b_5 r^{VIII} r^{VI} + b_6 r^{VIII} r^{IV}$$

(3.4)

In the work [66] were also derived values for coefficients $b_{1\text{-}6}$ from the best fit of correlation between calculated lattice constants and measured lattice constants (b_1 = 7.02954, b_2 = 3.31277, b_3 = 2.49398, b_4 = 3.34124, b_5 = - 0.87758, b_6 = - 1.38777). For multiple substitutions, the equations (3.1), (3.2), (3.3) can be modified by adding parts with adequate compositional parameters. It is assumed that with increasing complexity, the accuracy decreases [66].

For acquiring data about ion radii of substitution elements was used Database of Ionic Radii [67] that was originally based on work [68].

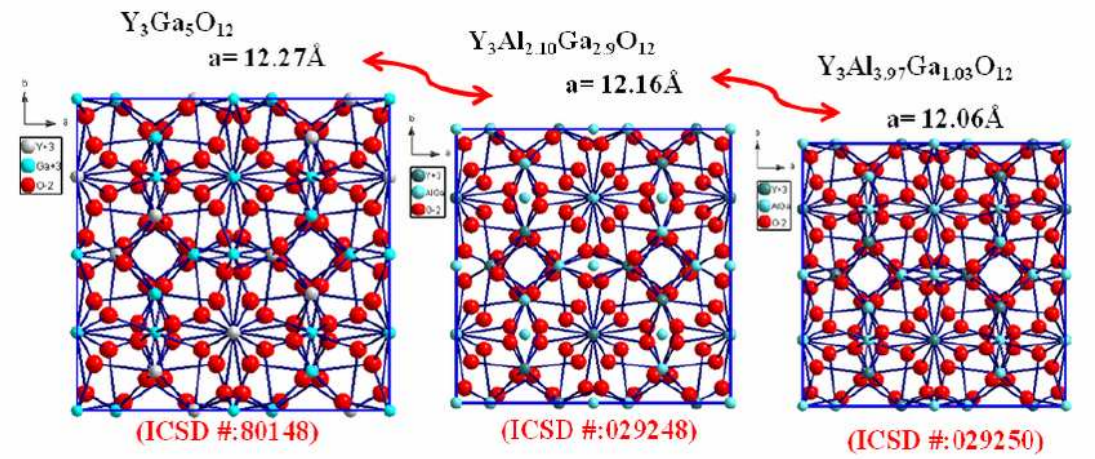

Figure 17: Lattice constant evolution in Ga substituted YAG. Cited from [69]

3.2. Yttrium oxyorthosilicate

Yttrium orthosilicate (Y_2SiO_5), Lutetium orthosilicate (Lu_2SiO_5) and transitioning $(LuY)_2SiO_5$ have been recently intensely studied for their promising features. The light yield of Ce doped crystals is comparable to the NaI(Tl) and when optimized, the energy resolution is better than PWO ($PbWO_4$) can provide [70]. Ce^{3+}-doped Lu_2SiO_5 (Ce:LSO) [71] and Ce:LYSO [72], have been developed as promising scintillators for positron emission tomography (PET). In this work are presented results on Ce and Tb doped YSO single crystal layers.

3.2.1. Crystallographic structure

Yttrium orthosilicate has a monoclinic biaxial crystal structure which belongs to the C2/c (C6 2h) space group [73]. The analogous LSO structure is depicted in the Figure 18. The base molecule structure consists of SiO_4 tetrahedra and Lu atoms bonded via oxygen atoms and forming an distorted tetrahedron with them [74]. There are two different sites of C1 symmetry surrounded either by 6 oxygen ligands and one non-Si bonding oxygen (Lu1, see Figure 18) , or 7 oxygen ligands with two non-Si bonding oxygen atoms (Lu2, see Figure 18). Existence of two possible sites is important as the dopant rare earth ions can enter both. Ce-doped LSO and YSO has been intensively studied for use in various applications [75], for example in medical imaging of positron emission tomography (PET) [76]. The two Ce centers in symmetry sites (Ce1 / Ce2) have different luminescence characteristics clearly distinguished below liquid nitrogen temperature as shown in [77]. The same is valid for the Ce-doped YSO host [77]. The density of LSO is 7.4g/cm^3 [75], the density of YSO is 4.54 g/cm^3 [75]. Pure LSO and YSO crystal is colorless.

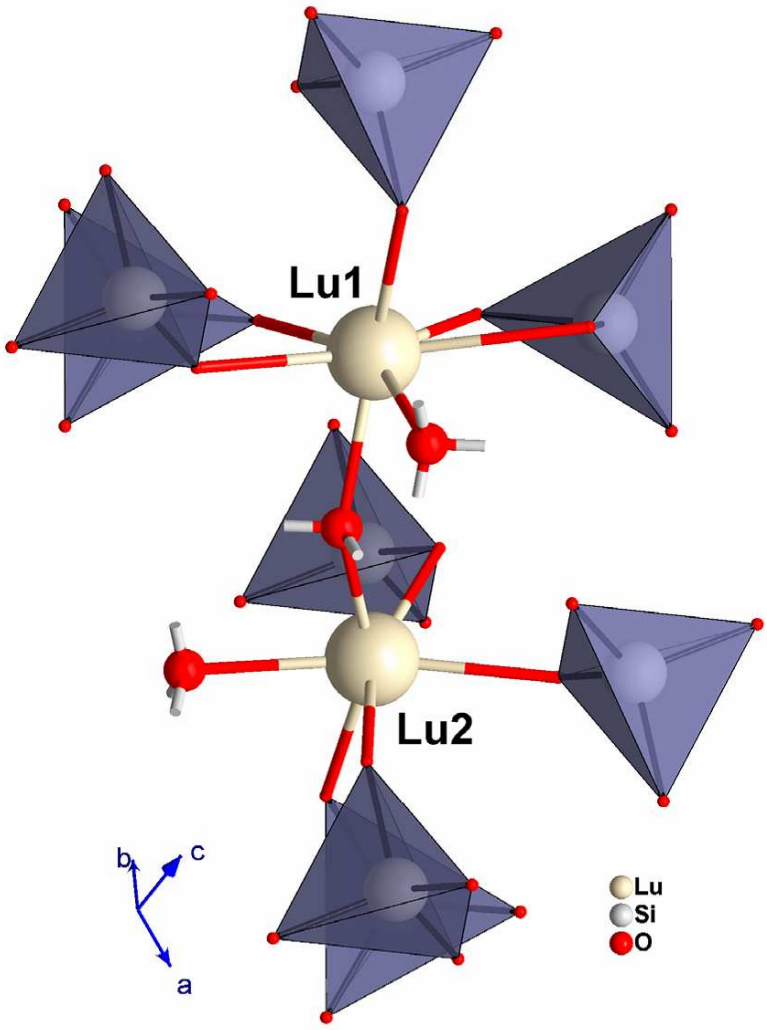

Figure 18: Geometrical representation of structure of the LSO crystal lattice with two Lu sites is shown, surrounded by $Si0_4$ tetrahedra. There are three oxygen ions forming an OLu_4 tetrahedra (depicted as red marbles with cut bonds) and do not create a Si-O bond. The site of Lul has one such oxygen, Lu2 site two; cited from [19]

3.2.2. Cerium doping

The emission spectra of Ce:LSO and Ce:LYSO have the strongest emission peak at around 420 nm at RT. There are two distinct types of emission and correlated excitation spectra of Ce^{3+}. It is a consequence of the existence of two sets of not identical sites mentioned above [59, 60] (excitation spectra at low temperatures are shown in Figure 19). On the contrary to the Ce:YAG or Ce:LuAG, the scintillation decay of Ce:LSO and Ce:LYSO has only one component with decay time that is longer in comparison to the photoluminescence decay time (35 ns). This is due to the lack of shallow electron traps in silicates when compared to the aluminum perovskite and the garnet host [61].

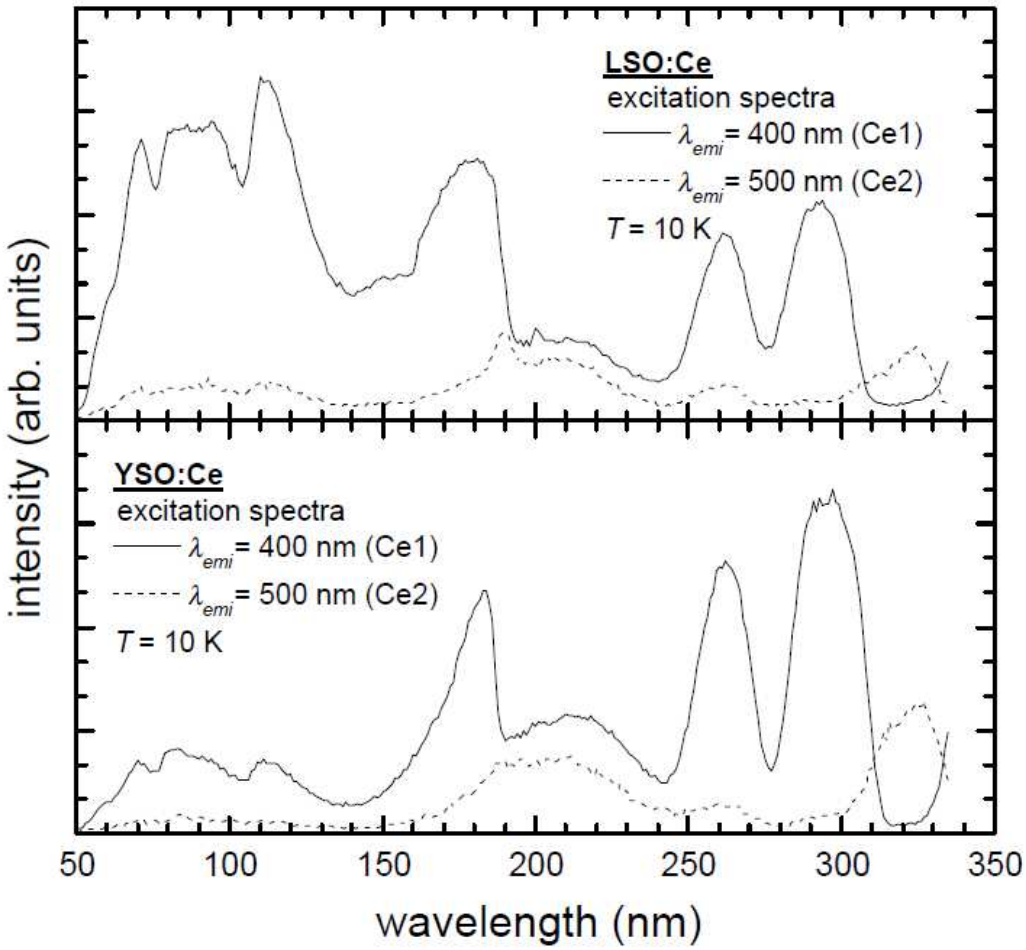

Figure 19: Excitation spectra of the Ce ions at emission wavelengths for both occupational sites in doped YSO and LSO crystals at liquid helium temperature (grown by Photonic Materials Limited, Scotland), cited from [77]

Further improvement of the scintillation performance can be achieved through oxidizing annealing as reported in [78-80]. Significant improvement of X-ray excited scintillation was observed, when Ca^{2+} and Mg^{2+} ions were used in codoping. This is believed to be an effective way to reduce oxygen vacancies significantly, that are normally acting as shallow traps. The results achieved by codoping are explained in [78] by overall increment of Ce^{4+} ions and in [81] by reduction of shallow traps. The reported afterglow is reduced and the light yield is higher.

3.2.3. Terbium doping

The spectra of the terbium in YSO lattice have characteristic four bands with peaks at 488 nm, 542 nm, 584 nm and 620 nm. They are comprised of two main radiative recombination channels and both are occurring between the excited ^5D and fundamental ^7F levels. Figure 20 of analogous crystal of LSO shows that $^5D_3$ to ^7F_J radiative transitions (where J goes from 1 up to 6) has structured emission placed in the UV range from 375 nm to 425 nm. Also the $^5D_4$ to ^7F_J transitions display a group of bands with structure in the range from 475 nm to 625 nm with the main emission band peaked at about 545 nm [82-85]. Transitions from the $^5D_3$ level in the UV are quenched due to cross-relaxation processes at higher Tb^{3+} concentrations. This is shown in an inset graph in Figure 20. The Tb:LSO emission spectrum is peaked at around 540 nm. The PL measured at 542 nm has decay time less than 2 ms and its concentration dependence is shown in Figure 21 in the right graph [85]. The relative ratio of the green and UV spectral components can be changed by variation of Tb concentration. This is allowed by an efficient energy transfer mechanism between the excited ^5D levels and it depends on the host crystal structure [38, 65, 69].

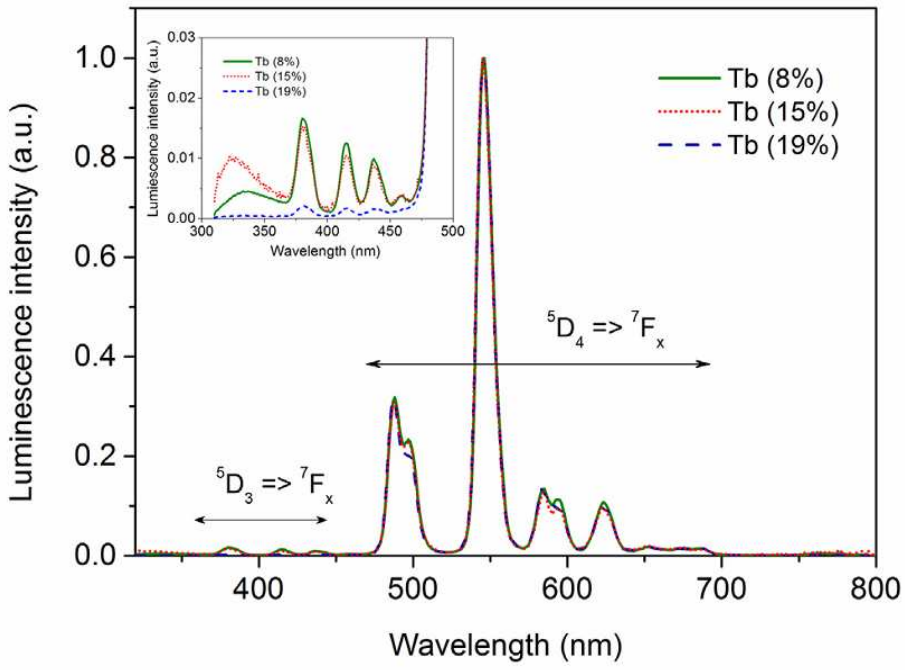

Figure 20: Photoluminescence emission spectra of LSO at RT, λ_{exc} = 236 nm, inserted magnified spectra of quenched transitions from $^5D_3$ to ^7F_x (concentrations are given in molar %, cited from [85])

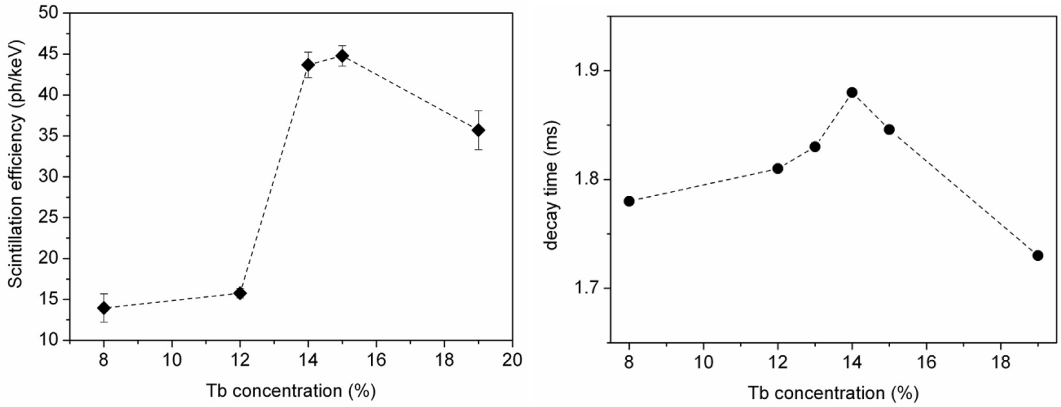

Figure 21: The left graph shows the dependence of scintillation yield on Tb concentration for Tb:LSO, the right graph shows the dependence of decay time on Tb concentration (cited from [85])

3.3. LPE technique

All samples of epitaxial garnet films were prepared by liquid phase epitaxy (LPE) using standard isothermal dipping technique. They were grown from $PbO\text{-}B_2O_3$ and $BaO\text{-}B_2O_3\text{-}BaF_2$ fluxes by this technique. Melt compositions were based on previous intensive work on iron garnets [86]. Core knowledge on behavior of these composite melt solutions was acquired mainly from [49, 87-94].

In the work of Blank [92] $PbO\text{-}B_2O_3$ fluxed melt system is characterized for growth of thin film single crystal iron garnet $(\Sigma Ln)_3Fe_5O_{12}$. There were described most important properties of this flux. Main advantages are dislocation free growth and when supercooled, flux is without spontaneous nucleation of garnet. For initial melt estimation and analysis of the multicomponent system was used simplified scheme of pseudo ternary system $PbO\text{-}Y_2O_3\text{-}Fe_2O_3$ (see Figure 23). The preferred crystal phase can be deduced from this diagram according to overall melt composition. The influence of lattice mismatch was also studied there. Critical lattice mismatch was determined from several substrate materials with different lattice constants and the temperature and substrate orientation dependence was confirmed. Deeper understanding of segregation and phase formation phenomena is developed in work of Chani [95]. Several cations were studied under same conditions (achieved by dissolving of equal amount of those cations in the experiment). The target structures of iron $(\Sigma Ln)_3Fe_5O_{12}$ and gallium $(\Sigma Ln)_3Ga_5O_{12}$ garnets were grown from $PbO\text{-}B_2O_3$ fluxes. These samples were then analyzed by EPMA. The segregation coefficient was determined for each of the cations from measured content (see Figure 22). Further $PbO\text{-}B_2O_3$ flux development and the possibility of Ce or other rare earth (RE) doped YAG growth was introduced by Robertson in [49, 93]. The RE ions that were part of mentioned studies are Eu, Tm, and Tb. There are also mentioned problems with high Ce doping, like pit creation, we also encountered. The cause was

identified in melt deterioration caused by cerium oxide crystallization when Ce was overdosed. Its content in layers was saturated and the particles of cerium oxide adhered on substrate as a seeds for pits.

In melts based on PbO, despite all advantages, occurs one main problem. It is the contamination of samples by Pb^{2+} ions. One possible alternative is the use of BaO based flux. The BaO-B_2O_3-BaF_2 fluxes and their use for garnet growth are researched in detail by Capper [89] and others [91]. These fluxes are praised for relatively low viscosity (compared to flux without BaF_2), low rate of interaction with platinum crucibles, low density, high solubility for garnet constituents, and low degree of solvent ion incorporation into the layers. Additionally, it is possible to get substantially higher Ce concentration into the sample than in PbO fluxes or Czochralski grown crystals [96]. The disadvantages is the increased volatility caused by BaF_2 addition, and the high viscosity of $Y_3Al_5O_{12}$ solutions compared to the solvents [90]. Observed high surface tension is a disadvantage for film growth by liquid phase epitaxy. High viscosity and also great surface tension of the BaO flux are both responsible for big amount of flux remaining on samples. It can cause strain big enough to crack whole sample. Stability field diagram of simplified three-phase system for BaO flux is in Figure 23. Melt viscosity is also connected to dynamic effects in growth process. Simulations of Czochralski growth process shown in Figure 24 imply that the rotation speed is also very important factor for optimal growth.

3.3.1. PbO - B_2O_3 flux system

In the center of attention for PbO-B_2O_3 flux were the growth conditions and aging of the melt. The PbO forming the core of this system is highly volatile at elevated temperatures, especially over the saturation temperature (approx. 1040°C). We studied the influence of melt composition on:

- growth temperature (seeking saturation and optimal growth temperature from growth rates, example shown in Figure 27)
- crystallographic properties (lattice mismatch and its compensation, XRD measurements)
- layer composition and impurities (growth temperature, supercooling and corresponding growth rate)

The melt for each of the series was prepared with different composition. For the garnet LuC series, there were total 10 melts. The differences were in Ce (from 0 to maximal possible) and garnet oxides (2 to 4 mol. %) concentration, ratio between Lu and Al. From each melt were created several samples at various temperatures. The 2LuC and 8LuC series were grown with high lattice mismatch. The segregation coefficient of Ce ions in the melt is rather low, so there was high excess of CeO in it.

Optimal saturation temperature was at 1000°C and temperature of supercooling between 2 to 5 K. The biggest drawback is slow growth and lower Ce concentration. Great advantage is less Pb ions. High supercooling means quick grow and very high Pb content.

3.3.2. BaO - B_2O_3 - BaF_2 flux system

This is very complex melt system consisting of 5 components. The aim was to find a blend suitable for LPE growth. Finding the right composition for given saturation temperature was tedious work. Major drawbacks when compared to the PbO flux were high viscosity, which is growing with supercooling. It also causes slower growth and most importantly problems with homogeneity of melt. Main reason for use of this system is total absence of Pb ions leading to better scintillation properties. The segregation coefficient of Ce ions in the melt is rather low too, so there was high excess of CeO in it.

Optimization was done on 14 series of Ce doped garnets. The melt for each of the series was prepared with different composition. The differences were in Ce (from 0 to maximal possible) and garnet oxides (18 to 22 mol. %) concentration and ratio between each of BaO - B_2O_3 - BaF_2 flux component. The saturation temperature for series from 1 to 10LBC was in range from 950 to 1100°C and for 11 to 14LBC from 930 to 1070°C. Optimal growth temperature was 1030°C and higher.

This flux melt system was optimized. The 11LBC series and further were grown at optimal conditions.

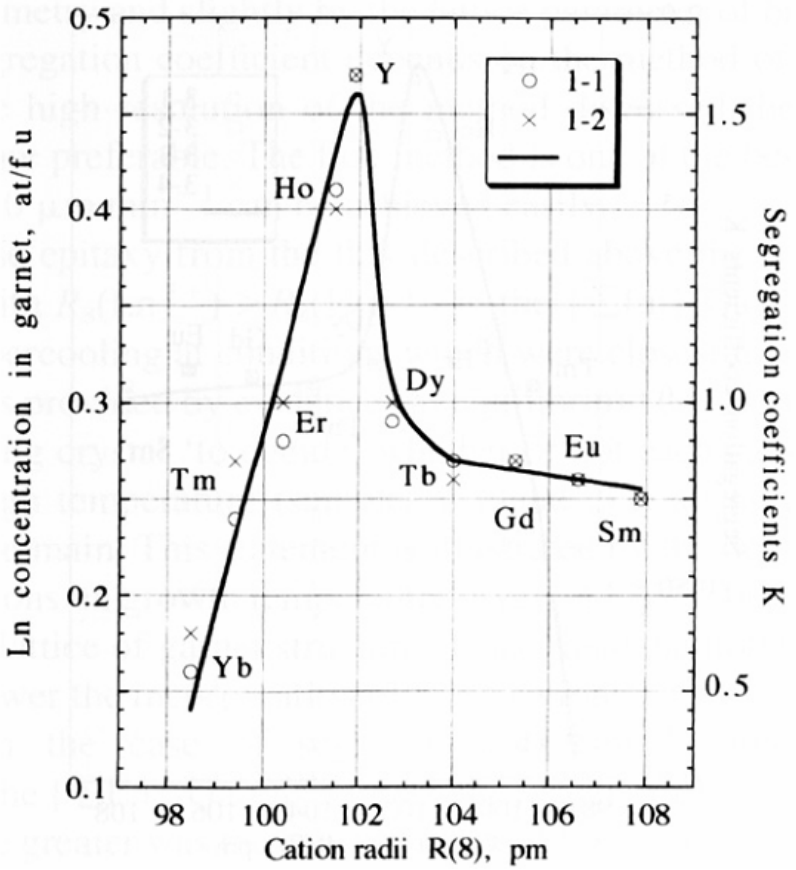

Figure 22: Dependence of concentration (in atoms per formula unit, p.f.u.) and segregation coefficients of rare earth elements from Lanthanides group - Ln^{3+} in the iron garnet $(\Sigma Ln)_3Fe_5O_{12}$ films as a function of cation radii. The films were grown from melt containing equal amounts of 10 rare-earth cations. Different symbols correspond to different samples grown from the same melt. Cited from [95]

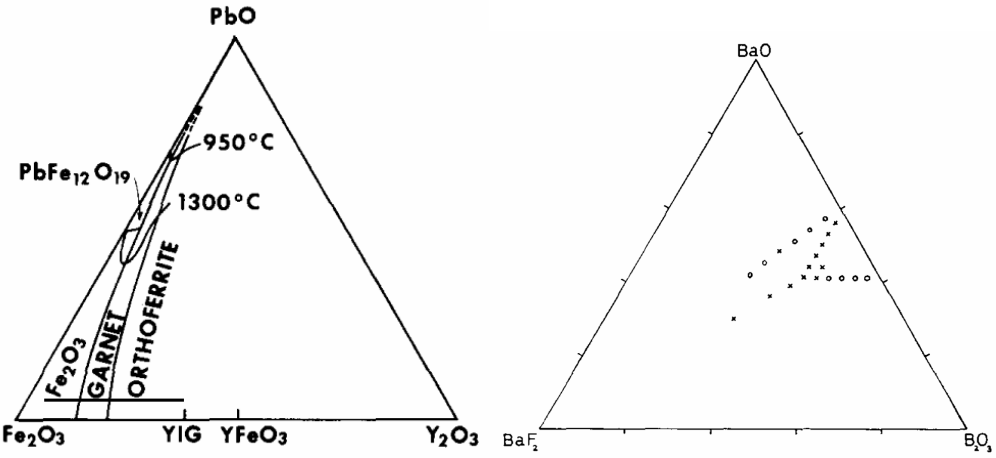

Figure 23: Left is simplified pseudo ternary representation of $PbO\text{-}B_2O_3$ flux system stability field for crystallization of iron garnets (cited from [92]) and right is $BaO\text{-}B_2O_3\text{-}BaF_2$ flux system of $Y_3Al_5O_{12}$ and (x) indicates garnet phase present; (O) garnet phase absent (cited from [89])

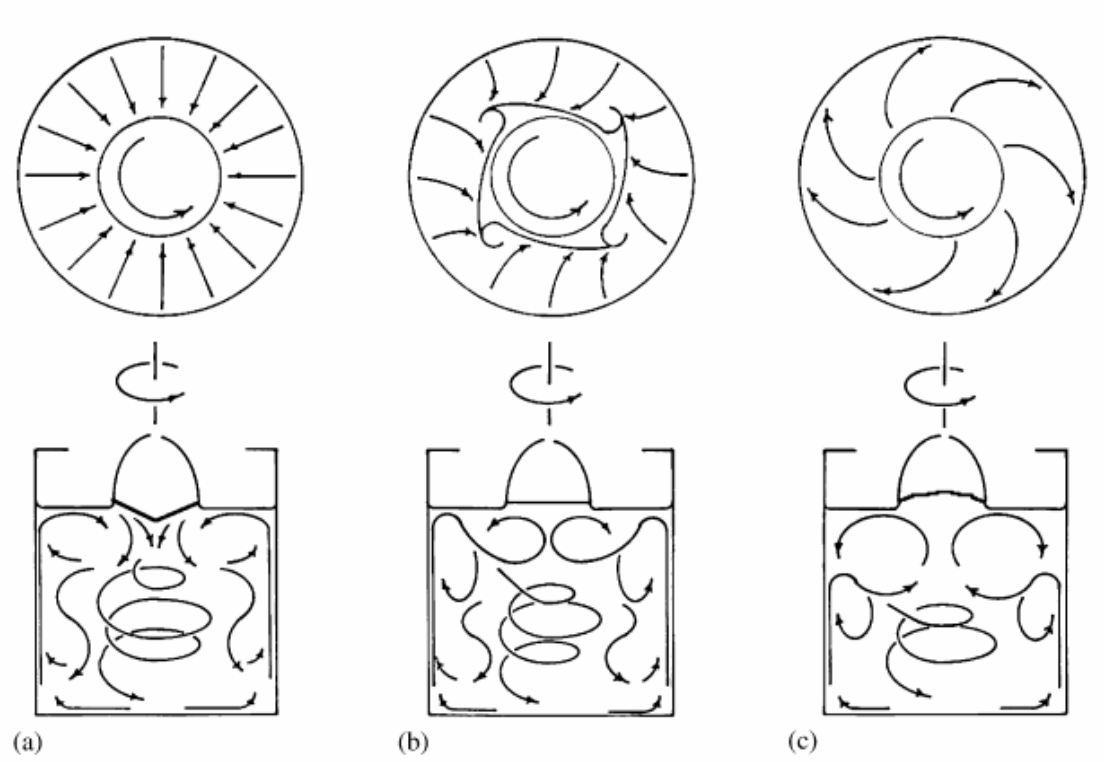

Figure 24: Crystal surface dependence on melt flow in water-glycerin simulation for a- slow rotation, b - moderate rotation, c - fast rotation (cited from [97])

3.4. Growth conditions

We used single crystalline substrates of YAG, LuAG, gallium gadolinium garnet (GGG) and calcium gallium gadolinium garnet (CGGG) with crystallographic orientations (111) or (100) for growing the garnet layers and YSO and Ce:YSO substrates with crystallographic orientation (010) for growing the oxyorthosilicate samples. All used substrates but GGG were from Crytur Ltd., Turnov, Czech Republic. The substrate diameter was mostly 20 mm. Some substrates were only 12 mm in diameter (Ce:YSO). Substrate material was chosen according to suggested layer composition and its lattice constant. Epitaxial growth is very strongly dependent on match of lattice constants between the layer and the substrate as mentioned above. Best growth is achieved when mismatch is very small (less than one tenth of percent). Larger mismatch prevents homogeneous growth or any growth at all (will be shown in further detail on Ce:LuAG samples in next part). Lattice constant estimation of grown layers was calculated according to equation (3.4). Films were grown from supercooled melt solution (see Figure 25) at growth temperature T_g. Substrates were rotated when submerged at 120 rotations per minute (rpm) and the rotation direction changed every 4 seconds in order to achieve a homogeneous growth. The sample was pulled up from the melt solution and slowly drawn out of the furnace (see Figure 26) at the end of growth time (t_g). Rapid spinning at

800 - 1000 rpm cleaned residual flux remaining on the sample and holder. The spinning speed varied in accordance to viscosity of the melt. The flux cannot be completely removed this way. The remaining flux must be chemically cleaned. Final cleaning was done in nearly boiling concentrated nitric acid. Initial materials used for melt preparation were of 5N purity. The thickness of grown layers was determined based on weight increase. The specifics on growth conditions and used melt compositions are in more detail discussed in articles [86, 96, 98, 99].

The LPE strongest point is significantly lower growth temperature than the Czochralski growth. From thermodynamics point of view, it can be assumed that less crystal defects will occur. The range of growth temperatures was from 930 to 1080°C. It is much lower temperature than the Czochralski growth requires (above 2000°C). On the other hand, the growth rates are significantly lower. They were from 0.04 to 1.8 µm/min and are strongly dependent on the flux, its overall composition and growth temperature. The dependence of growth rate on temperature is shown in Figure 27. These were measured for Ce:LuAG layers grown from $PbO - B_2O_3$ flux. All series show decreasing tendencies with increasing temperature. When extrapolated, the cross section of the curves with zero growth rate indicates the saturation temperature. The difference between growth and saturation temperature is called supercooling. The epitaxial films were grown from supercooled melt in the region from 3 to 60 K. Grown layers thickness ranged from 2 to 24 µm. Higher Ce content can be achieved in the samples from BaO fluxes than what is possible in Czochralski single crystals.

Epitaxial films prepared from the PbO flux have excellent crystallographic properties (will be shown in next part), and high optical quality surface. However, layers from the BaO flux were obtained with superior luminescent properties. These and other properties will be discussed in latter section.

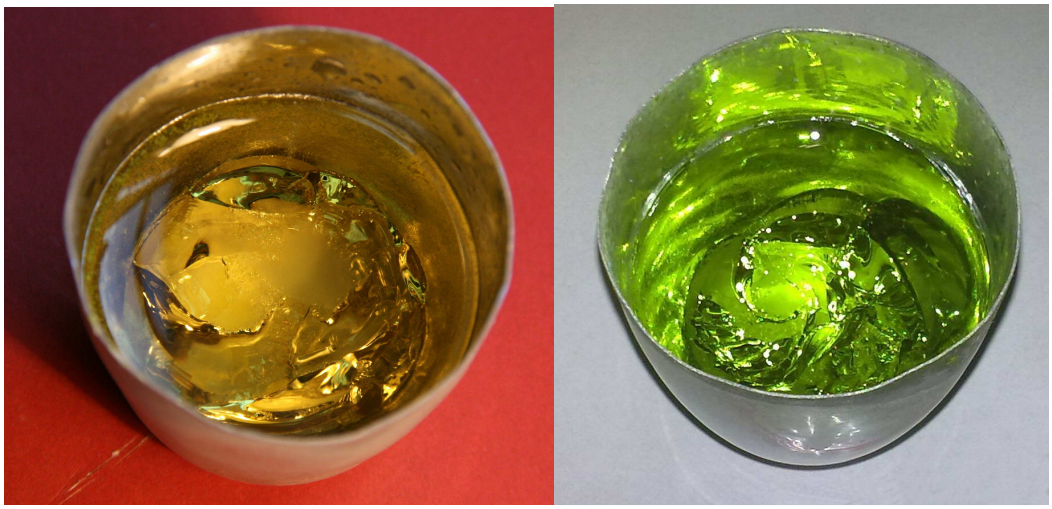

Figure 25: $BaO-B_2O_3-BaF_2$ fluxes prepared for growth at room temperature for Ce doped garnet samples on the left and for Pr doped samples on the right

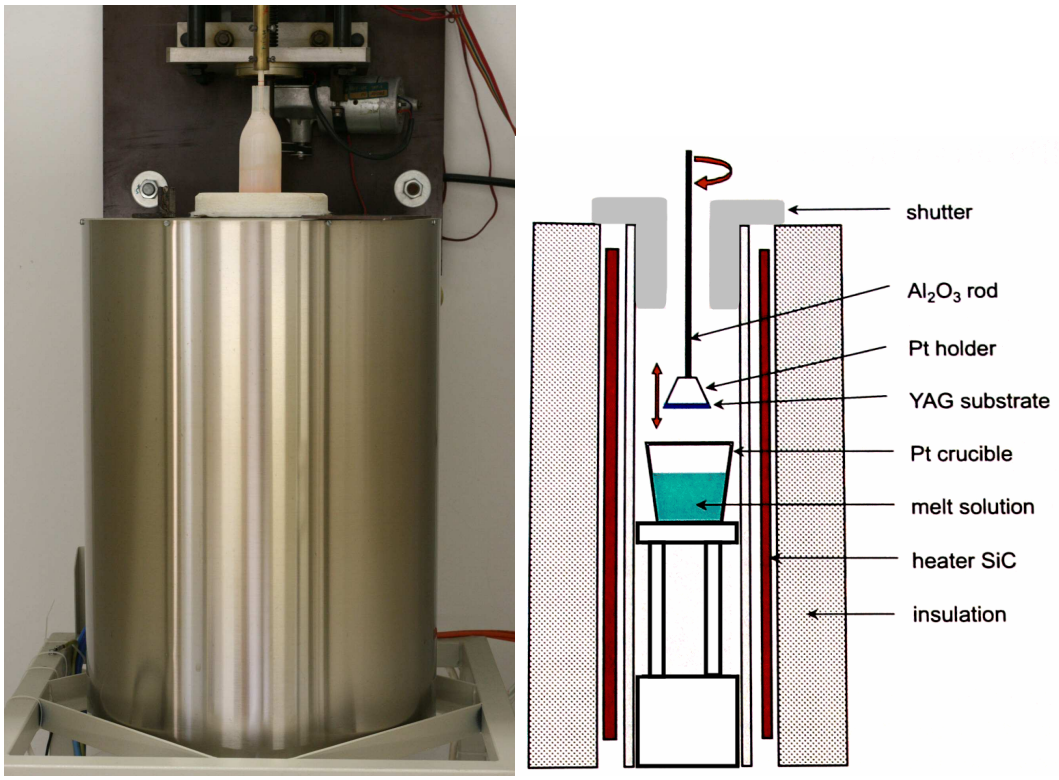

Figure 26: Photo of furnace for LPE during growth with sample inside, under quartz shielding on the left and its internal structure depicted approx. in scale 1:1 on the right

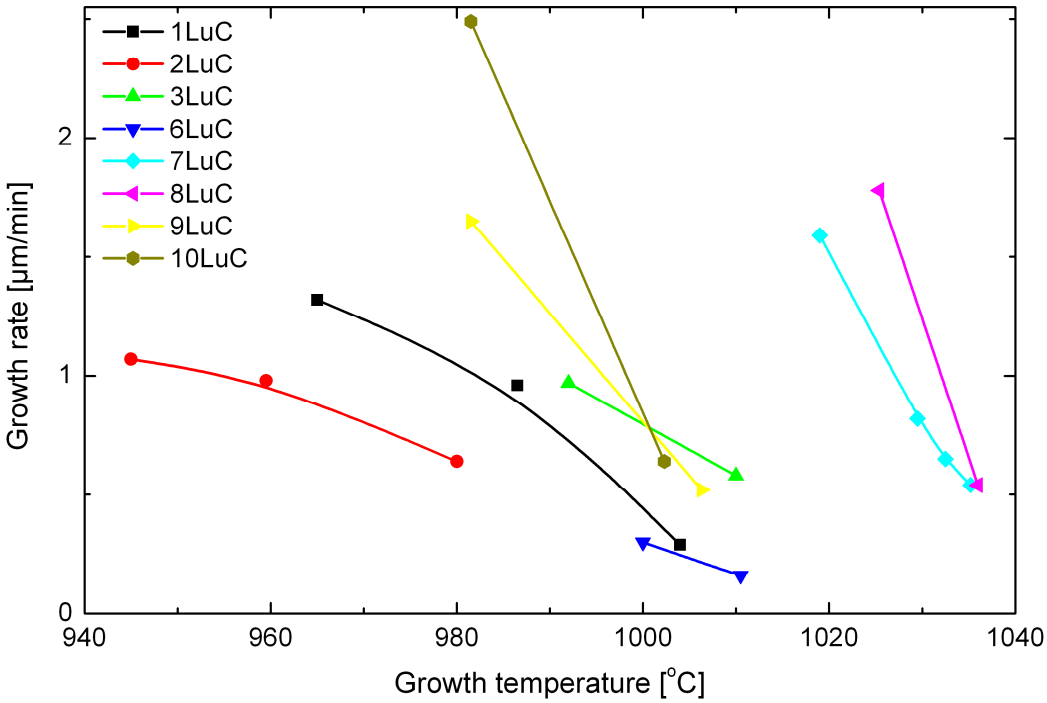

Figure 27: Growth rate of LuAG films as a function of growth temperature (supercooling). The graph shows various melt compositions used to grow Ce:LuAG layers from PbO–B_2O_3 flux.

3.5. Influence of melt

The PbO flux is responsible for increased absorption at wavelengths shorter than 280 nm and it was studied in further detail in [39-41]. It is its most negative feature. However, no absorption at lower energies was detected. The increased absorption in the UV mentioned above originates mostly from impurities caused by Pb^{2+} ions. They originate from the flux. The absorption band near 262 nm has been assigned to the internal allowed transitions of Pb^{2+} ($^1S_0 \rightarrow {}^3P_1$) [100]. The charge transfer between Pb^{2+} and the conduction band occurs at higher energies [100]. The Pb^{2+} ions create shallow trap states causing decrease of light yield. The PbO grown films are practically not transparent below 230 nm (see Figure 28). According to the GDMS analysis, we can estimate the content of Pb ions in samples to be somewhere in the range of 30 - 100 ppm. The contamination depends on the growth temperature. The higher the growth temperature is, the less Pb^{2+} ions are in the layers [93]. Their concentration also steeply decreases with the supercooling approaching the saturation temperature. Unfortunately, the same goes for the doping by ions like Ce [93] and Pr.

The BaO flux also shows an increase of absorption in the UV region. The impurities incorporated from the BaO flux do not quench luminescence (will be shown in next sections).

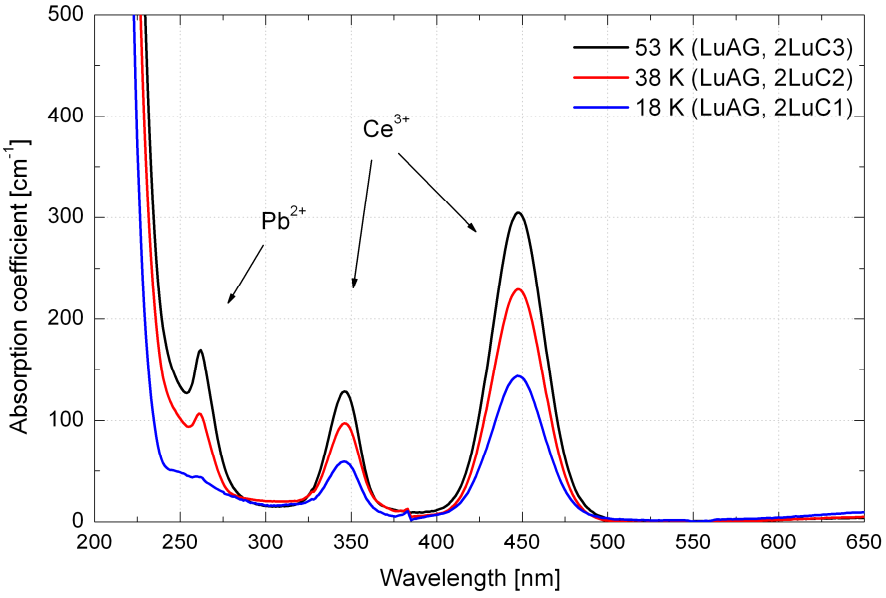

Figure 28: Supercooling influence on $PbO–B_2O_3$ flux grown samples absorption coefficient spectra. Absorption rises as supercooling temperature increases (from 18 K up to 53 K supercooling). Indicated Ce dopant peaks and Pb main absorption. LuAG substrate and layer (homoepitaxy, see Table 2) shown also in [99]

4. Experimental setup and measurements

4.1. Characterization of layers

4.1.1. Properties of epitaxial films

Samples grown from the PbO flux have mostly optical quality surface with some minor defects. The surface of films from the BaO flux was typically of lesser quality. Main disadvantage of BaO flux is significantly higher viscosity, surface tension and its homogeneity. However, photoluminescence (PL) properties of BaO grown layers tend to be better compared to the ones grown from PbO. These differences will be discussed. The optical absorption was measured, along with the PL excitation and emission spectra, and the PL decay kinetics for all films. The radioluminescence (RL) spectra and the photoelectron yield were measured by our colleagues at Institute of Physics of the Academy of Sciences of Czech Republic (ASCR). All presented measurements were carried out at room temperature.

4.1.2. Garnets sample quality

We were using several different substrates (see chapter 3.4) in order to match the lattice constant of the substrate and layer. The growth can be categorized as homoepitaxial (see Figure 29 left) or as heteroepitaxial (see Figure 29 right) based on difference in lattice constant of substrate and layer (called lattice mismatch Δa). With homoepitaxial growth, the difference is very small ($\Delta a < 0.1$ %). The heteroepitaxial growth occurs at greater lattice mismatch. A stress-releasing layer emerges in heteroepitaxial growth because of lattice mismatch (shown in Figure 29). This transient layer is crucial. The chemical composition of substrate to layer transition is critical issue. Its contamination by impurity ions from the flux and presence of other defects has great impact on further growth. The lattice constants of the LPE layers were measured by XRD method (see Figure 30). These measurements were used to calculate the lattice mismatch. For low lattice mismatch, < 0.02 Å, the transient layer is usually sharp and it is tens of nanometers thin (see left side photo from optical microscope in Figure 29). The morphology of the transient layer gets more complicated for greater lattice mismatch. Pictures in Figure 29 show the edge of samples cleaved perpendicularly to the surface, showing interface between film and

substrate for both low (the left photo) and high (the right photo) lattice mismatch. Sharp film to substrate interface is hardly observable at homoepitaxially grown Ce:LuAG - LuAG system (the left photo), where lattice constants of the film and substrate are nearly equal. The optical contrast between film and substrate is very weak due to almost identical refractive index and composition. On the other hand, for the heteroepitaxially grown Ce:LuAG - YAG system is the lattice mismatch rather high. The film to substrate interface is steep and thick. Columnar like structure of the layer oriented perpendicularly to the interface is observed. The morphology of the transient layer seems to be critical to physical stability of samples, especially for micrometer thick films.

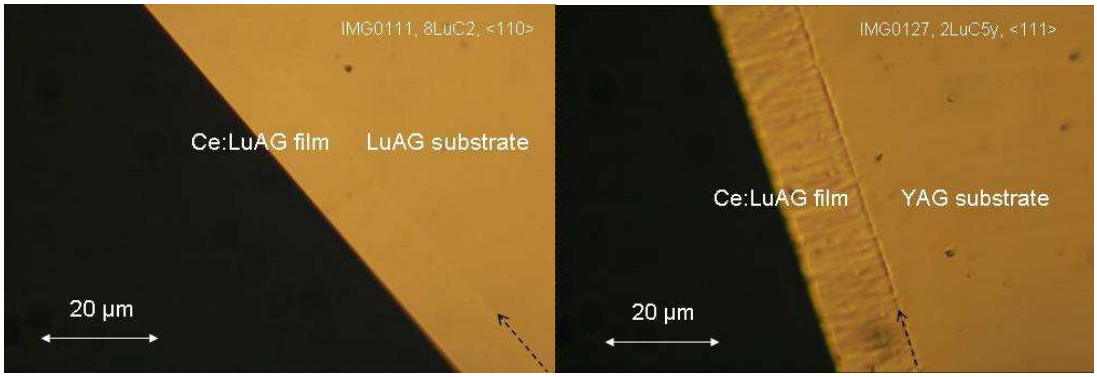

Figure 29: Microscope photography of the edge of cleaved sample grown from PbO flux; the arrow indicates the layer/substrate interface. On the left is homoepitaxially grown Ce:LuAG sample on LuAG substrate; lattice mismatch $\Delta a < 0.02$ %. On the right is heteroepitaxially grown Ce:LuAG sample on YAG substrate; lattice mismatch Δa is 0.8 % (for details see [101])

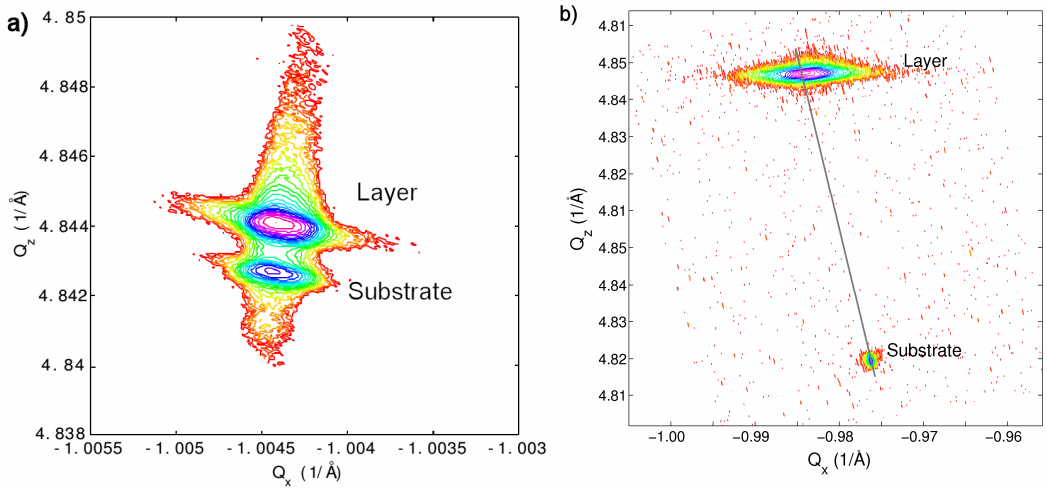

Figure 30: Asymmetrical reciprocal maps of 664 diffraction of Ce:LuAG samples both grown from PbO flux showing the difference in lattice constant between layer and substrate; z represents direction normal to the layer plane; a) is homoepitaxially grown Ce:LuAG sample 2LuC2; b) is heteroepitaxially grown Ce:LuAG sample on YAG substrate 2LuC5y (see also in Figure 29; for details see [99])

The surface morphology and surface profiles were mapped using the optical microscope. Surface roughness of the films was measured by a non-contact 3D surface profiler Zygo, model New View 5022. It uses scanning white light interferometry to acquire ultrahigh Z-resolution images. Typical surface profile of homoepitaxial Ce:LuAG epitaxial film grown onto high quality LuAG substrate from the PbO flux is shown in Figure 31 a. Rather smooth surface is observed and typical roughness is only a few nanometers. On the other hand, great surface roughness is typical for samples grown with high lattice mismatch. An example is shown in Figure 31 b. The heteroepitaxial growth (like the Ce:LuAG film on YAG substrate, where the lattice mismatch is 0.8 %) produce surface roughness of several hundreds of nm. Such films are matt and scatter light strongly. For few samples, the rough surface was polished and the optical properties were compared with other samples (approx. 3 μm of films were lost). After polishing, a glossy surface was obtained on the polished side.

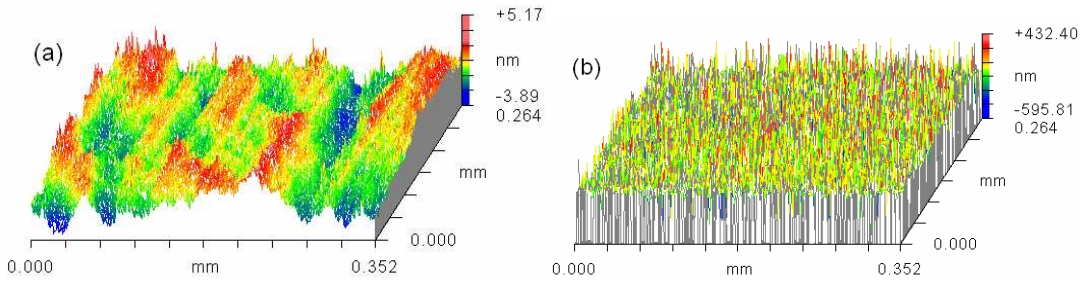

Figure 31: ZYGO interferometric representation of the surface profile a) The left represents surface of Ce:LuAG film on LuAG substrate (homoepitaxy), smooth with surface roughness (z axis) approx. 2 nm is observed; b) The right is Ce:LuAG film on YAG substrate (heteroepitaxy, lattice mismatch $\Delta a = 0.09$ Å), surface roughness approx. 300 nm (for more details see [101])

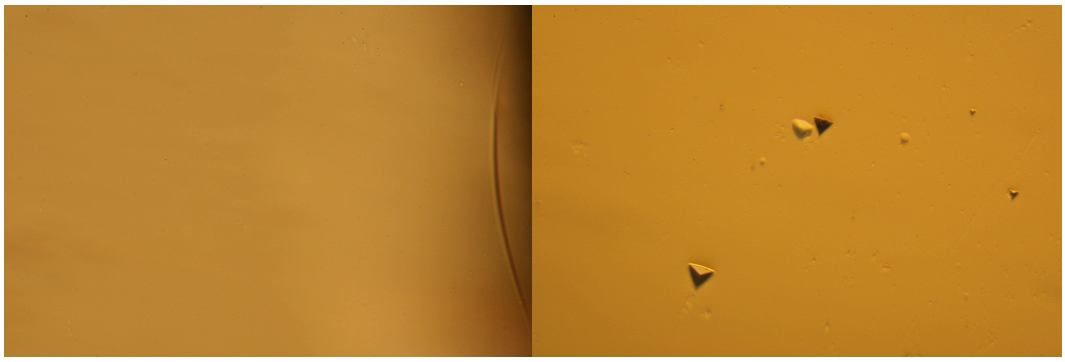

Figure 32: Surface images taken with optical microscope. Ce:YAG films grown on <111> oriented YAG substrate from the PbO flux at magnification of 30x. On the left is surface free of defects (shown scratch at the edge of the sample on the right side of the picture). On the right photography are triangular dislocation pits in the film. These are typical for <111> orientation and originate from the substrate defects or non-dissolved particles floating in the flux. (for more details see [101])

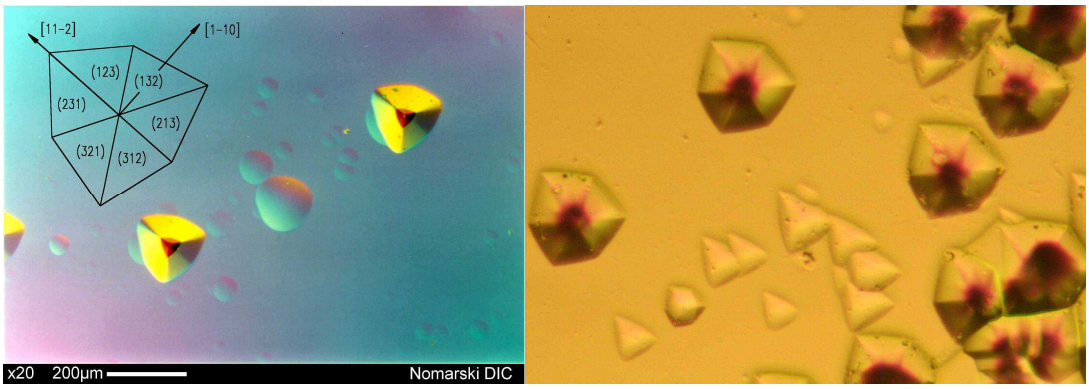

Figure 33: On the left is microscope photography of a typical crystal defect in LPE grown GGG films. The picture was taken with Nomarski differential interference contrast (DIC) (cited from [102]). On the right is a picture of a typical crystal defects in LPE grown LuAG layers grown from BaO - B_2O_3 flux (3LBC2) at magnification 25x. There are triangular dislocation pits as in PbO - B_2O_3 grown samples as well as hexagonal pits.

Surface properties of epitaxial films are strongly dependent on crystallographic quality and final polishing procedure of used substrates. Any substrate defect (dislocations, inclusions, scratches – shown in Figure 34, etc.) is transferred into the LPE film (see Figure 33). Figure 32 shows flawless surface in comparison to triangular dislocation pits observed typically in films grown on <111> oriented substrates. The defects (see in Figure 32 and Figure 33) are of µm dimensions and most probably come from the substrate defects, either intrinsic (dislocations, vacancies, etc.) or induced during the polishing stage by grinding of grains of polishing media. Another possible cause may be particles of another phase (like cerium oxide or perovskite) or oxide powders that did not dissolve and were floating in the flux (because of high viscosity of the solution). Such defects are practically nonexistent in films grown from the PbO - B_2O_3 flux and on high quality, well-polished substrates. However, increased number of pits was observed in films grown from the BaO - B_2O_3 flux. Very high viscosity of BaO - B_2O_3 flux is most probably another cause for defect creation. Another possible source of various defects is contamination by inorganic or organic pollutants of the substrate surface prior to the film growth.

Figure 34: Microscope photography of the LuAG substrate oriented at <111>, etched in sulphuric acid (H_2SO_4) and phosphoric acid (H_3PO_4), magnification 12.5x. Revealed deep defects in form of scratches, induced during the polishing stage by grains of polishing media.

4.1.3. Oxyorthosilicates sample quality

The surface morphology was studied by the optical microscope. Surface quality of YSO epitaxial films is strongly dependent on crystallographic quality and final polishing procedure of used substrates much like the LuAG. Substrate defects are transferred into the LPE layer (see Figure 35). In the left photo in Figure 36 is shown one of the best surfaces of YSO layers. In the right photo is a closer look on typical dislocation pits for YSO samples. Layers were grown on an oriented substrate at <010> face. The pit defects are of µm dimensions. The most probable sources of the defects are quite similar to the garnets grown from BaO flux. They originate either from the substrate (dislocations, vacancies, etc.) or from particles of another phase (like cerium oxide) or remnants of oxide powders that did not dissolve in the flux or from effects caused by high melt viscosity.

Figure 35: Surface image of sample 2S9, magnification 8x taken with optical microscope. Tb:YSO films grown on Ce:YSO <010> substrate from the PbO flux., with defects (shown pit aggregation along substrate defects, looking like scratches, induced during polishing)

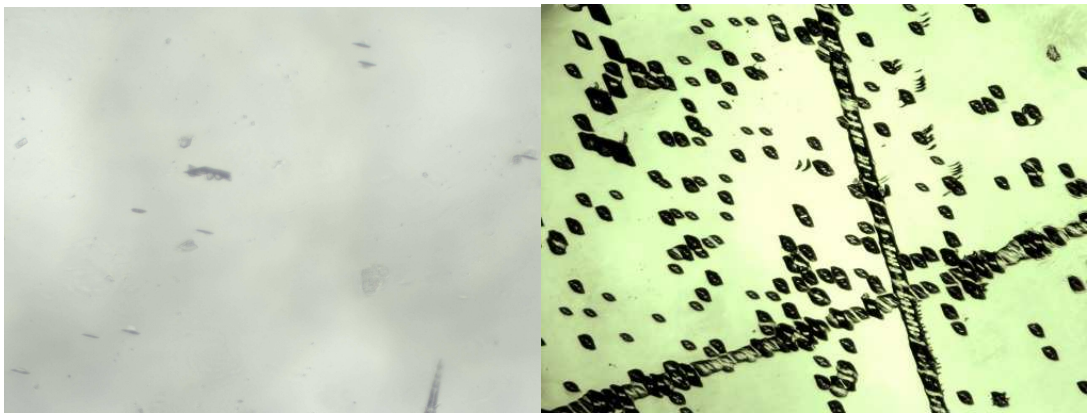

Figure 36: Surface images taken with optical microscope. Tb:YSO films grown on Ce:YSO <010> substrate from the PbO flux. On the left is surface of sample 1S5, magnification 10x, with very few defects (shown scratch at the edge of the sample on the right side of the picture). On the right photography are shown pits in the layer 2S6, magnification 40x. There is also shown pit aggregation along substrate defects (due to scratches induced during polishing)

4.1.4. Optical absorption measurements

The transmittance of all LPE grown samples and reference crystals was measured at room temperature. It was carried out using Perkin-Elmer lambda 12 and later on Specord 350 apparatus. The range was set from the UV at 190 nm to the near infrared at 1100 nm. This measurement provides information about layer contents, especially dopants like Ce and Pr. It is robust method, but less sensitive, when it comes to low absorbing dopants or impurities or highly absorbing or scattering

samples. It is possible to estimate dopant content via comparison of sample and reference sample absorption coefficient. The absorption coefficient can be calculated from the measured transmittance T. This approach was applied to ascertain Ce content in Ce doped LuAG films in the next chapter. In other cases, we calculated only optical density (OD) according to equation:

$$OD = -\log T \tag{4.1}$$

For the purpose of calculating absorption coefficient, we must include transmittance T and layer thickness x to equation (2.1), because the transmittance was measured. By definition:

$$T = \frac{I(\lambda)}{I_0(\lambda)}, \tag{4.2}$$

where I(λ) represent intensity of light passing through the sample and $I_0(\lambda)$ is light intensity entering the sample. The formula for transmittance transforms with reflectivity defined in (2.2) to:

$$T = \frac{(1-R)^2 e^{-\alpha d}}{1-R^2 e^{-2\alpha d}}, \tag{4.3}$$

where d is sample thickness. From here, we can derive an equation for absorption coefficient of the layer α_L by using reflectance R and layer thickness x:

$$\alpha_L = -\ln\left(\frac{-(1-R)^2 + \sqrt{(1-R)^4 + 4(RT)^2}}{2R^2 T x}\right) \tag{4.4}$$

An empirical model for the computation of reflectance based on work [23] was used for wavelength dependence estimation of refractive index in visible and near UV spectral range (see Figure 37). Thus, from equation:

$$R = \frac{(1-n)^2}{(1+n)^2},$$

(4.5)

and by using Sellmeiyer equation:

$$n^2 - 1 = \frac{A_1\lambda^2}{\lambda^2 - B_1} + \frac{A_2\lambda^2}{\lambda^2 - B_2} + \frac{A_3\lambda^2}{\lambda^2 - B_3},$$

(4.6)

and Sellmeiyer coefficients $A_{1\text{-}3}$ and $B_{1\text{-}3}$ from [23], the desired reflectance was obtained in measured range of wavelengths.

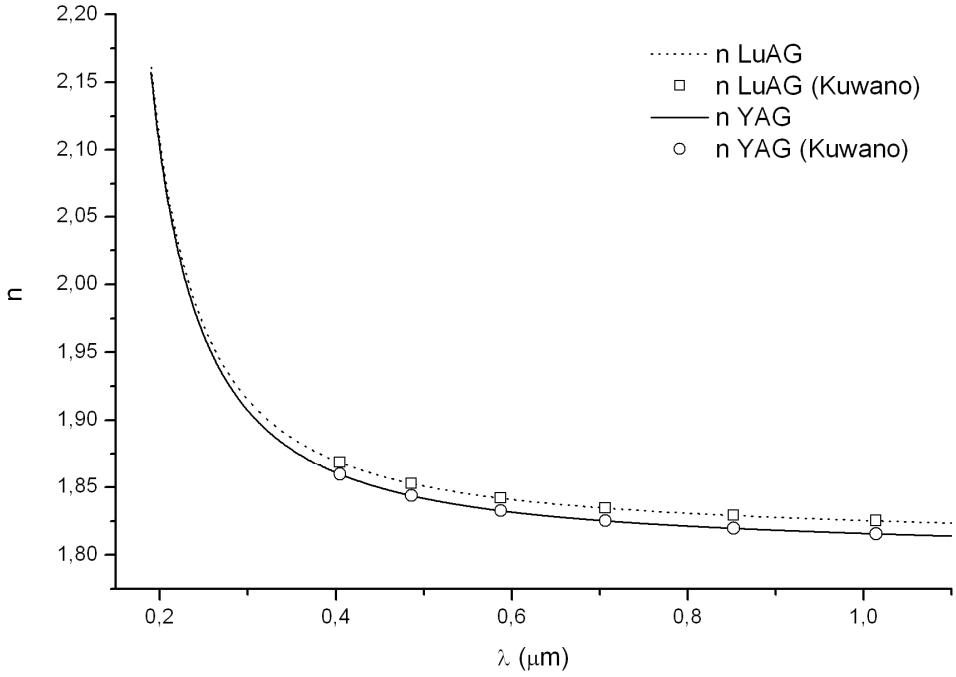

Figure 37: Theoretical refractive index dependence on wavelength calculated based on Sellmeiyer equation and coefficients cited from reference [23] for YAG and LuAG materials

The spectra of the absorption coefficient were computed based on samples specific thickness. We used formula (4.4) with respect to substrate absorption and sample scattering. The scattering was numerically compensated, but not always completely as it was mostly not constant in whole range and sometimes not even linear.

4.1.5. Photoluminescence

Optical excitation and emission spectra were measured on Jobin-Yvon Floromax 3 fluorescence spectrometer. The photoluminescence (PL) is very sensitive method allowing detection of very small quantities of ions. The most limiting factors for its use are only the range, where the material is transparent and wavelength of studied ion emission. Our measurements were in the range from 200 nm to 800 nm. We discovered limitation of this method directly related to our samples. It is caused by garnets relatively high refractive index and its difference between layer and substrate. Waveguide effect emerges and PL light is directed to the sides. Problem emerges when samples with good and poor surface quality are compared. The samples with rough surface emit the PL light more evenly. This phenomenon was compensated by fitting the sample at angle with maximum PL intensity. Despite all precautions, we believe, the maximal error in the PL intensity can be as high as 20 %.

Samples grown from the BaO flux exhibit higher intensity of PL emission compared to the ones grown from PbO. We discovered trace amounts of Ce ions and color centers from oxygen vacancies in LuAG substrates. Observed color centers were unique characteristic of each substrate. Example of the substrate emission is shown in Figure 38.

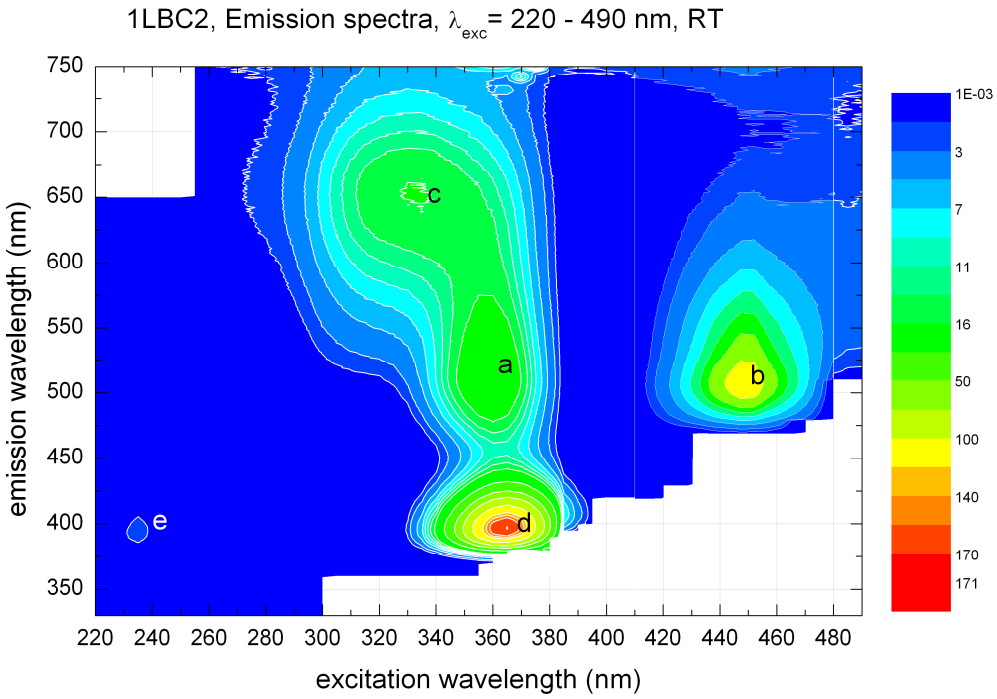

Figure 38: PL excitation and emission spectra of substrate. Czochralski grown LuAG single crystal with trace concentration of cerium (a and b peaks) and intense color centers (c, d and e peaks)

4.1.6. Decay kinetics of luminescence

The PL decay kinetics measurements provide additional information on the impurities and emission centers found in the PL emission. We used our cooperation with ASCR and participated on measurements with their device for measuring fast response of Ce and Pr. It consists of the spectrofluorometer 199S (Edinburgh Instruments). It is equipped with fast nanosecond hydrogen-filled flash lamp (IBH Scotland), or alternatively with ns LEDs as an excitation source. It was also capable, with microsecond xenon flash lamp, to measure a few orders slower response of Tb. The detection part consists of single grating emission monochromator and Peltier-cooled TBX-04 detection module (IBH Scotland) working in time-correlated single photon counting (TCSPC) method. All spectra were corrected for experimental distortion using the apparatus response curve. Deconvolution procedure (Spectrasolve software developed by Ames Photonics) was used as correction method for getting the true decay times, because the fast decay curves are greatly influenced by a finite width of the instrumental response for Ce and Pr.

4.1.7. Measurements with ionizing radiation

4.1.7.1. Radioluminescence

The radioluminescence (RL) spectra were measured at the same device as the PL decay kinetics with X-ray tube as excitation source. The X-ray tube Chirana or Seifert was used for the RL measurements. The range was originally from 200 nm to 670 nm, but after an upgrade of the detection unit, the range was increased up to 800 nm. For possible later comparison of all measured spectra in an absolute scale, the radioluminescence spectrum of the reference scintillation material $Bi_4Ge_3O_{12}$ (BGO) was measured with each batch of samples in one session. The RL was measured under X-ray excitation produced at 10 kV voltage and 50 mA current going through X-ray tube. Low excitation voltage ensures that the X-rays primarily excite the film and contribution of the substrate to the RL spectra is greatly reduced. Waveguide effect pose the same problem as in PL and it was compensated in similar way as in PL measurements.

4.1.7.2. Photoelectron yield

The photoelectron (N_{ph}) yield and the α-excited scintillation response were measured. The source of probing α particle radiation was radionuclide of ^{241}Am (peak energy of α radiation 5.4856 MeV) or ^{239}Pu alpha particle source (with particle energy 5.16 MeV). The dependence of N_{ph} yield as well as energy resolution on the

shaping time was measured. Range was within 0.5 – 10 μs. The experimental setup consists of an hybrid photomultiplier tube (model DEP PPO 475B), an ORTEC NIM model 672 spectroscopy amplifier, and a multichannel buffer in PC. This setup works in pulse-height mode [103, 104]. Radioactive source was placed directly onto sample surface to ensure minimum energy loss of α-particles in the air. Sample was covered in the immersion oil to reduce reflection losses of scintillation light. Complete setup description and parameters of measurements are thoroughly described in [105, 106].

The reason for using α particles to measure scintillation response is simply that we can be sure that all scintillation light comes from the layer and not from the substrate. It is possible to determine the penetration range (depth) for LuAG material R_{LuAG} of α particle using formula [104]:

$$R_{LuAG} = 2.3\times10^{-4}\,\frac{\sqrt{M_{eff,LuAG}}}{\rho_{LuAG}}\,R_{air} \tag{4.7}$$

where $M_{eff,LuAG}$ is effective atomic mass of LuAG, R_{air} is range of α particle in air and ρ_{LuAG} (in $kg.cm^{-3}$) is the density of LuAG. The effective atomic mass $M_{eff,LuAG}$ can be calculated from the following equation [104]:

$$\frac{1}{M_{eff,LuAG}} = \sum_i \frac{\omega_i}{\sqrt{M_i}} \tag{4.8}$$

where ω_i is the weight fraction of the i-th constituent. Range of α particle in the air can be found using its energy E_α by using formula [104]:

$$R_{air}\left[cm\right] = 1.24E_\alpha - 2.62 \tag{4.9}$$

From these equations is evident that the penetration of α particles is rather small. It is slightly above 10 μm in garnet and approx. 40 mm in the air for used radiation source.

4.1.8. X-ray diffraction

Analysis was performed on device PANalytical high-resolution X-ray diffractometer X'Pert Pro MRD (Cu $K_{\alpha 1}$ peak used). The X-ray beam has been conditioned using the x-ray mirror followed by four-bounce Bartels monochromator (4xGe220). Diffracted beam has been registered using the three-bounce channel-cut analyzer (Ge220) and proportional point detector. The XRD measurements were conducted on several samples mainly to determine lattice constants of grown layers and lattice mismatch of layer and substrate. Thorough information on XRD method can be found in [107].

4.1.9. Glow Discharge Mass Spectrometry

Glow Discharge Mass Spectrometry (GDMS) is an analytical technique based on mass spectrometry. It is used to measure trace levels of impurities in conducting or semiconducting solids. The primary advantages of GDMS are its sensitivity (ppt detection limits in some cases), its quantitative accuracy (20% on average) achieved without complicated standardization procedures, and its ability to detect all elements in the periodic table from lithium to uranium at nearly the same sensitivity. More information on GDMS analysis can be found in [107].

4.1.10. Electron Probe X-ray Microanalysis

Electron Probe X-Ray Microanalysis (EPMA) is spatially resolved, quantitative elemental analysis technique, where by bombarding a sample with a focused beam of electrons at high energies (typically 5 - 30 keV), an emission of characteristic X-rays is induced. The X-rays are measured by Energy Dispersive (EDS) or Wavelength Dispersive (WDS) X-ray spectrometers. Typical error is within ± 4 %. Range of detectable elements is from beryllium to the actinides. No harm is done to the sample, except for electron beam damage. Detection limit is approximately 100 ppm for WDS and 1000 ppm for EDS. Typical sampling depth is electron energy dependent (approx. 100 nm - 5 μm). Additional information on EPMA analysis can be found in [107]. A short comparison to other common analytical techniques is shown in Table 1.

Technique	Main information: Elemental	Chem. state	Phase	Defects	Structure	Image	Other	Depth probed (typical)	Width probed (typical)	Trace capability (typical)	Types of solid sample (typical)	Vacuum needed?
Light Microscopy				•		•	•	Variable	0.2 μm	—	All	N
SEM				•		•		sub μm	10 nm	—	Cond., coated ins.	Y
STM				•	•	•		sub Å	1 Å	—	Conductors	N
SFM				•	•	•		sub Å	1 nm	—	All	N
TEM			•	•	•	•		200 nm*	5 nm	—	All; <200 nm thick	Y
EDS	•					•		1 μm	0.5 μm	500 ppm	All; $Z > 5$	Y
EELS	•	•				•		20 nm*	1 nm	Few %	All; <30 nm thick	Y
Cathodo-luminescence		•		•			•	10 nm–μm	1 μm	ppm	All; semicond. usually	Y
STEM			•	•	•	•		100 nm*	1 nm	—	All; <200 nm thick	Y
EPMA	•					•		1 μm	0.5 μm	100 ppm	All; flat best	Y
XRD			•	•	•			10 μm	mm	3%	Crystalline	N
Photo-luminescence		•		•		•	•	Few μm	Few μm	ppb	All, semicond. usually	N
Modulation Spectroscopy		•		•		•	•	1 μm	100 μm	ppm	All, semicond. usually	N
VASE							•	1 μm	cm	—	Flat thin films	N
FTIR		•		•			•	Few μm	20 μm	Variable	All	N
Raman Scattering		•		•			•	Few μm	1 μm	Variable	All	N
HREELS		•			•			2 nm	mm	1%	All; flat cond. best	Y
NMR		•	•		•			Bulk	—	—	All; not all elements	N
GDMS	•							100 nm	cm	ppt–ppb	Sample forms electrode	Y
ICPMS	•							5 μm	mm	ppt	All	Y
ICPOES	•							5 μm	mm	ppb	All	Y
Neutron Diffraction			•		•			Bulk	—	—	Crystalline	N
Neutron Reflectivity							•	Up to mm	—	—	Flat polymer films	N

Table 1: Short compilation of comparative information on the analytical techniques (this table is a quick reference guide only, cited from [107])

5. Results and discussion

5.1. Ce:LuAG, Ce:LuYAG, Ce:GdGaLuAG

5.1.1. Sample summary

Goals of presented work on Ce-doped YAG and LuAG epitaxial films were optimization of LPE growth for PbO flux, testing and reasonable improvement of scintillation properties using alternative lead-free BaO flux. Overall, we aimed on preparation of layers with qualities comparable to single crystals grown by Czochralski method.

We have grown and characterized YAG and LuAG epitaxial garnet films doped with Ce^{3+} ions. In addition, growth and characteristics of novel material of Ga and Gd codoped Ce:LuYAG were studied. Focus was on the influence of melt and its composition on sample properties. Summary of prepared samples for this study is listed in Table 2 for PbO flux grown samples and in Table 3 for BaO flux grown samples. All are divided based on used flux or their composition. For Ce content in the following tables are used values based on comparison of absorption coefficient to the reference bulk Czochralski grown Ce:LuAG single crystal. Reference single crystal Ce ions content declared by manufacturer is 0.006 p.f.u. There are also results from GDMS measurements in Table 4 and EPMA analysis in Table 5 for several of these samples.

All of LuC series are PbO flux grown. Series from 1LuC to 6LuC, 9LuC and 10LuC were grown to determine ideal and maximal Ce concentration. Melt was continuously slightly changed between samples to achieve better growth and greater Ce doping. Growth was mostly homoepitaxial, but with increasing Ce content in flux, surface quality of layers deteriorated. Series 7LuC and part of 2LuC was experiment in heteroepitaxial growth on YAG substrates. Series 8LuC was grown at higher temperatures to achieve best possible surface quality.

The LBC series were all BaO flux grown. Series from 1LBC to 7LBC were grown to determine optimal melt composition. The melt was continuously slightly changed between samples to achieve better results. Series 8LBC to 10LBC were experiment in preparation of high Ce doped layers. Flux for 11LBC and 12LBC was based on previous BaO fluxes and it was a try for series with high surface quality of films. The 13LBC series was optimized by yttrium admixture. The 14LBC was a continuation of previous series with Ga and Gd admixed. It was a starting point to further research on multicomponent garnets, which are rigorously studied in thesis of my colleague, Zuzana Onderišinová [108].

Sample	Layer thickness [μm]	Substrate	Growth temperature [℃]	Absorption at 445 nm [cm^{-1}]	x (Ce) [p.f.u.]
1LuC1	**11.5**	LuAG	986.5	71	0.004
1LuC2	**6.3**	LuAG	1004	43	0.002
1LuC3	**7.9**	LuAG	965	167	0.009
2LuC1	**8.9**	LuAG	980	143	0.008
2LuC2	**9.8**	LuAG	959.5	230	0.013
2LuC3	**9.6**	LuAG	945	304	0.017
2LuC4y	**16.0**	YAG	960	425	0.023
2LuC5y	**13.3**	YAG	980	-	-
3LuC1	**5.8**	LuAG	1010	87	0.005
3LuC2	**9.7**	LuAG	992	172	0.009
6LuC1	**26.4**	LuAG	1010.5	166	0.009
6LuC2	**2.4**	LuAG	1010.5	244	0.013
6LuC3	**6.2**	LuAG	1019	78	0.004
6LuC4	**9.6**	LuAG	1000	345	0.019
7LuC1y	**23.8**	YAG	1019	190	0.010
7LuC2y	**12.2**	YAG	1029.5	121	0.007
7LuC3y	**1.9**	YAG	1032.5	-	-
7LuC4y	**16.8**	YAG	1035.2	95	0.005
8LuC1	**17.8**	LuAG	1025.4	206	0.011
8LuC2	**16.4**	LuAG	1025.2	337	0.019
8LuC3	**8.2**	LuAG	1036	99	0.005
8LuC4	**8.1**	LuAG	1035	139	0.008
9LuC1	**24.7**	LuAG	981.5	389	0.021
9LuC2	**12.9**	LuAG	1006.3	138	0.008
10LuC1	**24.9**	LuAG	981.5	670	0.037
10LuC2	**12.7**	LuAG	1002.3	298	0.016
Ce:YAG single crystal				82	
Ce:LuAG single crystal				109	0.006

Table 2: Table of Ce:LuAG – $(Lu_{3-x}Ce_x)Al_5O_{12}$ samples grown from PbO-B_2O_3 flux (concentration of cerium is determined by comparison to the reference Czochralski grown single crystal and is given as atoms per formula unit (p.f.u.); samples, where absorption could not be measured are noted by - mark)

Sample	Layer thickness [μm]	Substrate	Growth temperature [℃]	Absorption at 445 nm [cm^{-1}]	x (Ce) [p.f.u.]
1LBC1	**-13.76**	LuAG	1020.5	-	-
1LBC2	**-6.69**	LuAG	987	-	-
1LBC3	**-4.50**	LuAG	947.5	-	-
2LBC1	**1.42**	LuAG	949	457	0.025
2LBC2	**1.25**	LuAG	934.2	615	0.034
3LBC1	**4.46**	LuAG	958.5	514	0.028
3LBC2	**10.03**	LuAG	972.8	569	0.031
4LBC1	**5.24**	LuAG	979.5	622	0.034
4LBC2	**6.78**	LuAG	1000.5	310	0.017
4LBC3	**8.12**	LuAG	1020	197	0.011
5LBC1	**4.03**	LuAG	975	≈ 462	0.015
5LBC2	**8.12**	LuAG	1000	≈ 196	0.011
6LBC1	**1.00**	LuAG	978.5	468	0.026
6LBC2	**1.98**	LuAG	964.5	335	0.018
7LBC1	**8.50**	LuAG	1000	305	0.017
7LBC2	**11.90**	LuAG	1030	218	0.012
7LBC3	**15.10**	LuAG	1060	100	0.006
8LBC1	**6.50**	LuAG	998	-	-
8LBC2	**12.30**	LuAG	1050.1	-	-
9LBC1	**7.38**	LuAG	999	-	-
9LBC2	**14.92**	LuAG	1048.6	-	-
10LBC1	**11.06**	LuAG	1049.5	-	-
11LBC1	**8.49**	LuAG	990.4	160	0.009
11LBC2	**9.76**	LuAG	1009	114	0.006
11LBC3	**7.16**	LuAG	1029.7	90	0.005
12LBC1	**12.30**	LuAG	1019.5	146	0.008
12LBC2	**3.84**	LuAG	1037.6	138	0.008
12LBC3	**5.22**	LuAG	1019.5	125	0.007
13LBC1	**16.95**	LuAG	1030.5	127.5	0.007
13LBC2	**19.70**	LuAG	1040	126	0.007
14LBC1	**10,44**	LuAG	1020,2	113	0.006
14LBC4	**15,90**	YAG	1049,7	106	0.006
14LBC5	**16,98**	YAG	1068,3	69	0.004
14LBC6	**9,3**	YAG	1039,1	-	-
14LBC7	**7,0**	YAG	1015	60	0.003
Ce:YAG monokrystal				82	
Ce:LuAG monokrystal				109	0.006

Table 3: Table of Ce:LuAG – $(Lu_{3-x}Ce_x)Al_5O_{12}$ samples grown from $BaO\text{-}B_2O_3\text{-}BaF_2$ flux (concentration of cerium is determined by comparison to the reference Czochralski grown single crystal and is given as atoms per formula unit (p.f.u.); samples, where absorption could not be measured are noted by - mark)

Ce:LuAG (PbO flux)					
	Pb x 10^3	**Ce x 10^2**	**Y x 10^2**	**Pt x 10^2**	**B x 10^2**
2LuC2	0.214	1.094	0.45	0.135	0.866
Ce:LuAG (BaO flux)					
3LBC1	0.004	1.883	0.013	0.017	1.181

Table 4: Table of GDMS content analysis data for selected few Ce:LuAG – $(Lu_{3-x}Ce_x)Al_5O_{12}$ samples from $PbO\text{-}B_2O_3$ and $BaO\text{-}B_2O_3\text{-}BaF_2$ flux, the concentrations are given as atoms per formula unit (p.f.u.)

	Al	**Ga**	**Y**	**Ce x 10^2**	**Gd**	**Lu**
14LBC1	5.06	0.02	0.44	1.30	0.12	2.35
14LBC4	3.73	1.31	0.38	1.06	0.54	2.02
14LBC5	3.73	1.31	0.37	1.03	0.61	1.98
14LBC6	3.48	1.51	0.38	0.61	0.96	1.66
14LBC7	3.68	1.48	0.42	0.74	0.96	1.45

Table 5: Table of EPMA content analysis data for Ce:GGAG – $(Lu_{3-x-y-z}Gd_xY_yCe_z)(Al_{5-u}Ga_u)O_{12}$ samples from $BaO\text{-}B_2O_3\text{-}BaF_2$ flux, the concentrations are given as atoms per formula unit (p.f.u.)

From measurements is evident a decreasing trend of Ce concentration in layers with increasing temperature. In Figure 39 in the upper graph are shown Ce concentration dependences on temperature for $PbO–B_2O_3$ fluxes and all series show the decrease as the temperature closes to saturation temperature. The lower graph shows $BaO–B_2O_3$ fluxes. The 3LBC and 6LBC series have anomalous behavior with opposing, increasing tendency. We assume, that at low growth temperature, there is a connection to viscosity problem the $BaO–B_2O_3$ flux system has in general. As mentioned above, the series up to seventh were used as a trial to optimize the growth process. The Ce concentration in the missing 8, 9 and 10LBC series was impossible to asses from absorption due to high scattering of the samples.

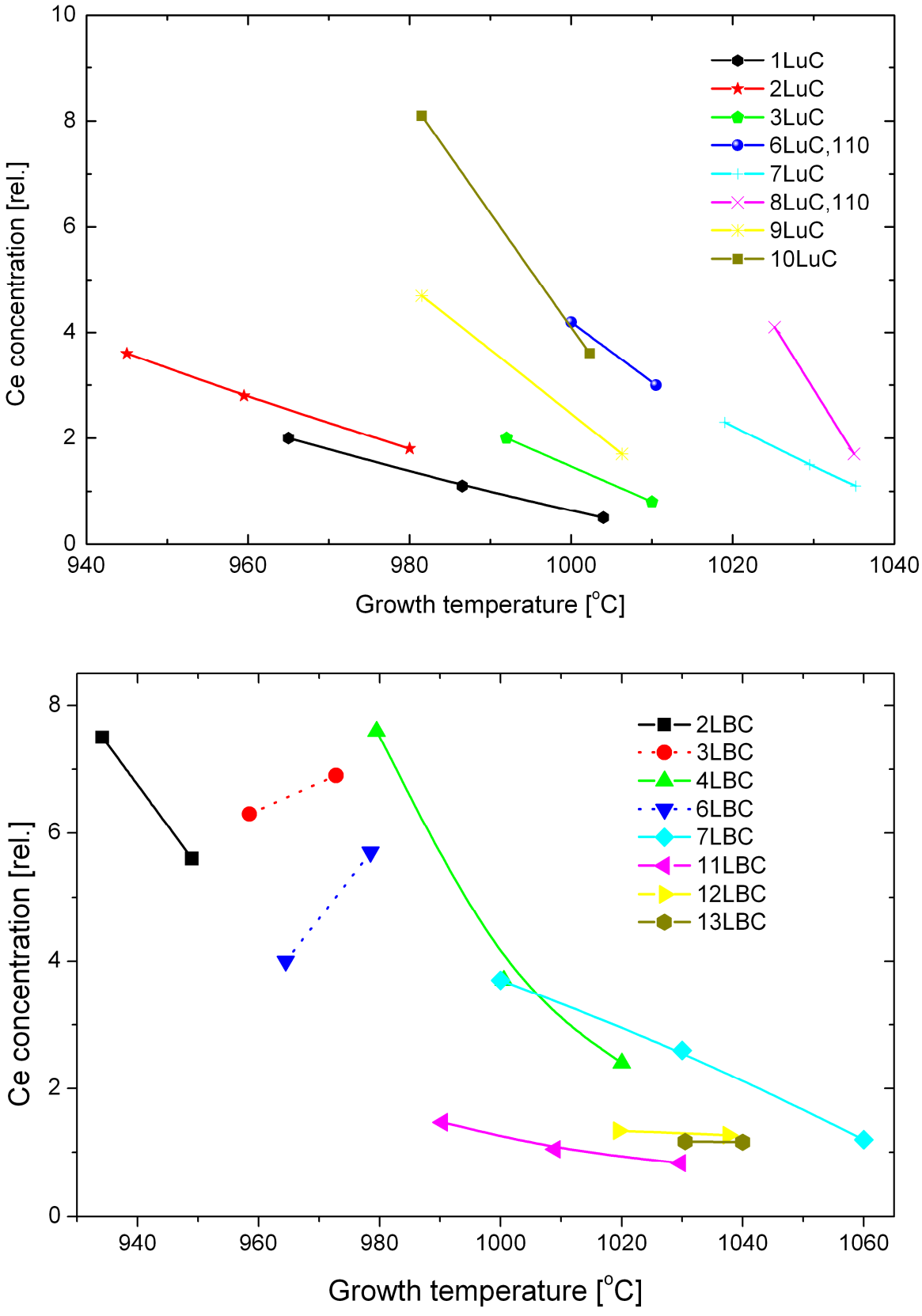

Figure 39: Concentration dependences of cerium in LuAG films on the growth temperature. The upper graph shows layers grown from $PbO–B_2O_3$ flux, the lower graph shows samples grown from $BaO–B_2O_3–BaF_2$ flux. Concentrations are relative to reference crystal. For specifics see Table 2 and Table 3 and [99].

5.1.2. Absorption

The spectra of the absorption coefficient of Ce-doped LuAG films are shown in Figure 40 for PbO – B_2O_3 flux grown samples and in Figure 41 for BaO – B_2O_3 flux grown samples. Spectrum of high purity Czochralski (CZ) grown Ce:LuAG single crystal (J. Kvapil, Monokrystaly Turnov) we used as a reference sample is plotted in both graphs for reference. Concentration of Ce was assessed from absorption coefficient ratio between sample and single crystal in peak at 448 nm for all samples. In addition, the 14LBC series was sent for EPMA analysis. The Ce content measured by EPMA was roughly twice the amount obtained by the absorption comparison method. Two broad peaks belonging to 4f - $5d_1$ and 4f - $5d_2$ centered at 448 nm and 346 nm were observed in all Ce:LuAG samples. The higher energy transitions in Ce^{3+} either are behind cut off (for PbO grown samples) or are not very well resolved (for BaO grown samples). A broad band around 225 nm could be distinguished only in CZ single crystal. The same band in epitaxial layers is modulated by absorption of impurities or lost in distortion caused by scattering.

A strong absorption below 270 nm is always present in films grown from the PbO flux. The Pb^{2+} ions are responsible. The relative concentration of lead ions is rather high for samples with high supercooling of the melt during growth. Transmission of optically transparent films, grown from the BaO flux, reaches further into the UV region. Observed content of impurities and Ce^{3+} ions is higher in heteroepitaxial films (2LuC4y and 2LuC5y and from 7LuC1y to 7LuC4y) compared to homoepitaxial ones grown under the same conditions.

The absorption peak of Ce at 448 nm in Ce:LuAG slightly shifts to longer wavelengths with admixed yttrium as it can be seen in 13LBC series. Furthermore, both Ce peaks are shifted closer together with introduction of Ga and the peak at 448 nm shifts to shorter wavelengths in 14LBC series. Specifically, the 14LBC4 shown in Figure 41 has maximum at 439 nm. This is in agreement with literature, where multicomponent Ce:GaGdYAG [17, 56, 57, 59] and Ce:GaGdLuAG [56] is studied. There is also noticeable Gd contribution with peaks at 275, 308 and 314 nm.

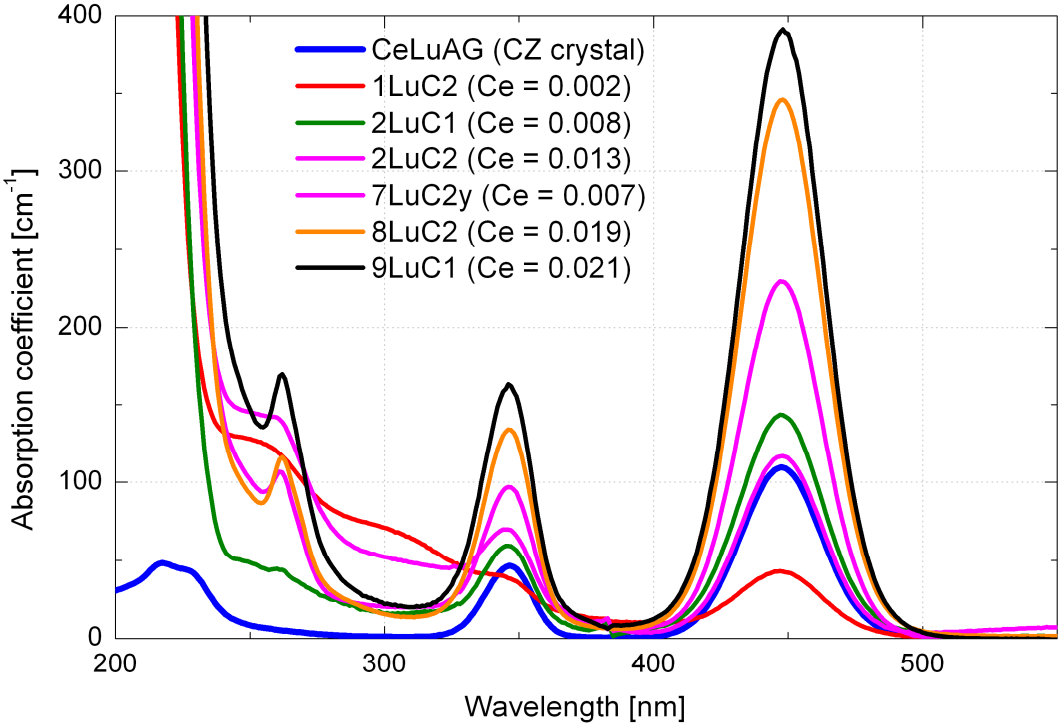

Figure 40: Absorption coefficient spectra for the PbO–B_2O_3 flux grown samples. Concentration of Ce relative to Ce:LuAG reference CZ grown single crystal are noted in the legend in p.f.u. For comparison added spectra of reference Ce:LuAG single crystal (Blue line).

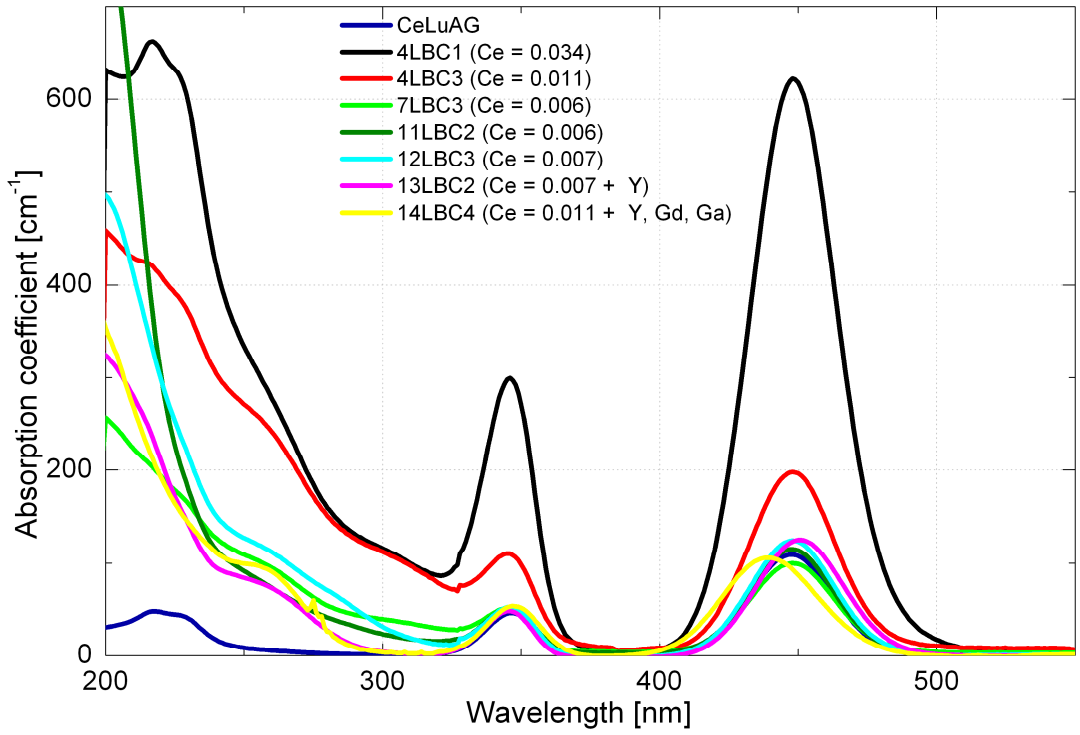

Figure 41: Absorption coefficient spectra for the BaO–B_2O_3 flux grown samples. Concentrations of Ce relative to Ce:LuAG reference CZ grown single crystal are noted in the legend in p.f.u. (for 14LBC4 is used GDMS analysis value); Spectra of reference Ce:LuAG single crystal added for comparison (black line).

5.1.3. Photoluminescence

The excitation and emission spectra were measured in the spectral range from 200 nm to 850 nm. An example of PL excitation spectra of Ce^{3+} emission at wavelength λ_{em} = 530 nm is shown in Figure 42. The shape of the excitation spectra shows a close resemblance to the absorption coefficient curves shown in Figure 40 and in Figure 41. Despite heavy absorption in the UV range for both PbO and BaO flux grown samples (clearly visible superior absorption of CZ grown single crystal below 320 nm in Figure 40), the Ce^{3+} contribution in the PL excitation spectra in the range from 270 nm to 220 nm is evident. Yttrium substitution in 13LBC shifted the highest peak at 446 nm to 449 nm. In the multicomponent (Y, Ga and Gd) garnets of 14LBC series, this peak shifts to 436 nm. There is also noticeable Gd contribution with peaks at 273, 306 and 312 nm.

An example of PL emission spectra in one of the two 4f - 5d transitions of Ce^{3+} with peak at excitation wavelength λ_{exc} = 445 nm is displayed in Figure 42. The observed broad emission band has a maximum, based on composition, in the range from 510 nm to 550 nm. For the pure Ce:LuAG samples from PbO flux, the peaks were between 510 and 520 nm. The BaO grown samples emission have characteristic broad plateau. The widest plateau is spread from 510 nm and reaching up to 550 nm. The excitation of samples with yttrium substitution in 13LBC series looks like in the PbO grown and the peaks were between 510 and 520 nm. In layers with Y, Ga and Gd substitution (14LBC), a wide peak with maximum at 525 nm occurred.

The Pb^{2+} ions originating from PbO flux compete with the Ce^{3+} ions for charge [26]. The Pb^{2+} was identified as a trap center for emission at 345 nm. It can be seen from ratio between 345 nm and 445 nm peaks in excitation spectra (shown in Figure 42) of samples 2LuC3 and 4LBC2, that in heavily Pb polluted 2LuC3 (very low growth temperature), the 445 nm peak is dominant and roughly double in size. In the 4LBC2, the 345 nm peak represents approximately 80 % of the 445 nm peak.

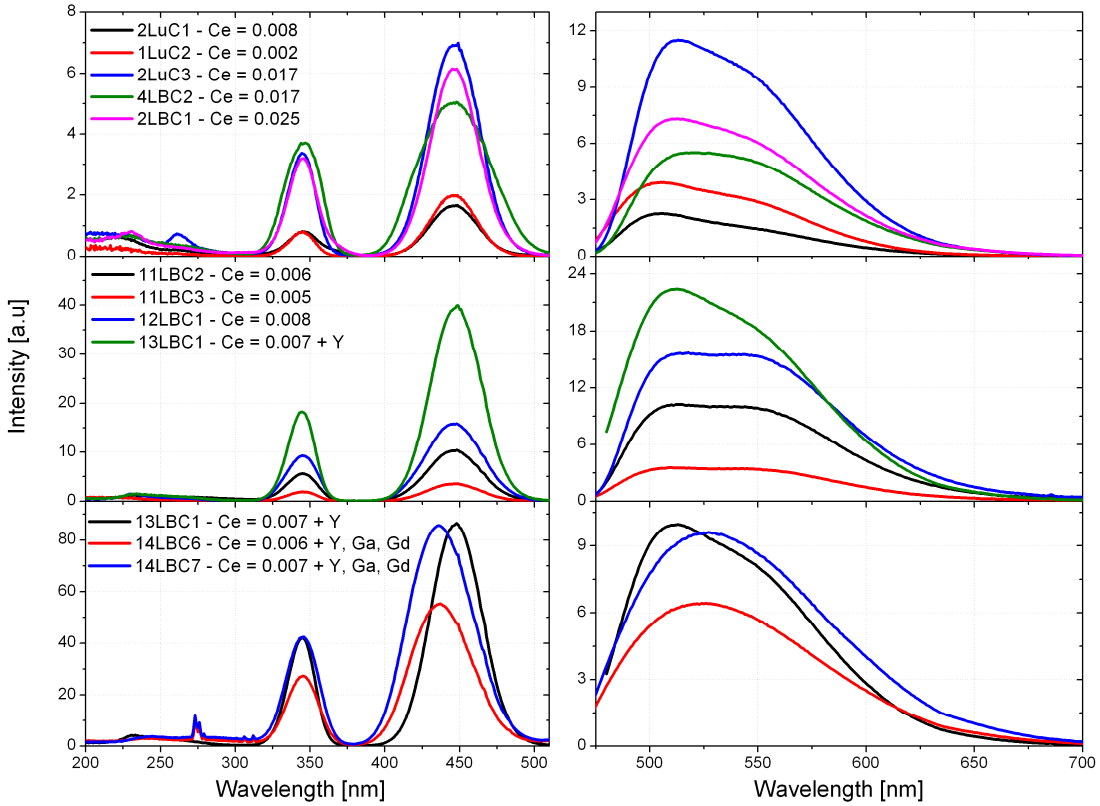

Figure 42: Left side shows excitation (at λ_{em} = 530 nm) and right side emission (at λ_{exc} = 445 nm) spectra of Ce:LuAG epitaxial layers grown from either PbO (LuC) or BaO (LBC) based fluxes. Left and right graphs contain corresponding samples.

5.1.4. Decay kinetics

The decay curves for Ce-doped LuAG films grown from both the PbO and BaO fluxes are shown in Figure 44 and Figure 43. The samples were excited at Ce^{3+} absorption peak at 340 nm and the PL emission was collected at 520 nm in all graphs in Figure 44 and at Gd^{3+} absorption at 274 nm and the PL emission was collected at 312 nm in Figure 43.

A two-exponential decay can be seen from fitted decay curves in Ce:LuAG samples grown from the PbO based flux (in Figure 44, b). The main component has decay time approximately 35 ns. This is far from 54 ns observed in the CZ single crystal [37]. The second, weaker, component has decay time 62 ns. The two-exponential decay indicates involvement of a nonradiative transfer. Part of the excitation energy is transferred between Ce^{3+} and impurity ions or defects. The amount of energy loss involving the nonradiative transitions can be roughly estimated by integration of decay curves and comparing those integral with single crystal. This approach shows approximately 3 % energy loss in PbO flux grown films. Identification of defect responsible for this energy dissipation will need further

investigation. Research on this topic can be found in [39-41]. The emission at about 580 nm was connected to Pb-based centers there. Based on this knowledge, we can assume an overlap of the excitation band with Ce^{3+} emission band and subsequent energy transfer from Ce^{3+}. No second component aside the main decay time is observed in high quality single crystals. The decay curve of a typical Ce:LuAG film grown from the BaO flux is shown in Figure 44, a. There are no Pb ions in these layers. The decay data in semilogarithmic representation show linear dependence over three orders of magnitude. This indicates one-exponential decay. The decay time from fitted curve is approximately 56 ns and corresponds very well with decay time of CZ single crystal mentioned above. This indicates lossless emission.

The decay times of Ce^{3+} in Ce:LuYAG samples, also grown from BaO flux, were one-exponential too and did not differ much as shown in Figure 44, c, as well as in Ce:GaGdLuYAG layers in Figure 44, d. The spread of decay times was within 8 % from 56 ns. There is a noticeable increase of background signal in multicomponent Ce:GaGdLuYAG layers. This is most probably caused by delayed emission caused by Gd - Ce energy transfer. The Gd ions have extremely long decay times, when compared to Ce ions. This topic is rigorously studied in thesis of my colleague, Zuzana Onderišinová [108, 109].

Typical graph of Gd ions decay time in multicomponent Ce:GaGdLuYAG layers are shown in Figure 43. There is a sharp peak at the beginning, because at 274 nm, the Ce ions are also excited. Shown sample has decay time of Gd ions 6.5 ms and when Ce contribution is excluded, it is one-exponential decay. The Ce ions excited at 274 nm show two-exponential decay times at high Gd concentrations. One component is fast, close to Ce excited at 340 nm and one long, close to Gd ions.

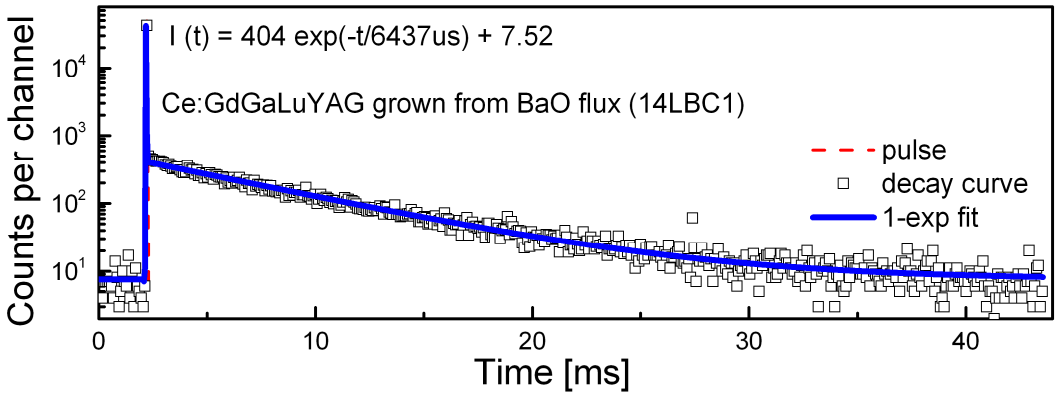

Figure 43: Decay kinetics spectra for Gd ion in epitaxial layers grown from BaO based flux (samples excited at 274 nm, emission collected at 312 nm; data fitted by reconvolution with apparatus function - red pulse)

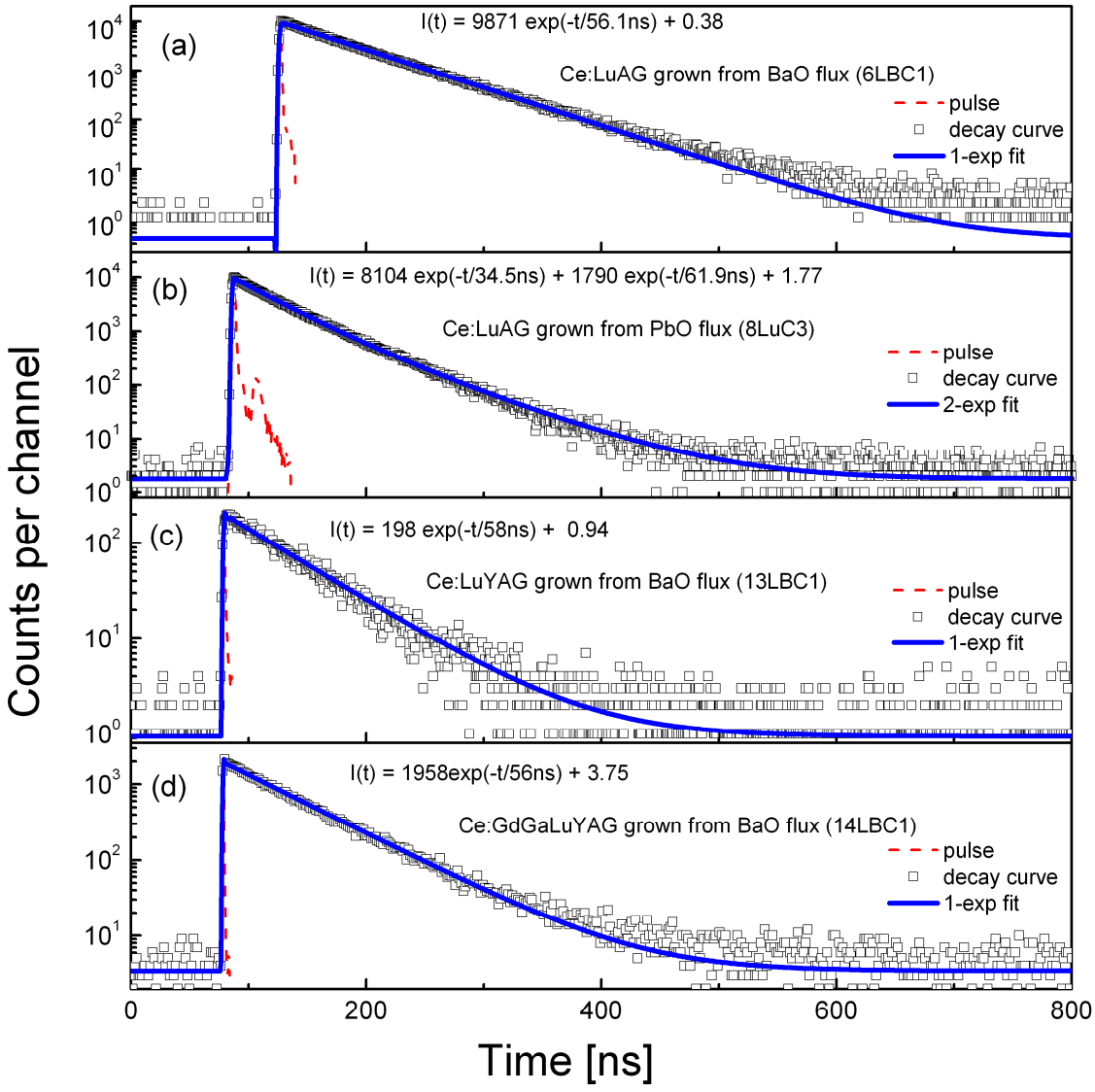

Figure 44: Decay kinetics spectra for Ce ion in epitaxial layers grown either from PbO (b - 8LuC3) or BaO (others, a,c,d) based fluxes (samples excited at 340 nm, emission collected at 530 nm; data fitted by reconvolution with apparatus function - measured response function for each spectra - red pulse) also shown in [110, 111]

5.1.5. Radioluminescence

The RL spectra were measured with the X-ray excitation source voltage set to 10 kV and current to 50 mA. The emitted light was measured in the spectral range from 200 nm to 670 nm. Spectra were compared with reference BGO single crystal ($Bi_4Ge_3O_{12}$). This provided objective mutual comparison of samples. An example of the RL spectra of Ce doped LuAG and LuYAG layers is displayed in Figure 45 a. The multicomponent Ce:GdGaLuYAG samples are shown in Figure 45 b.

There are two clearly distinguished emission bands in both LuYAG and multicomponent samples. The broad emission band located in the UV region between 250 and 400 nm with a maximum near 300 nm appears in majority of layers. It was not observed in PL spectra. This band originates mainly from the host lattice defects, since the host lattice was not excited in the PL. It most probably comes from antisite defects Lu_{Al} as reported in [6, 112]. It also has a contribution from the substrate, because the excitation X-rays penetrate tens of μm deep. There is also a possibility of some unidentified impurities. In the multicomponent layers is this band modulated by peak with maximum at 314 nm, which originates from the 4f - 4f transitions of Gd^{3+}.

Broad emission band of Ce^{3+} 5d transition have maxima at 510 nm and resembles the PL emission spectra for λ_{exc} = 445 nm shown in Figure 42. The ratio between both bands (300 nm and 510 nm) is slightly shifted in favor of the 510 nm one as Ce concentration rises and layers thickness increases in both Ce:LuYAG and Ce:GdGaLuYAG. The peak wavelengths slightly shift because of different Yttrium content in the 13LBC series and Ga/Gd codoping in the 14LBC series. For sample with the most Yttrium, with approx. 0.52 p.f.u. of Yttrium, 13LBC2, the peak maxima shifted to 320 nm and 515 nm respectively. The Ce peak in the multicomponent samples was 517 nm for light doping of Ga (0.02 p.f.u.) and Gd (0.12 p.f.u.). It shifted to 525 nm in heavily doped samples (14LBC6,7; Ga concentration 1.5 p.f.u. and Gd 0.96). The sharp Gd peak at 312 nm is most intensive at low Gd doping and it quenches with increased concentration. In samples with highest Gd content is completely quenched. The Gd^{3+} ions are reported [8] to be effective donors for a number of rare earth ions. From this and from graphs (in Figure 45 b), we can deduce, that an energy transfer from Gd to Ce ions occurs (discussed in greater detail in [108, 111]). In the graph is clearly visible steep decrease of Gd peak at 314 nm with increasing Gd concentration between samples 14LBC1 and 4, which is in contrast to Ce emission increase. This is a sign of positive role of Gd and Ga doping on the light output. Further increase in Gd concentration is detrimental to the growth process. Overall intensity decrease seen at samples 14LBC6 and 7 is due to significantly thinner layers. This decrease prevents precise assessment of high Gd and Ga doping impact on RL. The overall integral RL intensity of the samples spectra is significantly higher compared to that of BGO reference single crystal.

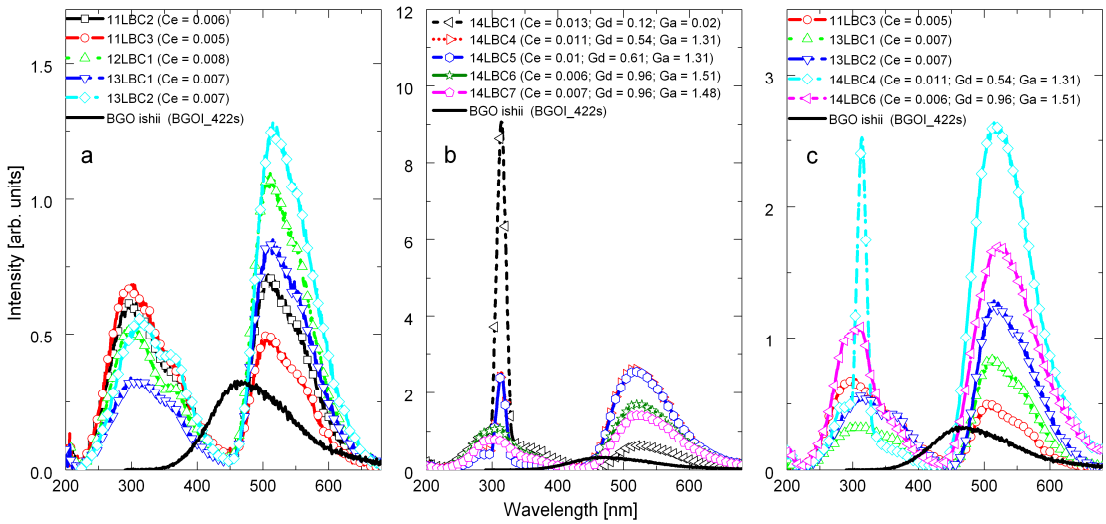

Figure 45: Radioluminescence spectra of Ce:LuAG (a) and Ce:GGAG (b) samples and their comparison (c); Concentrations noted in the legend are in p.f.u.; concentrations in Ce:GGAG are based on EPMA analysis. All shown spectra are in correlation to the plotted reference spectra of BGO crystal

5.1.6. Scintillation properties

Photoelectron yield of Ce:LuAG epitaxial layers were studied under alpha particle excitation (using ^{239}Pu alpha particle source, with particle energy 5.16 MeV). Photoelectron yield measurements of Ce:LuAG and Ce:LuYAG samples are shown in Figure 46. The results are in correlation with RL spectra. Yttrium has positive effect on photoelectron yield. The 13LBC2 sample with 0.52 p.f.u. of yttrium admixed shows highest photoelectron yield. The dynamic response represented by normalized photoelectron yield (see Figure 46 b) is on par with the other yttrium-doped samples and other low Ce doped samples. The relative N_{phe} increase is 45 %. This is better than highly doped Ce:LuAG sample with much higher relative N_{phe} increase, 65 %. The best dynamic response has low-doped Ce:LuAG sample (11LBC3) with lowest relative N_{phe} increase, 25 %. It has very little slow components. It was observed that high Ce concentration does not significantly quench luminescence as other rare earth ions do, but it is of no benefit either [113]. Photoelectron yield of multicomponent Ce:GdGaLuYAG epitaxial layers are shown in Figure 47. Contribution from the Gd^{3+} centers does not show directly in photoelectron yield measurements due to its millisecond decay time. Gd has strong emission that partially quenches Ce emission, especially at low Gd concentration (14LBC1). With higher Gd concentration is its emission quenched and Ce emission significantly increases due to energy transfer from Gd to Ce ions (14LBC4,5). Comparison to best Ce:LuYAG sample (13LBC2) show potentially greater light

yields. Best sample 14LBC4 looks promising as it has highest photoelectron yield, approx. 20 % higher than 13LBC2 and apparently less slow components longer than 6 μs (nearly flat after 6 μs). Extrapolation of Gd and Ga substitution expect further increase of photoelectron yield and suppression of slow components [114].

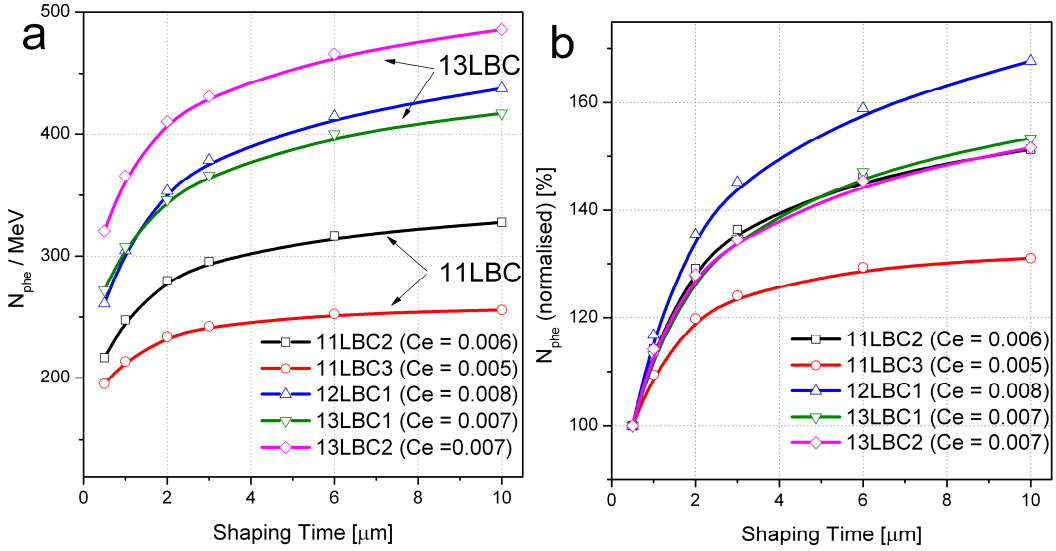

Figure 46: a - Photoelectron yield N_{phe} per MeV as function of shaping time under alpha particle excitation (source ^{239}Pu) of Ce:LuYAG epitaxial layers (concentrations of Ce relative to Ce:LuAG reference CZ grown single crystal are noted in the legend in p.f.u.); b - Normalized photoelectron yield to the shortest shaping time of 0.5 ms for the same samples.

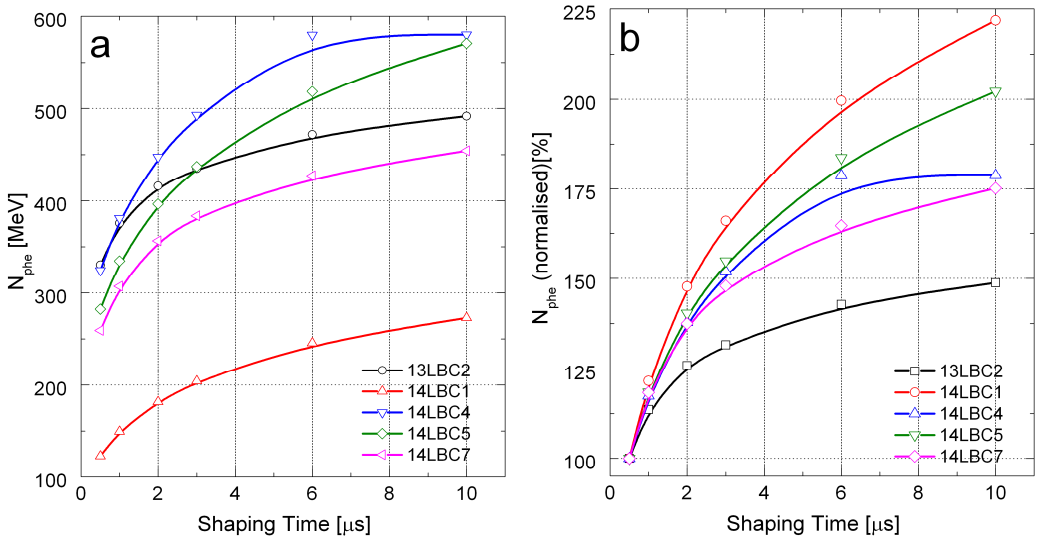

Figure 47: a - Photoelectron yield N_{phe} per MeV as function of shaping time under alpha particle excitation (source ^{239}Pu) of Ce:GdGaLuYAG epitaxial layers; b - Normalized photoelectron yield to the shortest shaping time of 0.5 ms for the same samples.

5.1.7. Summary

In this chapter, the growth process for both PbO – B_2O_3 and BaO - B_2O_3 - BaF_2 flux was optimized and samples with good optical quality were prepared from PbO based flux. The content of ever-present Pb^{2+} impurity from lead fluxes was reduced at high growth temperatures and low supercooling. Achieved improvements of alternative barium flux allowed successful growth of samples with high Ce concentrations, without luminescence quenching impurities and with surface quality on par with PbO – B_2O_3 flux.

Basic characteristics of the Ce:LuAG, Ce:LuYAG and Ce:GaGdLuYAG epitaxial films were studied by measuring of absorption spectra, photoluminescence, radioluminescence, decay kinetics and photoelectron yield. Optimization of Ce:LuAG lattice by Y admixing showed promising results but Gd and Ga admixture in multicomponent Ce:GdGaLuYAG garnet suggests significant improvement of scintillation properties. A red shift caused by Y doping and also blue shift due to the Ga doping was observed. The Gd induced red shift [58] was not seen because of stronger influence of Ga. Gd influence was visible in multicomponent garnets PL excitation spectra of Ce^{3+} ion.

A nonradiative energy transfer from Gd^{3+} to Ce^{3+} ions in multicomponent garnets was observed. The proof of it can be seen in decay kinetics and RL measurements. The photoelectron yield of multicomponent garnets proved to be superior in magnitude to the plain Ce:LuAG and to Y codoped Ce:LuYAG.

5.2. Pr:LuAG

5.2.1. Sample summary

The Pr^{3+}-doped LuAG is known for fast (~ 20 ns) 5d – 4f emission and good light yield. Goals were optimization of LPE growth from BaO flux for Pr:LuAG, testing and subsequent improvement of surface, optical and scintillation properties. We aimed on preparation of samples qualitatively comparable to single crystals grown by Czochralski method. Improvement of scintillation properties was expected with Sc codoping. Energy transfer from Sc to Pr was anticipated based on structure of energy levels. The idea of consecutive energy transfer from Sc to Pr to Ce [58, 115] was based on the same assumption. All this was meant to increase the light yield.

Summary of prepared samples for this study is listed below in Table 6 and Table 7. All are prepared from $BaO\text{-}B_2O_3\text{-}BaF_2$ flux. For dopant content in the following tables are used either values based on melt composition and estimated from segregation coefficient or results from EPMA and GDMS measurements for chosen samples. Main focus was the influence of Sc content varying from low to high on low-doped Pr:LuAG in series from 1LBS to 3LBS and at the beginning of series 5 and 6LBS. The 4LBS samples were grown to discern Sc contribution in luminescence. Series 7LBS and 8LBS were prepared to discern Pr contribution. A possibility of Ce codoping was also studied in last few samples of 5LBS, 6LBS and 8LBS series.

Sample	Layer thickness [μm]	Substrate	y (Sc) [p.f.u.]	x (Pr) [p.f.u.]	Calculated lattice constant	Measured lattice constant
1LBS1	14.0	LuAG	0.005	0	11.916	11.918
1LBS2	12.1	LuAG	0.005	0.0009	11.917	-
1LBS3	11.6	LuAG	0.005	0.0018	11.918	11.918
1LBS4	12.1	LuAG	0.031	0.0018	11.922	11.917
1LBS5	8.2	LuAG	0.122	0.0018	11.939	11.936
1LBS6	5.4	LuAG	0.122	0.0018	11.939	11.943
1LBS7	5.5	YAG	0.360	0.0018	11.98	11.979
1LBS8	6.9	YAG	0.792	0.0018	12.054	12.047
1LBS10	5.0	CGGG	1.996	0.0018	12.262	12.154
2LBS2	10.5	YAG	0.55	0.0005	12.012	-
2LBS3	12.0	YAG	0.57	0.0017	12.017	-
2LBS4	10.4	YAG	0.56	0.0041	12.022	-
3LBS2	6.3	LuAG	0.12	0.0002	-	-
3LBS3	8.5	LuAG	0.12	0.0005	-	-
3LBS4	11.7	LuAG	0.12	0.0009	-	-
3LBS5	9.9	LuAG	0.12	0.0012	-	-
3LBS6	11.2	LuAG	0.12	0.0016	-	-
4LBS2	5.7	LuAG	0.027	0	11.921	11.911
4LBS3	7.8	LuAG	0.1	0	11.934	11.923
4LBS4	9.1	LuAG	0.22	0	11.954	11.954
4LBS5	7.0	LuAG	0.365	0	11.98	11.987
4LBS6	6.7	YAG	0.525	0	12.006	11.983

Table 6: Table of PrSc:LuAG – $(Lu_{3-x}Pr_x)(Al_{5-y}Sc_y)O_{12}$ samples from $BaO\text{-}B_2O_3\text{-}BaF_2$ flux, only Sc and Pr variations (at samples, where lattice constant was not measured or calculated is noted by - mark, concentration of scandium and praseodymium were determined from melt content suggesting segregation coefficient k and is given as atoms per formula unit (p.f.u.); For k_{Pr} it was ~ 0.055 and k_{Sc} ~ 1)

Sample	Layer thickness [μm]	Substrate	z (Sc) [p.f.u.]	y (Pr) [p.f.u.]	x (Ce) [p.f.u.]	Calculated lattice constant	Measured lattice constant
5LBS1	10.5	YAG	0.575	-	-	-	-
5LBS2	11.8	YAG	0.575	0.0003	-	-	-
5LBS3	11	YAG	0.575	0.0006	-	-	-
5LBS4	12.3	YAG	0.575	0.0010	-	-	-
5LBS5	11.9	YAG	0.575	0.0010	0.0007	-	-
5LBS6	10.9	YAG	0.575	0.0010	0.0015	-	-
5LBS7	10.2	YAG	0.575	0.0010	0.0029	-	-
6LBS1	7	LuAG	0.24	0	-	-	-
6LBS2	11.2	LuAG	0.24	0.0003	-	-	-
6LBS3	9.9	LuAG	0.24	0.0006	-	-	-
6LBS4	10.7	LuAG	0.24	0.0010	-	-	-
6LBS5	10.5	LuAG	0.24	0.0010	0.0004	-	-
6LBS6	10.8	LuAG	0.24	0.0010	0.0009	-	-
7LBS1	19.3	LuAG	0	0.0003	-	-	-
7LBS2	14	LuAG	0	0.0007	-	-	-
7LBS3	13.6	LuAG	0	0.0017	-	-	-
7LBS4	14.9	LuAG	0	0.0048	-	-	-
8LBS1	12.7	LuAG	0	0.0045	-	-	-
8LBS2	12.4	LuAG	0	0.0043	-	-	-
8LBS3	19.9	LuAG	0	0.0041	-	-	-
8LBS4	35.7	LuAG	0	0.0041	-	-	-
8LBS5	22.1	LuAG	0	0.0077	-	-	-
8LBS6	21.4	LuAG	0	0.0077	0.0060	-	-
8LBS7	27.4	LuAG	0	0.0111	0.0059	-	-
8LBS8	18.7	LuAG	0	0.0111	0.0059	-	-

Table 7: Table of PrSc:LuAG and PrScCe:LuAG – $(Lu_{3-x-y}Ce_xPr_y)(Al_{5-z}Sc_z)O_{12}$ samples from BaO-B_2O_3-BaF_2 flux (at samples, where lattice constant was not measured or calculated is noted by - mark, concentration of scandium and praseodymium were determined from melt content suggesting segregation coefficient k and is given as atoms per formula unit (p.f.u.); For k_{Pr} it was ~ 0.055 and k_{Sc} ~ 1)

	Pr x 10^2	Sc
1LBS4	0.29	0.04
1LBS7	0.06	0.49
1LBS8	0.12	0.90
4LBS6	0	0.61

Table 8: Table of GDMS analysis data for selected few TbSc:LuAG – $(Lu_{3-x-y}Ce_xPr_y)(Al_{5-z}Sc_z)O_{12}$ samples from BaO-B_2O_3-BaF_2 flux, the concentrations are given as atoms per formula unit (p.f.u.)

	Ce x 10^2	Pr x 10^2	Sc x 10^2	Pt x 10^2	B x 10^2
1LBS3	0.00	0.10	0.26	0.04	2.12
1LBS4	0.01	0.18	2.37	0	3.74
3LBS6	0.00	0.13	9.06	0.07	10.98

Table 9: Table of GDMS analysis data for selected few TbSc:LuAG – $(Lu_{3-x-y}Ce_xPr_y)(Al_{5-z}Sc_z)O_{12}$ samples from BaO-B_2O_3-BaF_2 flux, the concentrations are given as atoms per formula unit (p.f.u.)

Sample	Lu	Y x 10	Pr x 10^2	Ce x 10^2	Al	Sc x 10	O
1LBS1	2.53	0	0	0	5.46	0.09	11.989
1LBS2	2.52	0	0.15	0	5.47	0.10	11.978
1LBS3	2.54	0	0.15	0	5.45	0.07	11.991
1LBS4	2.54	0	0.08	0	5.42	0.42	11.935
1LBS5	2.54	0	0.18	0	5.26	1.97	11.994
1LBS6	2.55	0	0.10	0	5.22	2.24	11.995
1LBS7	2.53	0	0.14	0	4.93	5.39	11.996
1LBS8	2.42	0	0.12	0	4.63	9.50	12.000
1LBS10	2.40	0	0.43	0	3.88	17.23	11.994
2LBS4	2.64	0	0.72	0	4.66	6.95	12.002
3LBS6	2.80	0	0.13	0	5.11	0.94	12.001
4LBS6	2.66	0	0	0	4.71	6.32	11.999
6LBS6	2.79	0	0.05	0	5.00	2.08	12.010
7LBS1	2.92	0	0.39	0	5.07	0	11.992
7LBS2	2.91	0	0.30	0	5.09	0	11.994
7LBS3	2.92	0	0.20	0	5.08	0	11.992
7LBS4	2.90	0	0.81	0	5.09	0	11.984
8LBS2	2.68	3.35	0.24	0	4.98	0	11.996
8LBS3	2.40	6.85	0.26	0	4.91	0	11.993
8LBS1	2.77	0.81	0.60	0	5.15	0	11.987
8LBS5	2.40	4.52	1.15	0	5.14	0	11.983
8LBS6	2.42	4.57	1.21	1.36	5.10	0	11.963
8LBS7	2.44	4.48	1.19	0.99	5.09	0	11.966
8LBS8	2.43	4.56	1.54	1.35	5.08	0	11.954

Table 10: Table of EPMA analysis data for selected PrSc:LuAG – $(Lu_{3-x-y-z}Y_xCe_yPr_z)(Al_{5-u}Sc_u)O_{12}$ samples from $BaO\text{-}B_2O_3\text{-}BaF_2$ flux, the concentrations are given as atoms per formula unit (p.f.u.); (overall sum of cations normalized to 8, oxygen calculated as remainder, inherent problem of separating Lu and Al peaks in the measurement resulted in the overestimation of Al content and underestimation of Lu content in many samples)

5.2.2. Absorption

Optical density calculated from measured absorption of PrSc:LuAG and CePrSc:LuAG layers for two selected Sc doping levels (0.12 and 0.575 p.f.u.) and varying Pr and Ce content from 0 to 0.0029 p.f.u. is shown in Figure 48 and in Figure 49 respectively. Optical quality of all epitaxial layers (grown from the BaO flux) is mostly high (defect density range from few pits per sample up to pit aggregates, for reference see Figure 33). No impurity related absorption was observed at all. The broad and intense absorption bands at 240 nm and 282 nm originate from parity allowed 4f - 5d transitions of Pr^{3+}. The two lowest levels of 5d (^2D) states are splitted by crystal field. The parity forbidden f – f transitions of Pr^{3+} ions were not visible in the absorption spectra, due to low doping concentrations and low thickness of the layers. At 345 and 445 nm were observed allowed 4f - 5d transitions originating from

Ce^{3+} ions. Doping with Sc^{3+} ions does not introduce any peak in the absorption spectra and has no visible effect on the absorption spectra. Increased absorption below 230 nm most probably comes from the decrease of the band gap of LuAG caused by Sc content or as a result of increased scattering causing greater error in computation of optical density.

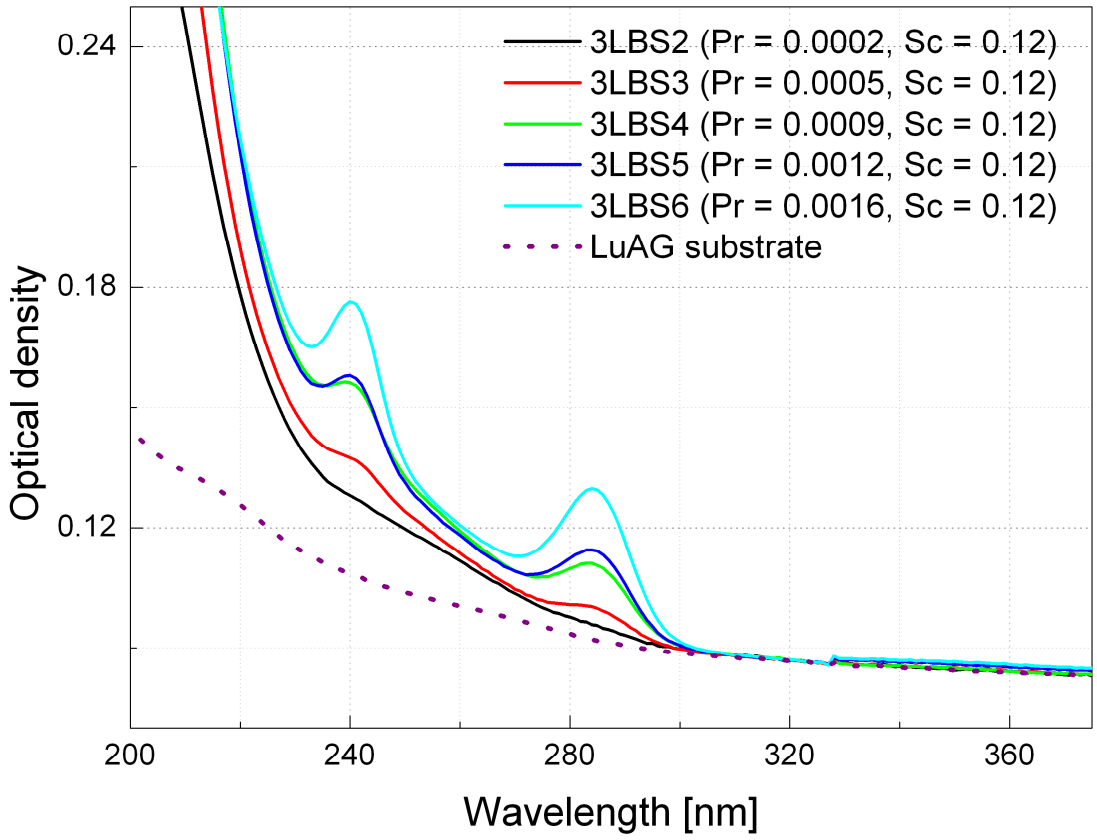

Figure 48: Optical density of Sc and Pr co-doped LuAG epitaxial layers (with constant 0.12 p.f.u. of Sc and increasing Pr concentration from 0.0002 to 0.0016 p.f.u., grown on LuAG substrates from the $BaO–B_2O_3–BaF_2$ flux, LuAG substrate shown for reference) (see also in [116])

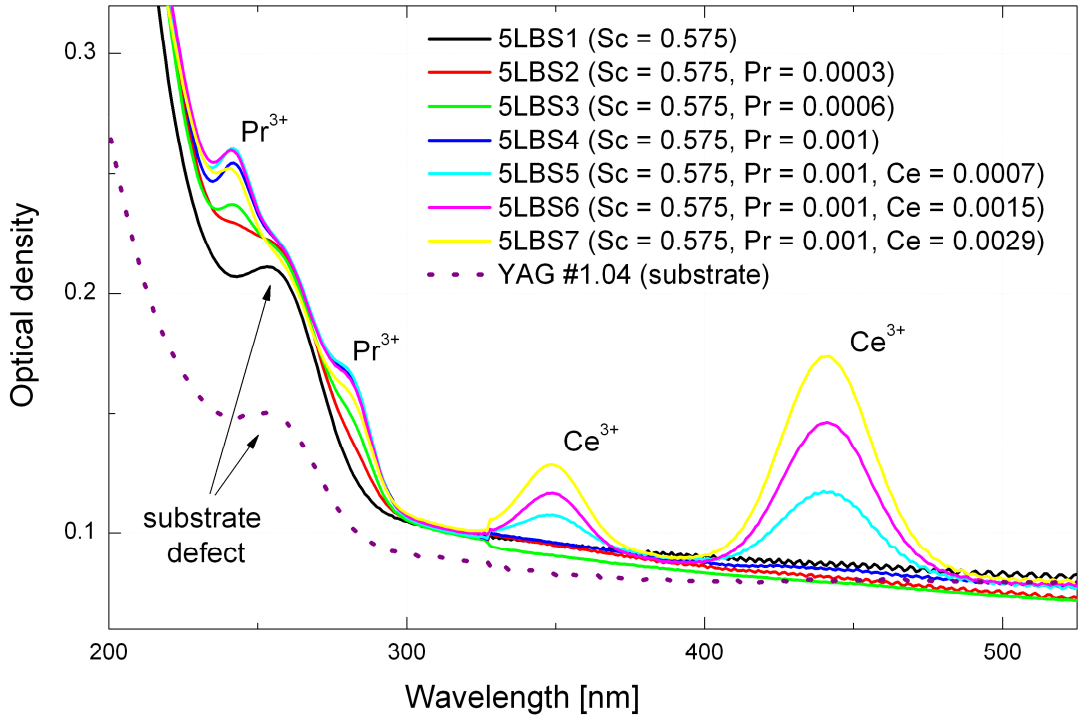

Figure 49: Optical density of Sc and Pr co-doped LuAG epitaxial layers (ScPrCe:LuAG layers with 0.575 p.f.u. of Sc grown on YAG substrates, samples doped with Ce exhibit maxima at 345 and 445 nm. The absorption band at 260 nm comes from the defects in the YAG substrates, which is shown in YAG substrate reference, all samples grown from the $BaO–B_2O_3–BaF_2$ flux) (see also in [116])

5.2.3. Photoluminescence

The spectral range of excitation and emission spectra measurements of the PL was from 200 to 850 nm. Example graphs are shown in Figure 50. The PL was excited at 282 nm in 4f – 5d absorption band below the band gap of the LuAG material. The samples doped only with Pr^{3+} ions show intense UV PL between 290 and 450 nm. Transitions from 5d states to 4f (^3H_J, ^3F_J) manifolds (the example spectra is in Figure 50, graph a, b and c) are responsible for these PL bands. The maximum of this emission is at 308 nm and its position was independent on Sc concentration (see Figure 50, graph b and c). Very weak and narrow intraconfigurational 4f – 4f transitions of Pr^{3+} from ^3P and ^1D terms to ^3H_J ground states were observed near 480 and 615 nm. Nearly all of the emission in the Pr:LuAG is in the UV. The integral intensity of 5d - 4f transitions spectral band

dominates over f - f transition peaks with more than 96 % from whole integral. The broad bands in the excitation spectra belonging to Pr^{3+} 5d transitions at 240 and 282 nm match those seen in the absorption spectra (Figure 48). All PL properties of Pr:LuAG epitaxial layers are nearly similar to single crystals mentioned in [117].

The PL spectra of ScPr and ScPrCe:LuAG samples are shown in Figure 50, graph b and c. Any Sc related emission did not appear in the measured PL spectra. There is a significant increase in PL intensities of forbidden f - f transitions for both 480 and 615 nm at higher Sc doping concentrations. This is accompanied by the decrease in intensity of allowed 5d - 4f emission. Figure 51 shows the ratio of integral intensity of PL emission from f - f transitions to the d - f integral intensity. Linear dependence on Sc concentration is obvious up to the highest Sc content, where this ratio is an order of magnitude higher than in samples without Sc. Nearly one third of the emission comes from the forbidden f - f transitions in the sample with highest Sc concentration. The process of the energy transfer is not clear. It can be explained by a nonradiative transition from 5d states to lower 4f states of Pr^{3+}.

The PL intensity of Pr^{3+} ions decrease with Ce^{3+} doping (for example see Figure 50, graph c). The Ce emission is significantly lower compared to the sample from previous chapter with equivalent Ce content and nearly same thickness (5LBS6 ~ 1LuC1). In addition, quenching of 5d emission of Pr^{3+} ions is evidently due to Ce doping.

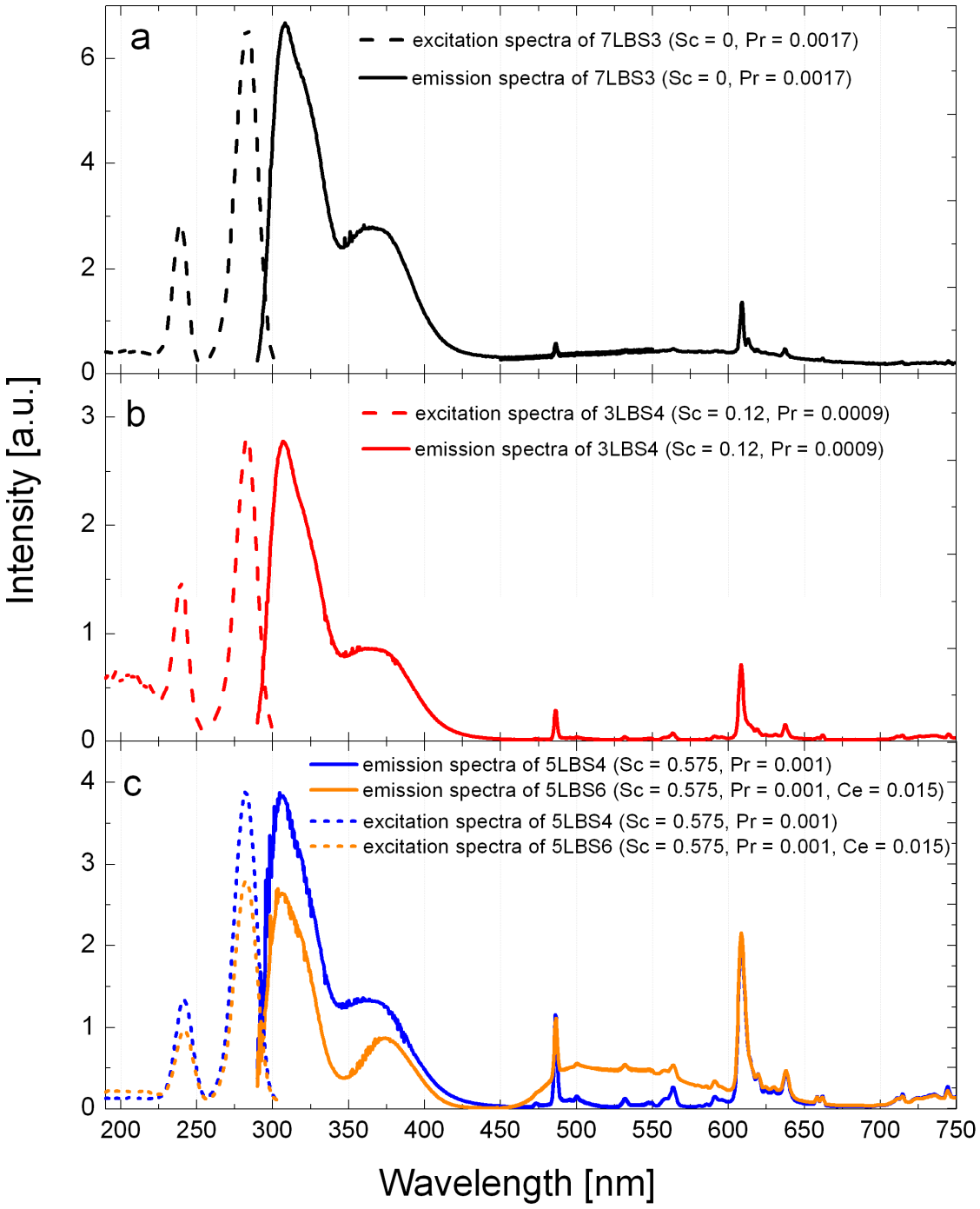

Figure 50: PL excitation spectra (emission at 310 nm) and emission spectra (excited at 282 nm) of ScPrCe co-doped LuAG samples. Concentrations of dopants in shown layers are noted in legends in p.f.u. (for further details see [116])

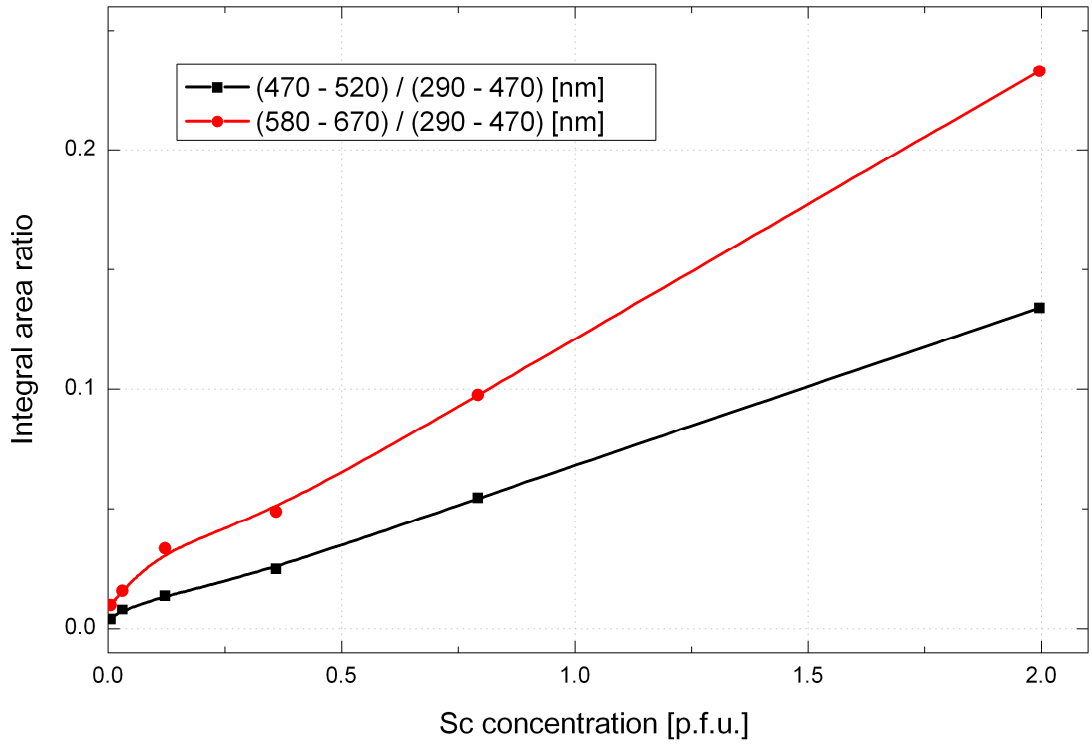

Figure 51: Dependence of the integral PL intensity ratios of emission from f–f transitions centered at 470–520 nm (^{3}P - ^{3}H) and at 580–670 nm (^{1}D - ^{3}H), to 5d–4f (^{3}H, ^{3}F) emission at 290–470 nm on Sc concentration (for further details see [116])

5.2.4. Decay kinetics

The influence of Sc codoping on decay time of Pr in LuAG is shown in Figure 52. A detail of decay start is in the inset graph. The reconvolution curves of samples with constant Pr content show initial increase of decay time. The Sc concentration 0.122 p.f.u. and higher seem to cause decrease of the decay time. There is an apparent step in the decay curves shown in the graph in Figure 52. The decay time is shortened from 20 ns at low to 19 ns at high Sc doping. This is very small change, close to the error of the reconvolution method. Only negligible long component was found in all samples.

The 5d - 4f decay kinetics for both Pr^{3+} and Ce^{3+} ions were measured in the PrScCe codoped samples. The measured data and fitted decay curves are shown in Figure 53. The samples were excited in the 5d absorption bands of Pr^{3+} or Ce^{3+} ions. The samples were excited at 282 nm for Pr emission and at 340 nm for Ce emission. The emission was collected at 320 nm for Pr and at 520 nm for Ce. The reconvolution fit of the decay curves minimized influence of excitation pulse width, especially for the fast PL emission of Pr^{3+}. There are two components for Pr^{3+} emission present, with a dominant 18 ns component and much weaker approx. 100 ns component. This slow component is also present in undoped layers. It is likely from

the host lattice or substrate (which contains small quantity of color centers). Some of the color centers detected in absorption spectra do absorb near 280 nm and it means that they are also excited. Only a 55 ns component was observed for Ce^{3+} emission. The decay times obtained from fits for both Pr^{3+} and Ce^{3+} ions are in agreement with those reported for the Czochralski grown single crystals [117]. From PL decay curves can be concluded that these layers do not have any significant energy loss from Pr^{3+} or Ce^{3+} ions due to impurities.

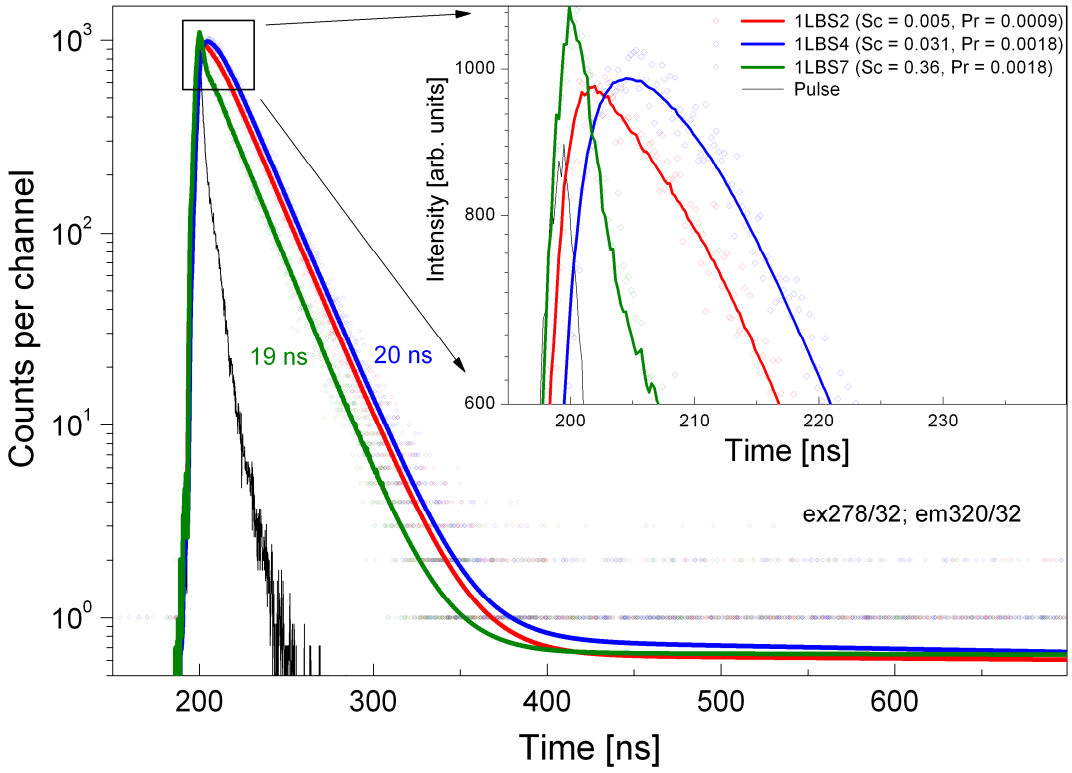

Figure 52: Decay kinetics curves of ScPr codoped LuAG epitaxial layers measured at emission, λ_{em} = 320 nm and λ_{exc} = 278 nm with both slits opened to 32 µm. The solid lines are a reconvolution fit curve with the black curve of instrumental response. All concentrations are in p.f.u.

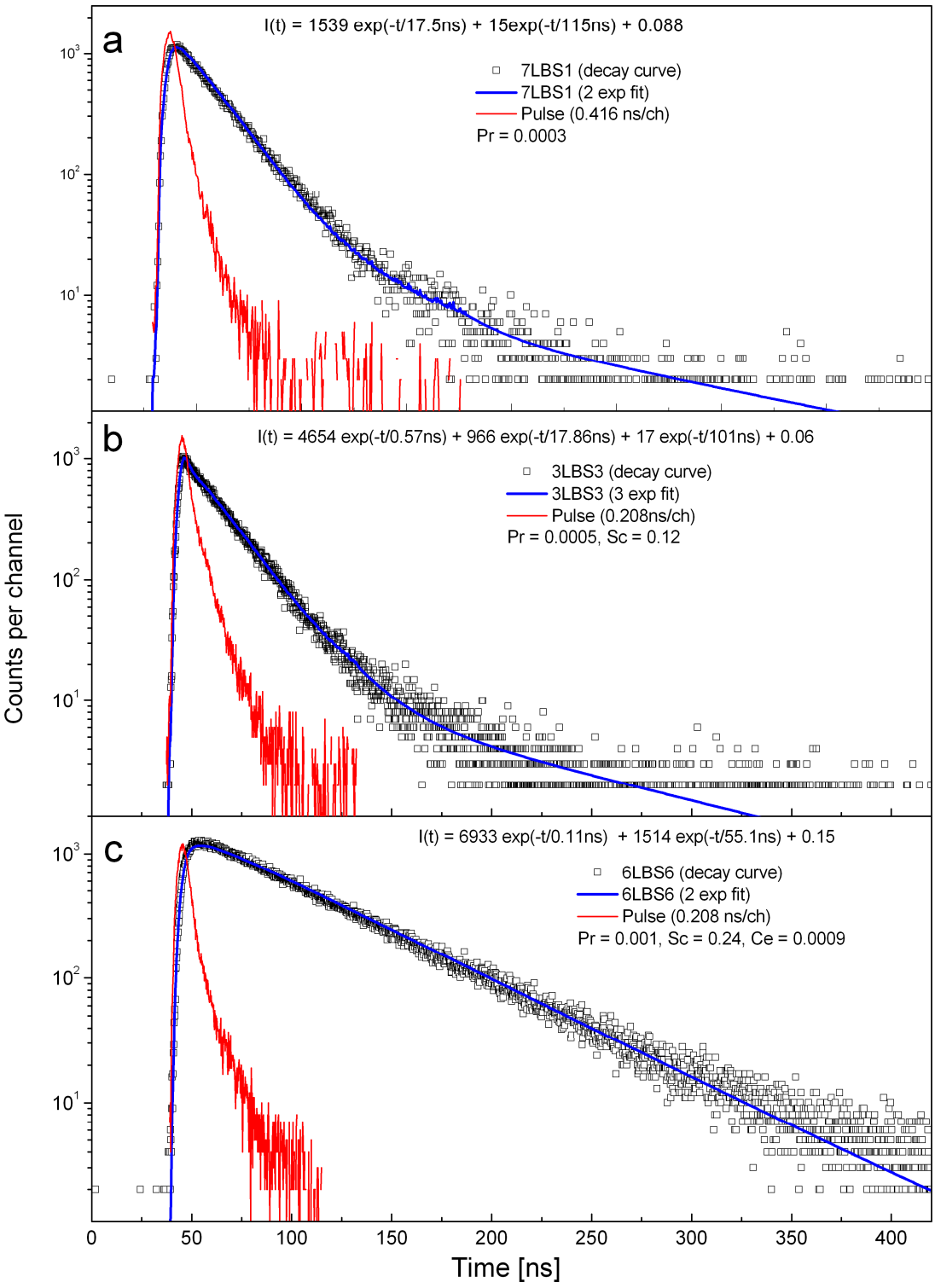

Figure 53: Decay kinetics curves of Pr, ScPr and ScPrCe doped LuAG epitaxial layers measured for (a,b) Pr^{3+} ion (5d–4f) emission, λ_{em} = 320 nm and λ_{exc} = 282 nm and (c) Ce^{3+} (5d–4f) emission, λ_{em} = 520 nm and λ_{exc} = 349 nm. The solid blue line is a reconvolution fit curve (I(t) noted in legend) with the red curve of instrumental response (for further details see [116])

5.2.5. Radioluminescence

The X-ray excitation source voltage was set to 10 kV and current to 50 mA for RL spectra measurement. Emitted light was measured in the spectral range from 200 nm to 670 nm. All measured RL spectra were compared with reference BGO single crystal ($Bi_4Ge_3O_{12}$). The RL spectra of Sc doped LuAG layers are shown in Figure 54 a. These spectra are in good agreement with the results in reference [118]. Maximal Sc^{3+} emission is observed at 265 nm for the lowest Sc doping, 0.02 p.f.u. The peak of RL intensity shifts with increasing Sc concentration up to 290 nm for 1.996 p.f.u. The intensive Sc RL emission originates from exciton radiative recombination on Sc center. There is also present a side peak at 370 nm that disappears at high doping levels. The shift of the main peak and disappearance of side peak can be explained by forced occupation of both octahedral and dodecahedral sites by Sc at high doping levels. The RL spectra of Pr doped LuAG layers are shown in Figure 54 b. The maximum of Pr^{3+} RL emission is at 308 nm for 5d - 4f transitions and resembles the PL spectra shown in Figure 50 a. The sharp 4f – 4f transitions of Pr^{3+} are greatly suppressed in the RL spectra due to measurement with wide slits. Only a negligible wide peak around 488 nm can be distinguished.

The RL spectra of ScPr co-doped LuAG layers are displayed in Figure 55. The integral RL intensity of shown spectra is significantly higher compared to that of the BGO reference single crystal. We can identify the main contributions from individual ions thanks to the RL spectra of LuAG doped with either Sc (Figure 54 a) or Pr ions (Figure 54 b) only. The Sc^{3+} and Pr^{3+} related peaks are positioned at 280 and 308 nm respectively, see in Figure 55. From the absorption spectra shown in Figure 48 can be seen an overlap of Sc RL emission peak with Pr^{3+} absorption, thus we can assume that an energy transfer from Sc to Pr centers is possible. The integral RL intensity of ScPr:LuAG samples increased with Sc content by 60 – 80% for Sc doping in the range from 0.24 to 0.575 p.f.u. The intensity of Sc peak at 280 nm increases with the Sc concentration. From this phenomenon can be assumed that there is a connection between Sc doping and the Pr emission. A considerable increase in intensity of the Pr^{3+} peak at 308 nm is correlated with increase of Sc content while the Pr content is constant. This is clearly seen in Figure 55 a. This dependency was observed even for high Sc concentrations up to 0.575 p.f.u. The transfer of the excitation energy from Sc^{3+} to Pr^{3+} activator ions can explain it. While for low Sc content we observe a proportional increase in RL intensity, shown in left graph of Figure 55, the contribution to RL decreases for higher Sc content (higher than 0.792 p.f.u.). The RL intensity of 5d – 4f emission band in the UV region is increasingly quenched for high Sc-doped samples (see Figure 55 b). Most probable cause is concentration quenching and nonradiative transfer of energy to ^3P and ^1D terms as it can be deduced from Figure 57. It is apparent that the RL intensity in the UV range is greatly reduced for 1.996 p.f.u. of Sc.

The RL spectra are in accordance with the PL spectra. The f – f emission in the range from 480 nm to 615 nm is also greatly amplified when compared to the d - f emission thanks to Sc doping. Addition of Ce^{3+} ions in the ScPrCe:LuAG samples have very negative influence on the RL intensity of Pr^{3+} ions (see Figure 56). The observed yellow - green 5d – 4f emission of the Ce^{3+} ions is significantly weaker compared to the Ce:LuAG samples shown in previous chapter and also does not significantly increase with higher Ce concentration. Apparently, there was no energy transfer to Ce^{3+} ions. Instead, a quenching of Pr^{3+} emission due to Ce doping was observed.

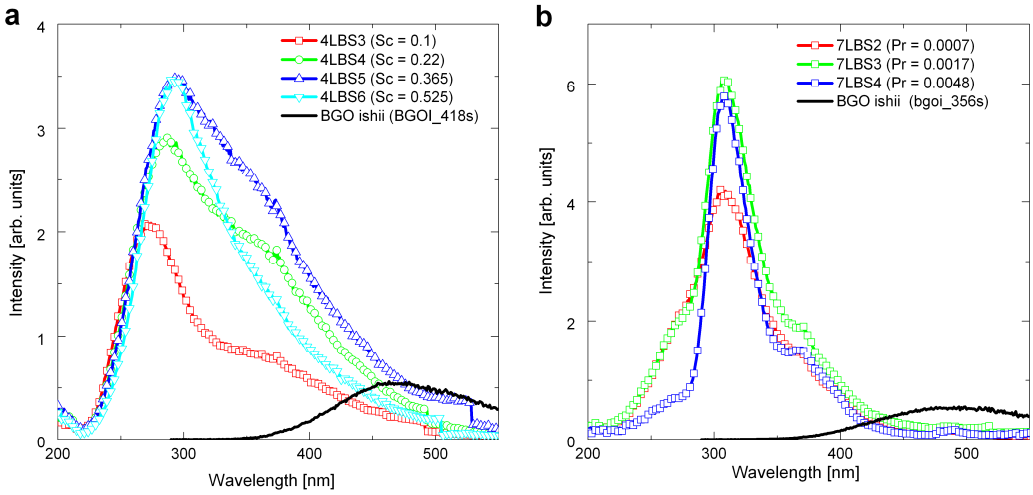

Figure 54: Radioluminescence spectra of a - purely Sc doped LuAG samples, and b - purely Pr doped LuAG samples, Concentrations of Pr and Sc in p.f.u. are noted in the legend, the reference spectra of BGO crystal plotted for comparison (see also in [116])

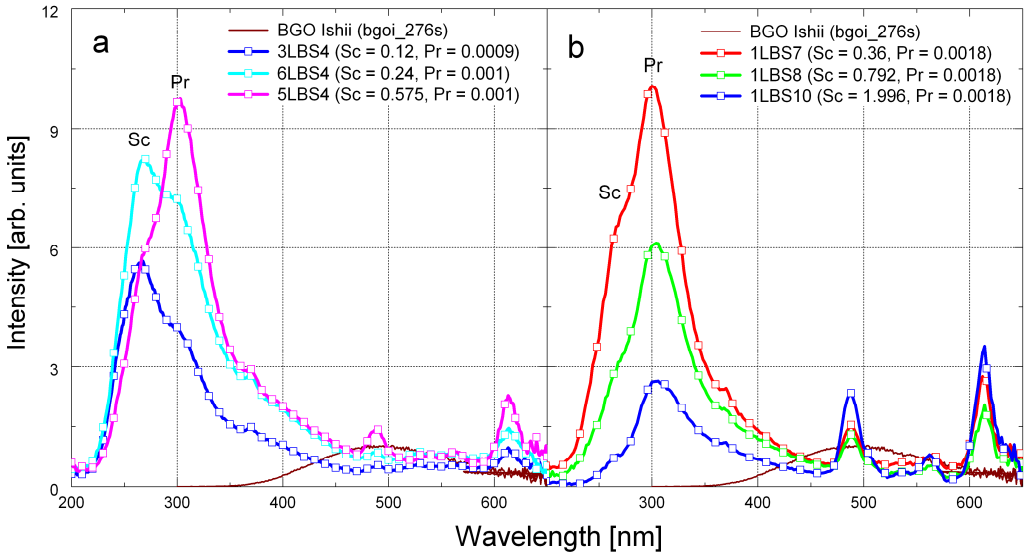

Figure 55: Radioluminescence spectra of ScPr codoped LuAG samples, a - samples with low up to medium Sc concentrations, b - heavily Sc doped samples. Concentrations of Sc and Pr are noted in the legend in p.f.u. Pr content was nearly constant across the samples in both graphs. Contributions from Sc and Pr ions are marked. The spectra of BGO crystal plotted for reference (see also in [116])

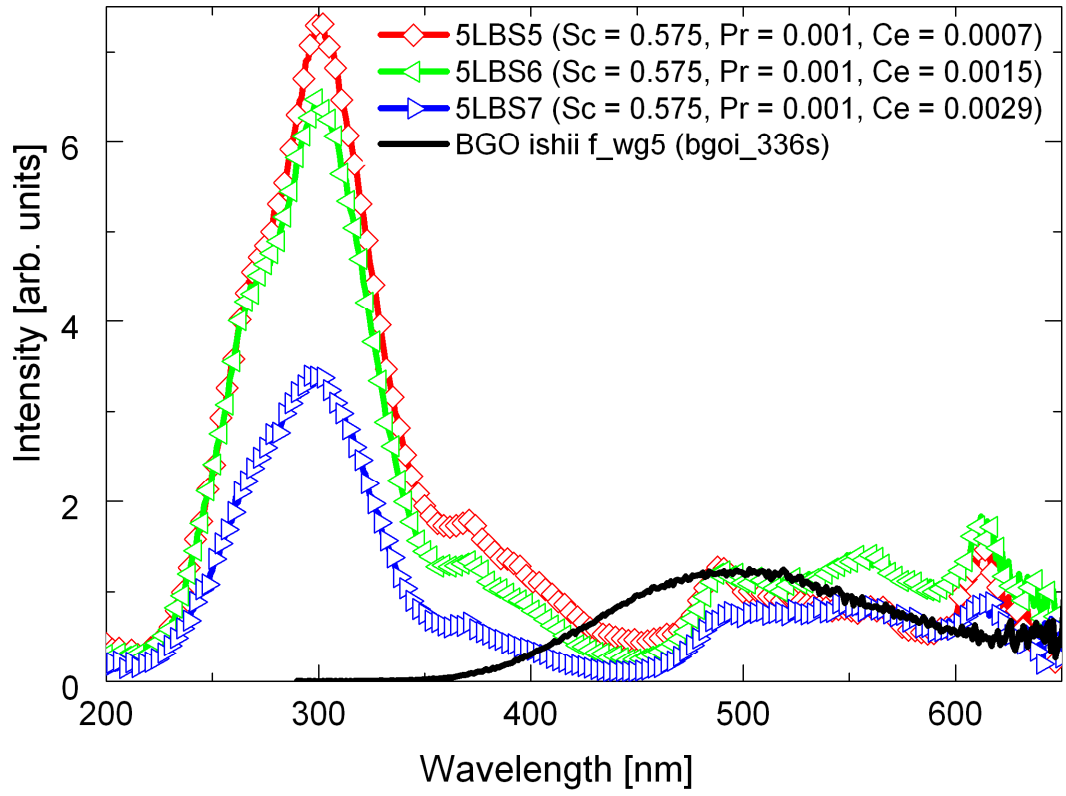

Figure 56: Radioluminescence spectra of ScPrCe codoped LuAG samples, samples with low and constant Sc and Pr and varying Ce concentration. Concentrations of dopants noted in the legend in p.f.u. The spectra of BGO crystal plotted for reference

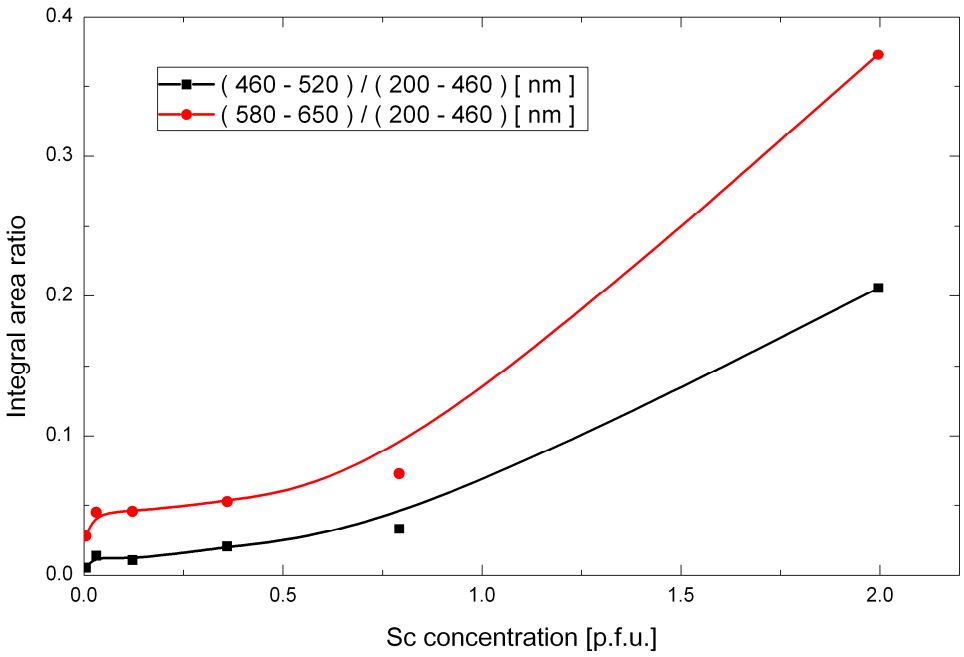

Figure 57: Dependence of the integral RL intensity ratios of emission from f–f transitions centered at 470–520 nm (^{3}P - ^{3}H) and at 580–670 nm (^{1}D - ^{3}H), to 5d–4f (^{3}H, ^{3}F) emission at 290–470 nm on Sc concentration

5.2.6. Scintillation properties

Photoelectron yield of Sc:LuAG, ScPr:LuAG, and ScPrCe:LuAG epitaxial layers were studied under alpha particle excitation (using ^{239}Pu alpha particle source, with particle energy 5.16 MeV). The largest photoelectron yield was observed for ScPr:LuAG layers with low concentrations of both Sc and Pr. Best result showed sample with 0.12 p.f.u. of Sc. The observed photoelectron yield was notably higher compared to the Czochralski grown Pr:LuAG single crystals in the best samples (see Figure 58). For higher Sc concentrations, the photoelectron yield decreases. It is interesting that the Sc doping change ratio between slow and fast components in the photoelectron yield. In low Sc-doped PrSc:LuAG samples are suppressed slow components, intensity of fast components is boosted and such layers have better performance when compared to the Czochralski Pr:LuAG single crystal. The time dependence curves of the photoelectron yield in the range of shaping times from 0.5 to 10 μs are in Figure 58. Shown ScPr:LuAG epitaxial layers are better than Pr:LuAG single crystals. The relative photoelectron yield (see Figure 58, b) increase in measured time frame only by 18 % for Sc content 0.12 p.f.u. and 23 % for 0.24 p.f.u. On the other hand, the photoelectron yield increases by more than 40 % in Pr:LuAG single crystals and it is still far from saturation even at the end of 10 μs shaping time window (see Figure 58). This clearly shows reduction of slow components in ScPr:LuAG epitaxial layers. Higher values at the beginning of photoelectron yield, at the shortest shaping time 0.5 μs, prove that the ratio between slow and fast components is in favor of the fast in layers when compared to the single crystals. The origin of slow components is delayed recombination. According to literature [6], they originate from antisite Lu_{Al} defects which are responsible for shallow electron traps present in single crystals. Sc substitution into the octahedral sites most probably interferes with the creation of the Lu_{Al} antisite defects and has positive effect on scintillation decay. However, the fraction of slow components in layers increases again at higher Sc concentrations, and for 0.575 p.f.u., the slow components represent roughly 45 % of photoelectron yield. More detailed study about photoelectron yield of ScPr co-doped LuAG is in literature [119]. Ce doping was found undesirable, because the Ce^{3+} decreases photoelectron yield even more than high Sc concentration. This result supports the facts from RL spectra measurements and other observations. The Ce^{3+} quenches emission of the Pr^{3+} and do not improve the scintillation properties of ScPr:LuAG.

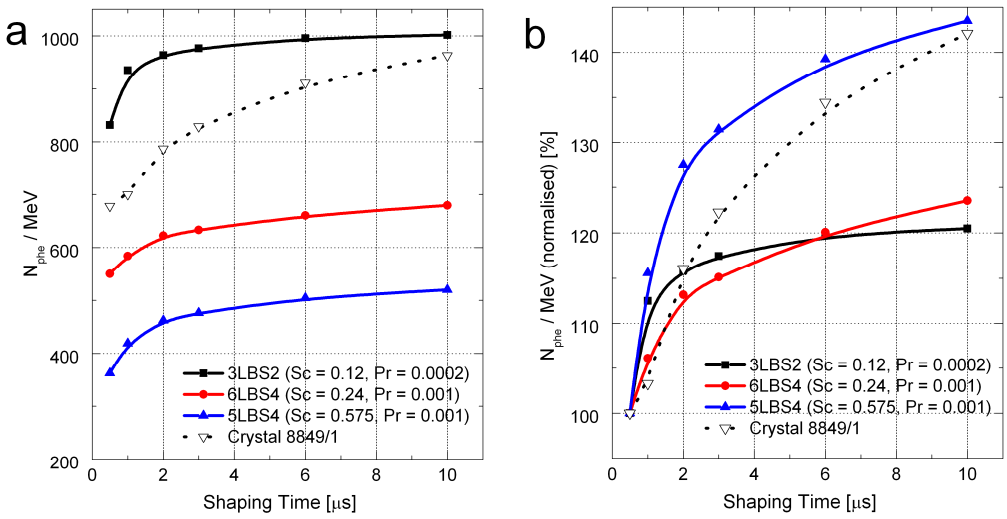

Figure 58: a - Photoelectron yield N_{phe} per MeV as function of shaping time under alpha particle excitation (source ^{239}Pu) of ScPr:LuAG epitaxial layers (concentrations of Sc and Pr, in p.f.u., are shown in the legend); b - Normalized photoelectron yield to the shortest shaping time of 0.5 ms for the same samples. Reference Czochralski grown single crystal of Pr:LuAG, sample 8849/1 included for comparison (see also in [116])

5.2.7. Summary

In this chapter, the growth and characterization of Sc codoped Pr:LuAG and Ce codoped Pr:ScLuAG epitaxial films were performed. From absorption measurements is clear, that Pr and Ce absorption peaks are not affected by Sc codoping.

In photoluminescence and RL of pure Pr:LuAG, most of the emission is in the 5d - 4f transitions in the UV band. PL of these epitaxial layers is similar to the single crystals. No Sc peaks are present in PL in Sc codoped samples, but significant 4f – 4f transitions peaks intensity increase occur. Ce codoping has detrimental impact on the PL and Pr UV luminescence is quenched.

Higher Sc concentration cause shortening of 5d - 4f decay time of Pr ions and increase of the f – f emission responsible for slow components.

The maximum integral radioluminescence signal was observed for samples with moderate Sc concentrations. The intensity was about 60 – 80 % higher when compared to samples of pure Pr:LuAG. Shown graphs in Figure 55 are proof of energy transfer from Sc^{3+} to Pr^{3+} ions.

The best photoelectron yield was obtained for lower Sc concentrations. Observed suppression of slow components is the most desirable effect of Sc codoping. Fast components have notably greater presence in layers when compared to the Czochralski grown crystals. Contradictory, the slow components increased and photoelectron yield started to decrease at higher Sc concentrations. This can be explained by emerging of new stable electron traps induced by the abundance of Sc ions. The Ce^{3+} quenches emission of the Pr^{3+} and do not improve the scintillation properties of ScPr:LuAG.

5.3. CePr:GdYAG

5.3.1. Sample summary

Goal of presented work on garnet epitaxial films was to use previously optimized LPE growth conditions for preparation and testing various structural compositions. The emphasis was put on photoluminescent properties, because of the intended use of such layers as a light emitting element. The aim was to study red shift and emission changes (color tuning) induced by Gd substitution and by energy transfer anticipated between Pr and Ce [58]. Influence of codoping on sample properties was studied. Summary of prepared samples for this study is listed in the table below. They were prepared from $BaO\text{-}B_2O_3\text{-}BaF_2$ flux (DBC series), and from $PbO\text{-}B_2O_3$ flux (DCe series). For dopants content in the following table are used values based on melt composition and estimated from segregation coefficient.

Sample	Layer thickness [μm]	Substrate	Growth temperature [℃]	z (Pr) [p.f.u.]	y (Ce) [p.f.u.]	x (Gd) [p.f.u.]
1DBC3	8.8	YAG	1030.4	0.000	0.005	0.784
1DBC4	7.9	YAG	1035.4	0.001	0.005	0.758
1DBC6	2.3	YAG	1030.7	0.004	0.005	0.758
1DCe1	13.1	YAG	1001.8	0.000	0.021	1.014
1DCe2	16.9	YAG	1001.2	0.004	0.022	1.022
1DCe3	3.8	YAG	1001.4	0.012	0.022	1.032

Table 11: Table of CePr:GdYAG – $(Y_{3-x-y-z}Gd_xCe_yPr_z)Al_5O_{12}$ samples from $BaO\text{-}B_2O_3\text{-}BaF_2$ flux (DBC series) and $PbO\text{-}B_2O_3$ flux (DCe series), the concentrations are derived from melt content as atoms per formula unit (p.f.u.)

5.3.2. Absorption

The spectra of the absorption coefficient of Ce-doped multicomponent LuAG films are shown in Figure 59. There is a clear peak shift of Ce^{3+} 4f - 5d transitions (from 339 nm to 346 nm and from 463 nm to 453 nm) with change of crystal field as Lu is introduced in the crystal lattice for 8LBS6 sample. The broad bands at 240 nm and 282 nm come from parity allowed 4f – 5d of Pr^{3+} transitions to the two lowest levels 5d (^{2}D) states that are split by crystal field. The parity forbidden f – f transitions of Pr^{3+} were not noticeable in the absorption spectra due to low doping and low thickness of the layers. The Gd^{3+} ions f – f transitions are present, but with extremely low absorption within range from 308 nm to 318 nm and more noticeable

contribution at around 276 nm in samples 1DCe1 and 2 spectra (highest Gd concentration).

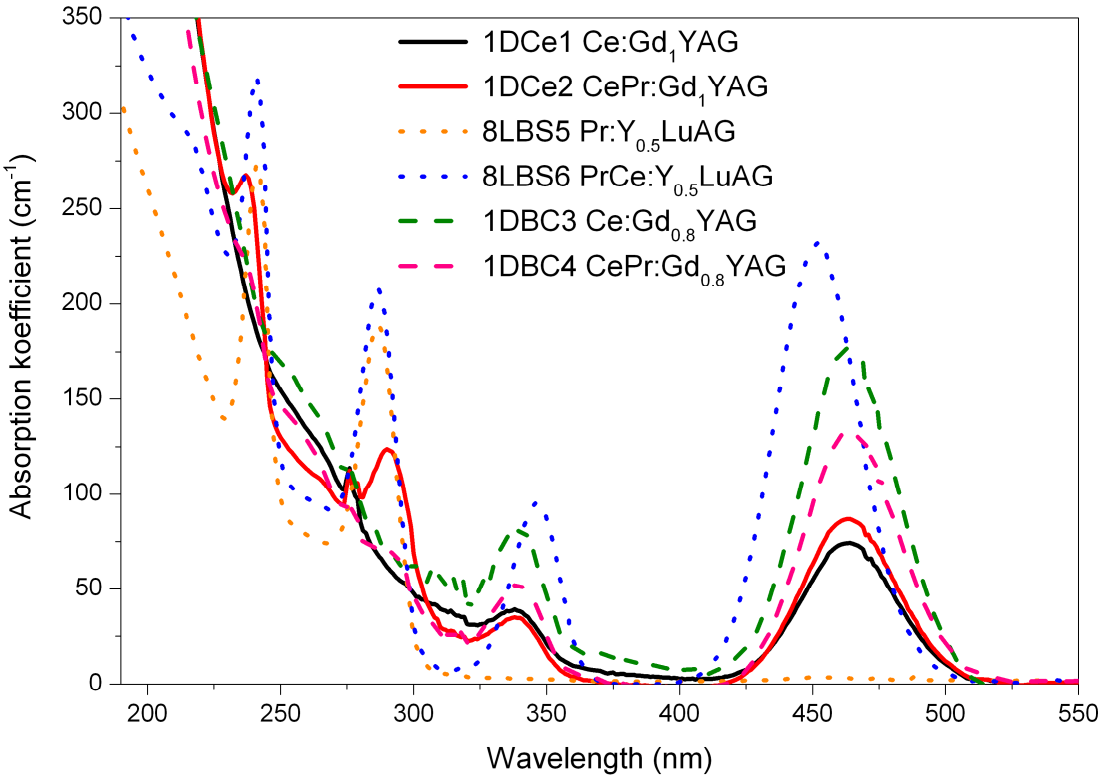

Figure 59: Absorption coefficient spectra for multicomponent garnet layers. The CePr:GdYAG samples compared to CePr:YLuAG samples.

5.3.3. Photoluminescence

The excitation and emission spectra of the PL were measured in the spectral range from 200 nm to 850 nm. The excitation energies are below the band gap of the host material. The samples doped with Pr^{3+} ions show superimposed wide band of 4f - 5d transitions of Ce^{3+} ions peaking at 546 nm and sharp peaks of f – f transitions of Pr^{3+} at 608 nm in emission spectra. The Gd^{3+} ions have f – f transitions peaks at 273 nm, 301 nm, 307 nm and 312 nm superimposed onto excitation spectra of Ce^{3+} 4f - 5d transitions. It is shown in Figure 60, that the emission peak of Ce is reduced in favor of Pr one with increasing concentration of Pr and overall intensity tends to increase in DBC series in contrast to DCe series. This means, that the impurities from PbO melt have negative impact on emission. Analogous tendencies are seen when the PL was excited at Pr peak at 608 nm, shown in Figure 61.

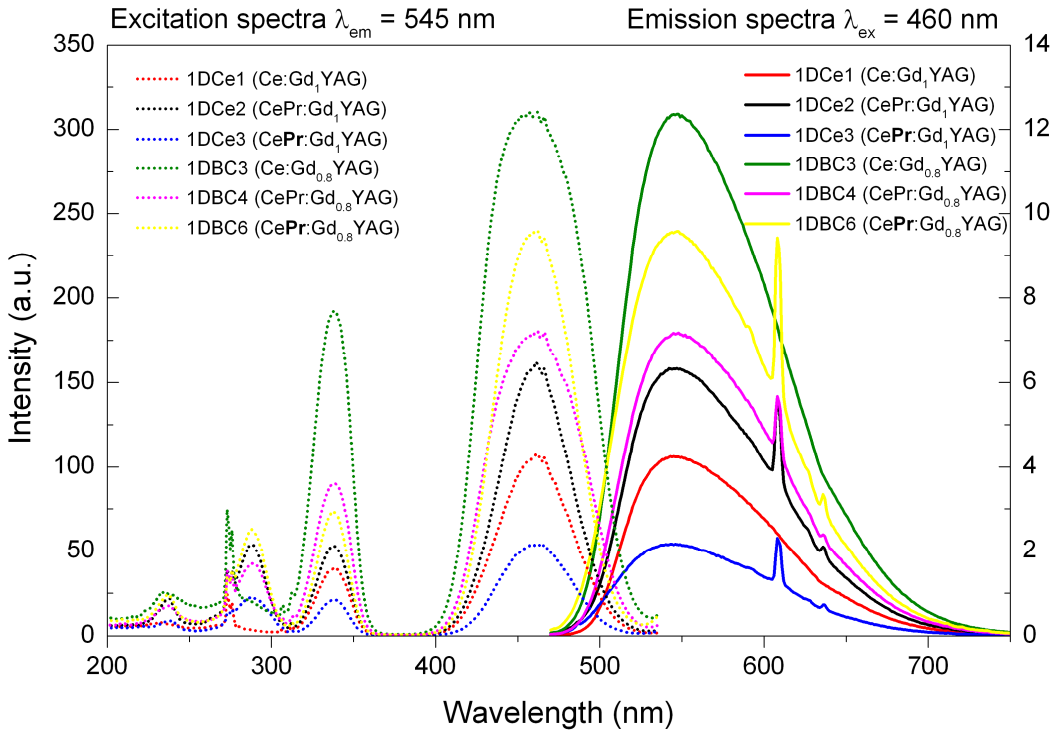

Figure 60: PL in Ce^{3+} peaks, where excitation spectra (emission at 545 nm) and emission spectra (excited at 460 nm) of Ce and Pr co-doped Gd:YAG samples show initial decrease of PL intensity as Pr is introduced and then increase with higher Pr content for BaO flux grown samples. PbO grown layers show opposite behavior (bold Pr means increased concentration).

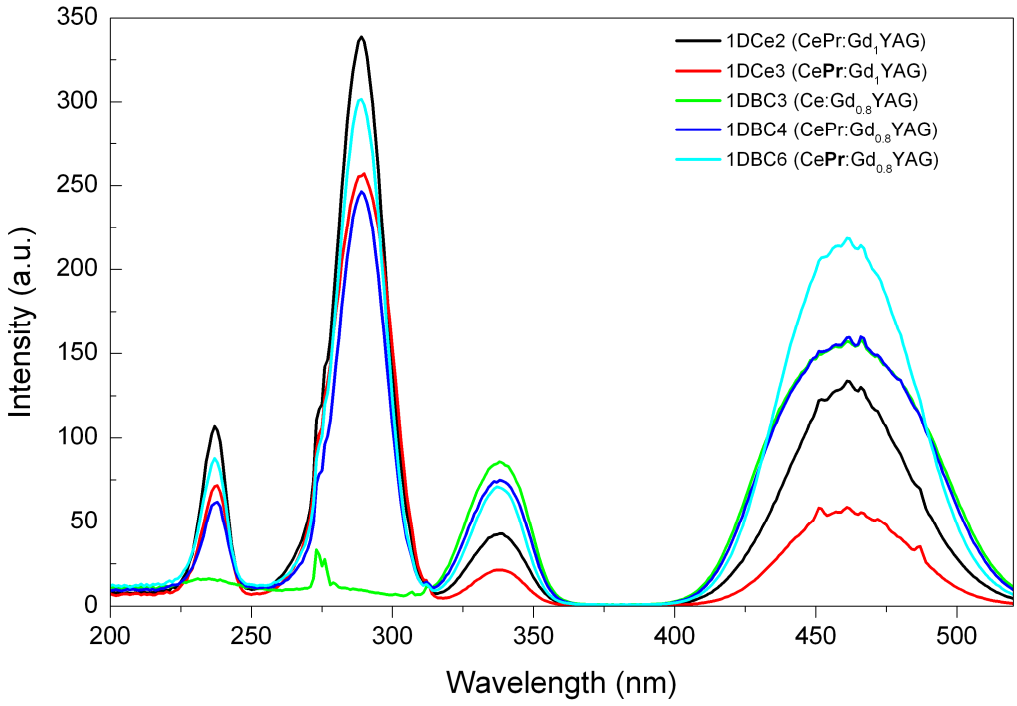

Figure 61: PL excitation spectra (emission at 608 nm) in Pr^{3+} peak of Ce and Pr co-doped Gd:YAG samples show quite similar behavior as in Ce^{3+} peaks

Spatial distribution of light emitted with a blue LED excitation source is shown in Figure 62 for PbO flux grown samples and in Figure 63 for BaO flux grown samples. The LEDs emission peaks at 461 nm and its power was regulated by a current source that was set at 0.04 A. The emission spectrum is greatly dependent on the measurement angle. There is a clear evidence of waveguide effect when measured at steep angles even when the surface quality of the sample was far from optimal. As the samples were rotated counterclockwise (CCW) to the edge, the excitation light slowly decreased in intensity, until it vanished from the spectra and at the same time, the emission light increased its intensity. The emission was most intense at the edge of the sample due to the waveguide effect. This means, it will be necessary to grow the layers with very rough surface for more even spectral distribution.

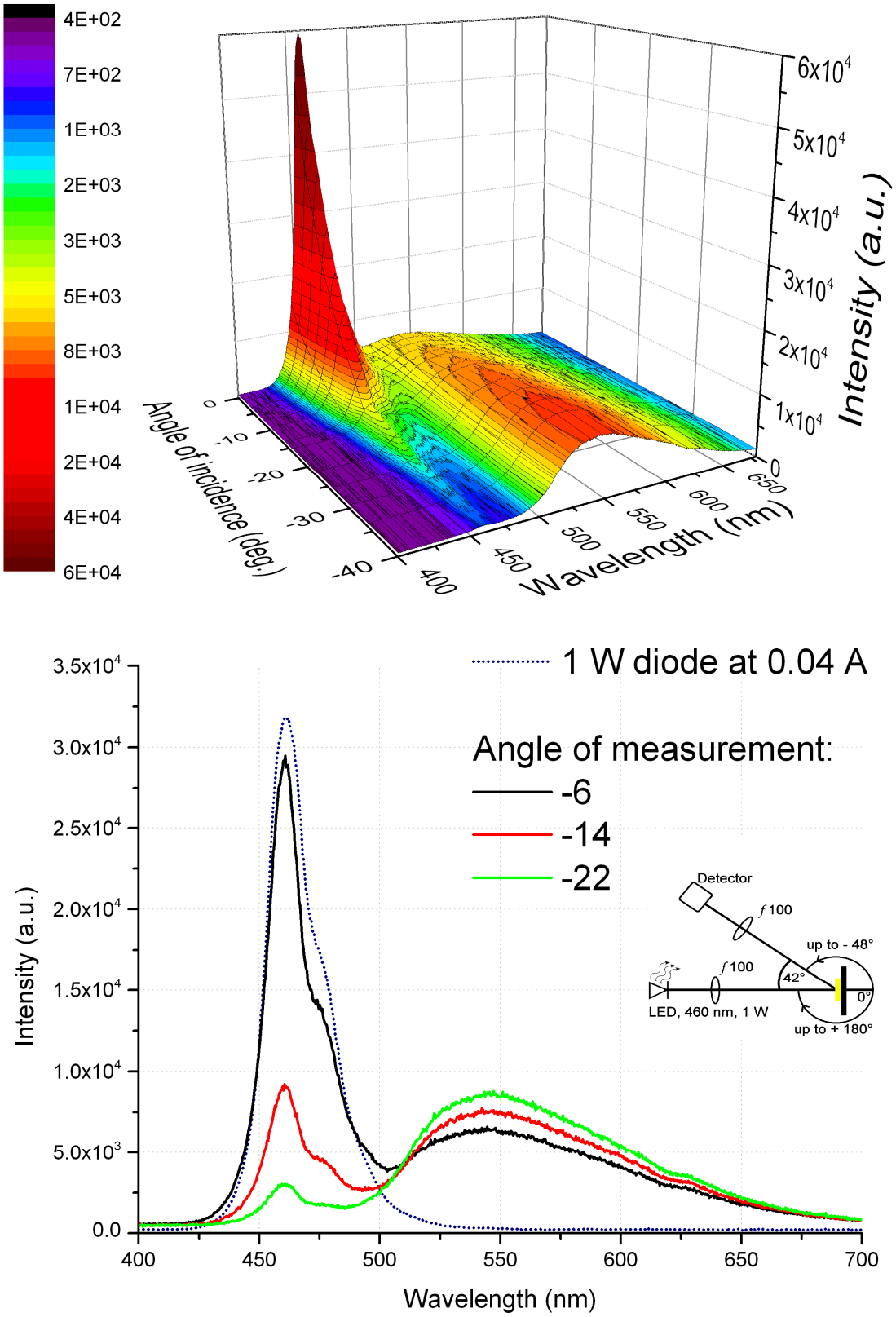

Figure 62: Angular dependence of emission spectra for multicomponent garnet layer. Excited by 1 W diode set to operate at 0.04 A and at peak wavelength at 461 nm. The CeGd:YAG sample 1DCe1 was observed from angle directly reflecting diode light (approx. 21 degrees) to angle, where dominates the waveguide effect (approx. negative 40 degrees). The upper is a 3D plot from measured data, on the lower graph are selected emission spectra compared to spectra of the excitation diode.

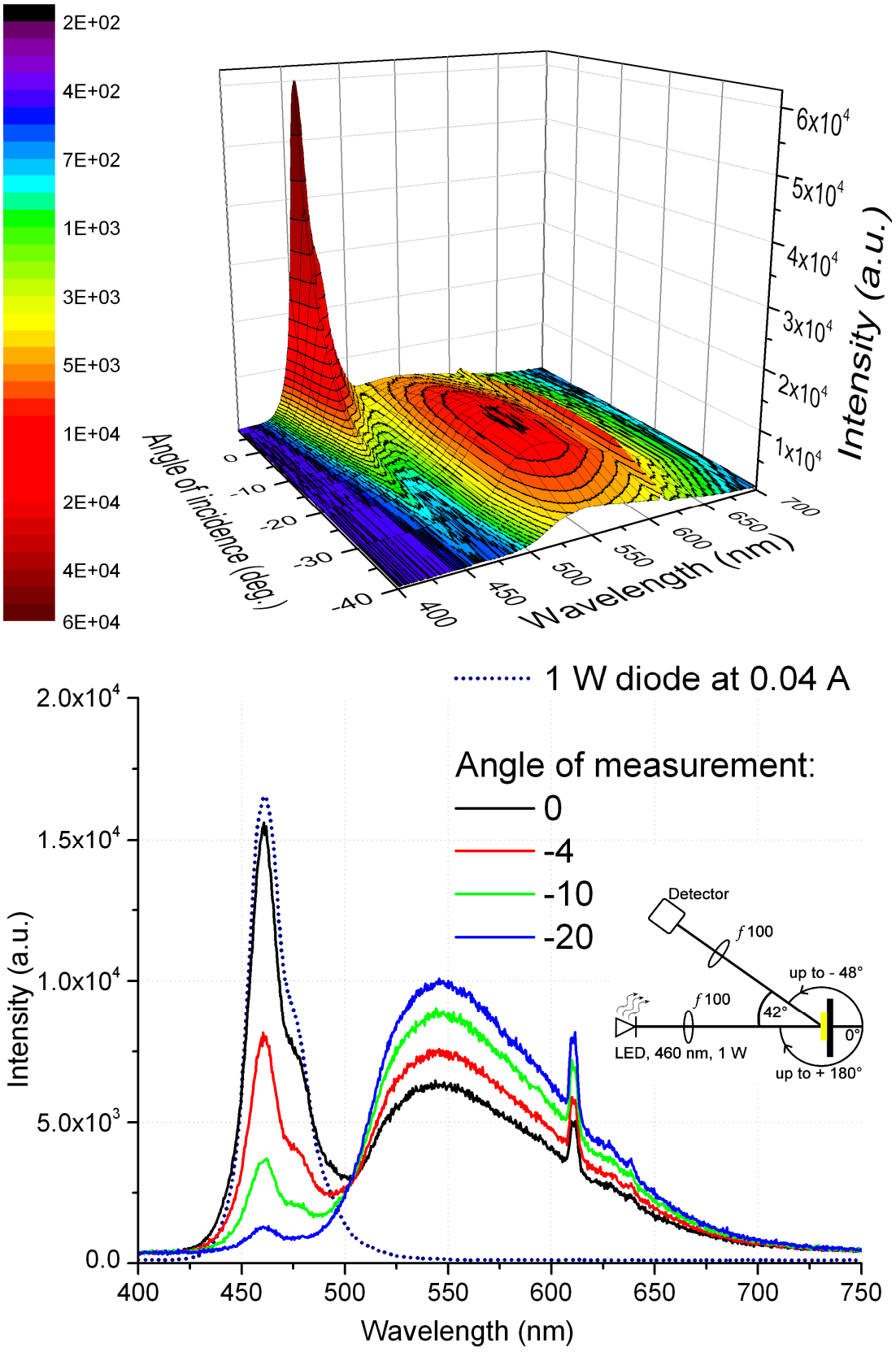

Figure 63: Angular dependence of emission spectra for multicomponent garnet layer. Excited by 1 W diode set to operate at 0.04 A and at peak wavelength at 461 nm. The CePrGd:YAG sample 1DCe2 was observed from angle directly reflecting diode light (approx. 21 degrees) to angle, where dominates the waveguide effect (approx. negative 40 degrees). The upper is a 3D plot from measured data, on the lower graph are selected emission spectra compared to spectra of the excitation diode.

5.3.4. Summary

From experiments conducted in this chapter can be concluded, that the multicomponent garnet epitaxial films are perspective for color tuning of high-powered white LEDs. Most suitable method is epitaxial growth from BaO based flux because the emission intensity of these samples is stronger than from PbO based flux samples. For practical use as light source, white balance is important. Unfortunately, the white balance is quite strongly angle dependent.

5.4. Tb:LuAG and Tb:YAG

5.4.1. Sample summary

The Tb-doped garnet epitaxial layers have slow (~ 1 ms), but intense green emission of Tb^{3+} ions. Their application is in scintillation screens where fast response is not required. Goals of presented work on Tb-doped garnet epitaxial films were comparison of LPE grown samples to Czochralski grown single crystals [120-122] and further improvement by Sc codoping. An increase of light output due to energy transfer from Sc to Tb centers similar to PrSc codoped garnets was anticipated based on structure of energy levels.

Influence of doping and codoping on sample properties was studied. Brief summary of prepared samples for this study is listed below. All are prepared from BaO-B_2O_3-BaF_2 flux. For dopant content in the following tables are used either values based on melt composition and estimated from segregation coefficient or results from EPMA and GDMS measurements for several of these samples. The 1LBT batch of samples was grown to discern Tb luminescence and its concentration dependence. Series 2LBT and 3LBT were prepared in order to study influence of high and low Sc codoping on Tb:LuAG luminescence. In 2LBT series was Tb concentration constant and in 3LBT series was Sc concentration constant.

Sample	Layer thickness [μm]	Substrate	Growth temperature [℃]	y (Sc) [p.f.u.]	x (Tb) [p.f.u.]
1LBT1	18.0	LuAG	1024.8	0	0
1LBT2	17.3	LuAG	1030	0	0.004
1LBT3	20.4	LuAG	1035.3	0	0.015
1LBT4	17.7	LuAG	1040.4	0	0.072
1LBT5	17.7	LuAG	1045	0	0.298
2LBT1	11.9	LuAG	1045	0.098	0.298
2LBT2	13.3	LuAG	1044.8	0.196	0. 298
2LBT3	7.9	LuAG	1045.5	0.296	0. 298
2LBT4	9.8	LuAG	1037.3	0.425	0. 298
2LBT5	12.4	YAG	1038.5	0.425	0. 298
2LBT6	12.7	YAG	1038.5	0.578	0. 298
2LBT7	10.7	YAG	1039.4	0.803	0. 298
2LBT8	14.7	YAG	1039	1.204	0. 298
3LBT1	16.1	LuAG	1040.2	0.252	0
3LBT2	13.0	LuAG	1040.2	0.252	0.006
3LBT3	14.3	LuAG	1045	0.251	0.015
3LBT4	15.9	LuAG	1049.8	0.25	0.029
3LBT5	12.5	LuAG	1044.5	0.252	0.074
3LBT6	21.4	LuAG	1048.7	0.252	0.297
3LBT7	11.4	LuAG	1054.4	0.254	0.601

Table 12: Table of TbSc:LuAG – $(Lu_{3-x}Tb_x)(Al_{5-y}Sc_y)O_{12}$ samples from $BaO\text{-}B_2O_3\text{-}BaF_2$ flux (concentration of scandium and terbium were determined from melt content suggesting segregation coefficient k and is given as atoms per formula unit (p.f.u.); For k_{Tb} it was ~ 1 and k_{Sc} ~ 1)

	Tb x 10	Sc
1LBT3	0.12	0
1LBT5	2.26	0
2LBT2	2.34	0.24
2LBT8	3.13	1.35

Table 13: Table of content analysis data for selected few TbSc:LuAG – $(Lu_{3-x}Tb_x)(Al_{5-y}Sc_y)O_{12}$ samples from $BaO\text{-}B_2O_3\text{-}BaF_2$ flux, the concentrations are given as atoms per formula unit (p.f.u.); (GDMS analysis)

	Tb x 10^2	Sc x 10^2	Pt x 10^2	B x 10^2
1LBT3	0.96	0	0.06	6.03
3LBT2	0.41	16.26	0.04	4.45

Table 14: Table of content analysis data for selected few TbSc:LuAG – $(Lu_{3-x}Tb_x)(Al_{5-y}Sc_y)O_{12}$ samples from $BaO\text{-}B_2O_3\text{-}BaF_2$ flux, the concentrations are given as atoms per formula unit (p.f.u.); (GDMS analysis)

	Tb x10	Lu	Al	Sc x10	Pt	O	Sum of a and d sites
1LBT2	0.03	2.73	5.27	0	0	11.995	5.265
1LBT3	0.12	2.67	5.32	0	0	11.982	5.318
1LBT4	0.55	2.73	5.21	0	0	11.999	5.215
1LBT5	2.32	2.52	5.25	0	0	11.999	5.250
2LBT1	2.35	2.54	5.15	0.83	0	11.999	5.230
2LBT2	2.16	2.51	5.04	2.41	0	11.999	5.277
2LBT3	2.14	2.48	5.02	2.86	0	11.999	5.305
2LBT4	2.46	2.44	4.72	5.92	0	11.999	5.311
2LBT5	2.71	2.44	4.81	4.88	0	11.999	5.294
2LBT6	2.76	2.44	4.63	6.61	0	11.999	5.288
2LBT7	2.99	2.38	4.35	9.69	0	11.999	5.323
2LBT8	3.24	2.26	4.07	13.44	0	11.999	5.416
3LBT1	0.04	2.72	5.01	2.64	0	11.994	5.273
3LBT2	0.04	2.76	5.00	2.41	0	11.992	5.237
3LBT3	0.22	2.73	5.01	2.40	0	11.999	5.251
3LBT4	0.25	2.77	4.99	2.19	0	11.959	5.207
3LBT5	0.38	2.72	5.01	2.31	0	11.999	5.241
3LBT6	2.19	2.52	5.00	2.67	0	11.999	5.265
3LBT7	4.56	2.24	4.99	3.12	0	11.999	5.301

Table 15: Table of content analysis data for selected few TbSc:LuAG – $(Lu_{3-x}Tb_x)(Al_{5-y}Sc_y)O_{12}$ samples from $BaO\text{-}B_2O_3\text{-}BaF_2$ flux, the concentrations are given as atoms per formula unit (p.f.u.); (EPMA analysis, overall sum of cations normalized to 8, oxygen calculated as remainder)

5.4.2. Absorption

The transmittance was measured in range from 190 to 1100 nm. Calculated optical density spectra of Tb doped LuAG in the range of 4f - 5d transitions are shown in Figure 64 and spectra of TbSc codoped LuAG are in Figure 65. Samples grown with low layer to substrate lattice mismatch show high transparency. The transmittance was above 80% in general. Samples grown with high lattice mismatch (Δa from roughly 0.04 up to 0.14 Å) have matte surface and characteristic strong scattering. The main broad absorption band is located at 270 nm, second and weaker one is at 230 nm. Their sources are parity allowed transitions from terbium 4f shell to crystal field splitted 5d (^{2}D) excited states. Absorption lines belonging to forbidden f - f (Tb^{3+}) transitions were not detected in the layers, because of their small thickness.

Absorption belonging to Sc ions was not observed in the absorption spectra as can be seen in Figure 65. Increased absorption below 210 nm comes probably from band gap changes caused by Sc ions or due to contamination from the flux. Slight decrease in crystal field splitting of 5d states of Tb ions and their shift closer together induced by Sc doping can be seen in Figure 65.

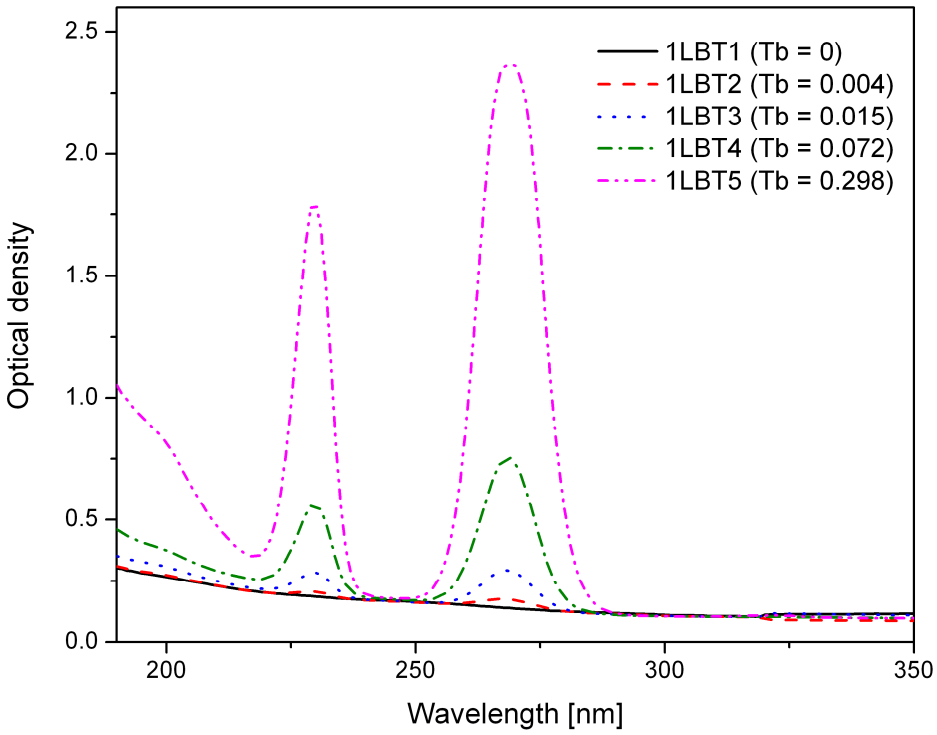

Figure 64: Optical density of Tb:LuAG epitaxial layers with 4f - 5d Tb transitions. Concentrations of Tb ions are noted in the legend in p.f.u. (for details see [123])

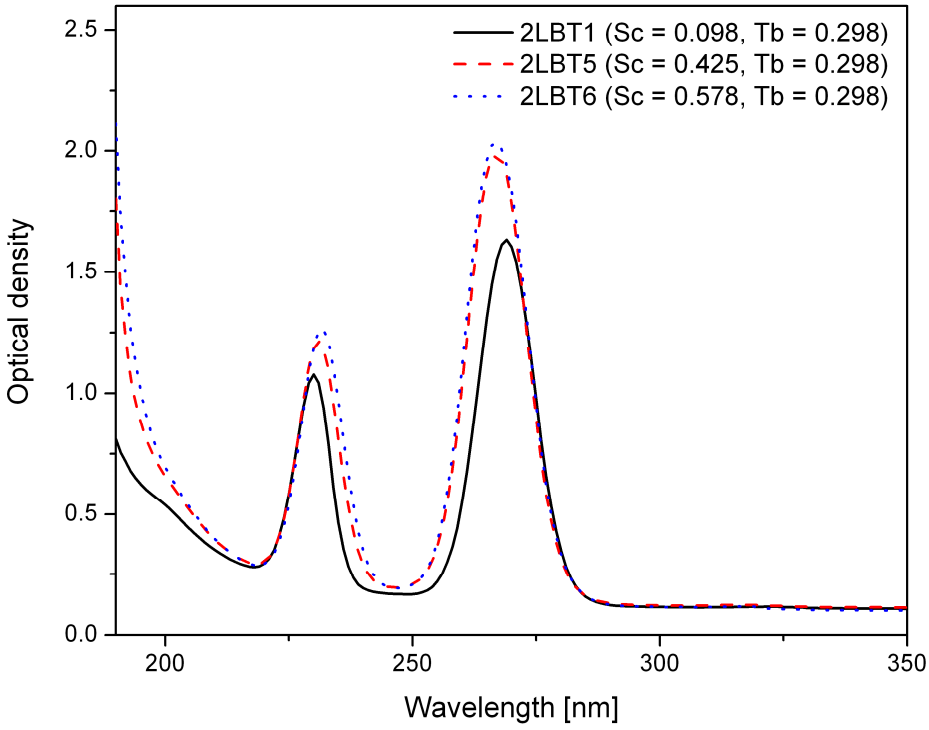

Figure 65: Optical density of TbSc:LuAG epitaxial films showing 4f - 5d Tb transitions. Concentrations of Tb and Sc ions are noted in the legend in p.f.u. (for details see [123])

5.4.3. Photoluminescence

The PL excitation and emission spectra were measured in the range from 200 to 750 nm in 0.5 nm steps. Measured PL spectra of Tb:LuAG with increasing concentration of Tb are shown in Figure 66. The spectra of TbSc:LuAG samples for constant Tb and varying Sc concentrations are in Figure 67. The PL emission in the samples was excited at wavelength λ_{ex}, 270 nm, corresponding to the Tb^{3+} 5d states. No d - f emission of Tb ions was observed in both Tb:LuAG and TbSc:LuAG samples. A transfer of excitation energy down from the 5d states to near 4f states was observed. It consisted of an intense f - f ($^5D_{3,4} \rightarrow {}^7F_j$) emission in bands composed of sharp lines within the spectral range from 370 nm to 630 nm. Concentration quenching was observed with increasing Tb content in $^5D_3$ multiplet occupying the interval of wavelengths from 370 to 470 nm. This was identified as a cross-relaxation effect in [120, 124]. When the Tb content is increased above 0.072 p.f.u., this emission becomes completely quenched and the excitation energy is transferred to the nearby multiplet $^5D_4$, with lower energy and with emission in the spectral range from 480 nm to 630 nm. Thus, the green emission line at 543 nm at higher Tb content dominates. The excitation spectra were measured in this emission line. Figure 66 also shows that the 270 nm band of the excitation spectra becomes deformed at higher Tb concentrations due to self-absorption.

The Sc content was increased up to 1.204 p.f.u. while Tb content was kept constant for TbSc:LuAG films presented in Figure 67. No Sc related peaks in either excitation or emission spectra were observed. We simply could not reach excitation wavelengths needed for Sc luminescence. Notable increase of intensity of $^5D_4$ emission is observed in the samples where Sc content rises above 0.425 p.f.u. The PL intensity does not change much for higher Sc content. Concentration quenching of Tb PL emission is not observed even for the highest Sc concentrations.

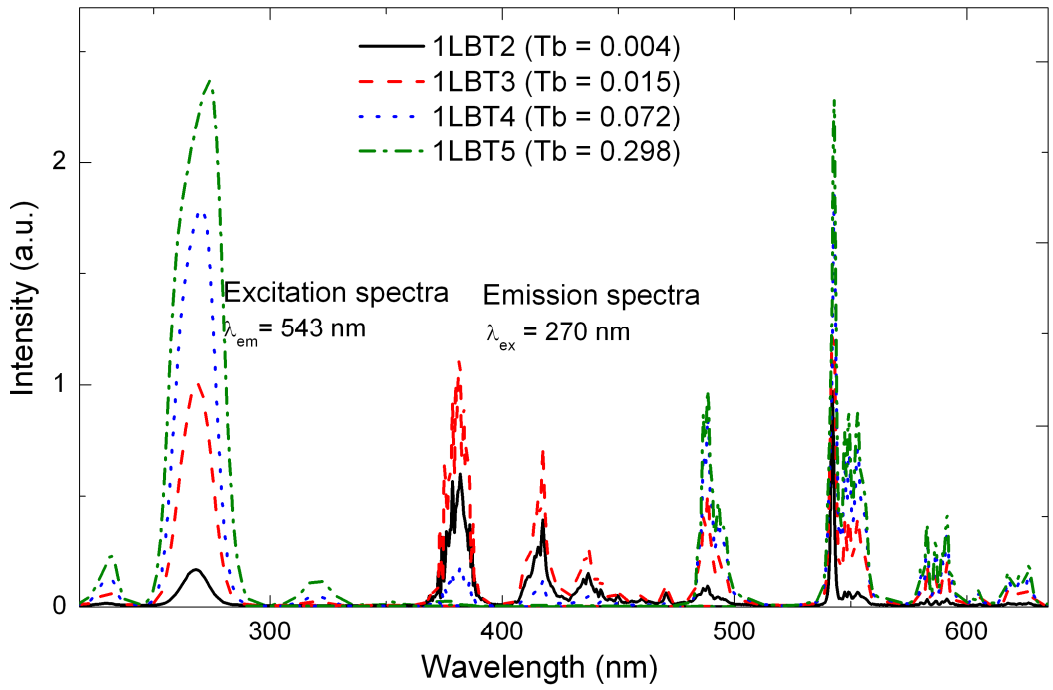

Figure 66: PL excitation (λ_{em} at 543 nm) and emission (λ_{ex} at 270 nm) spectra of Tb doped LuAG samples. Concentrations of dopants in presented layers are noted in legend in p.f.u. (for details see [123])

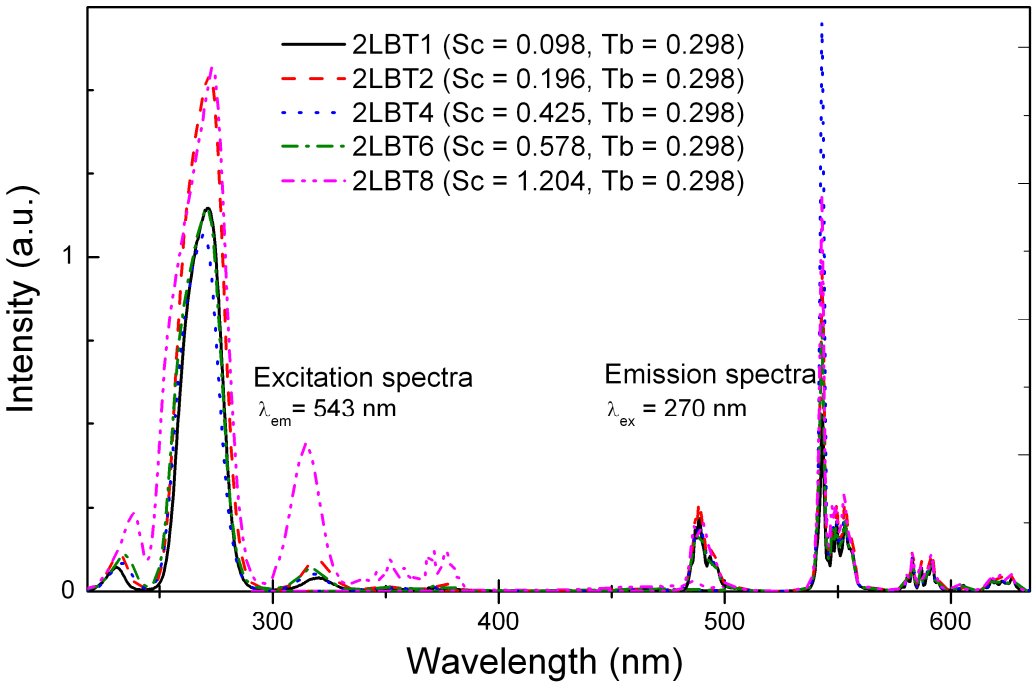

Figure 67: PL excitation (λ_{em} at 543 nm) and emission (λ_{ex} at 270 nm) spectra of Tb:LuAG samples codoped with Sc. Concentrations of dopants in presented layers are noted in legend in p.f.u. (for details see [123])

5.4.4. Decay kinetics

The decay kinetics was measured for additional information on the effects connected to Tb^{3+} and Sc^{3+} doping. Decay measurements of Tb^{3+} ions at emission in $^5D_4$ provide more detailed information about potential concentration quenching. The samples were excited in the 5d band of Tb^{3+} with excitation at 270 nm and Tb emission was collected at 543 nm. The $^5D_3$ emission was not studied, because it is totally quenched in most of the samples.

Decay curves of chosen samples with low and high Tb and Sc concentrations are shown in Figure 68. The reconvolution fits of these decay measurements are single exponential with dominant decay time of approx. 3 ms for all Tb and Sc concentrations of all samples. In the first graph in Figure 68 is a layer with small and only Tb doping. The decay curve has quite slow rise time (this introduced the negative factor to the second exponential dependence of related decay component in the equation). This indicates slow and continuous increase in population of $^5D_4$ states. It is likely due to some kind of complex slow energy transfer between 5d and $^5D_3$ and $^5D_4$ levels. This phenomenon does not affect samples with higher Tb concentration (from approx. 0.072 p.f.u.). The decay time values are close to reported for Tb:YAG Czochralski grown single crystals reported in [121] or powders of Tb:GAG [52].

The decay times of all samples as a function of either Tb or Sc concentrations are plotted in Figure 69 a and b respectively. The graph in Figure 69 a consists of two sample series. Both Tb:LuAG and TbSc:LuAG compositions are covered. Decay time variation is very low. Both show decreasing tendencies and both series progression resemble each other. From the graphs in Figure 69 is clear that Sc substitution has only minor effect on the Tb decay kinetics. The Tb^{3+} decay time dependence on Sc concentration for TbSc:LuAG (graph b in Figure 69) samples shown minimal shortening of decay time even for the highest Sc concentrations.

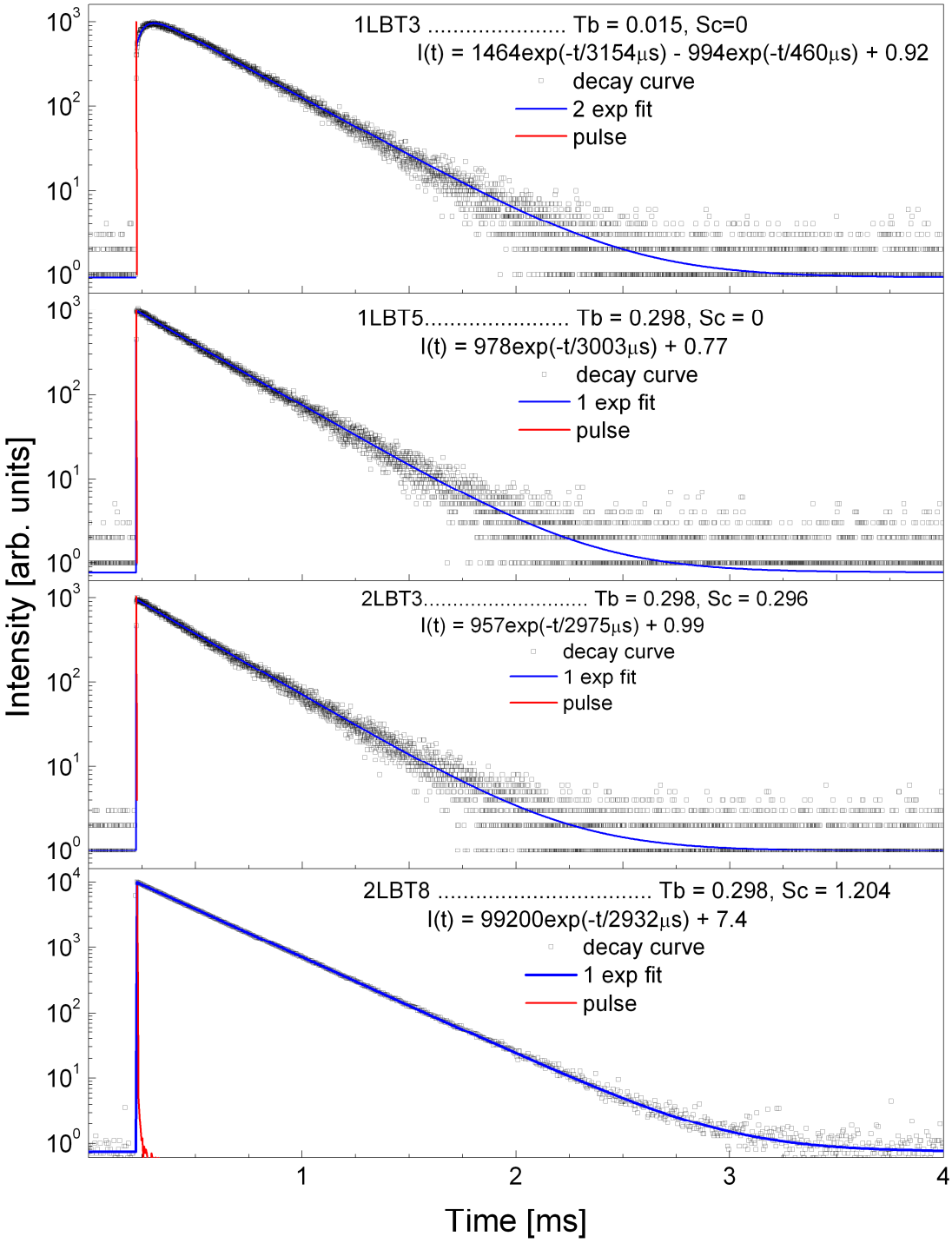

Figure 68: Decay kinetics curves excited in 5d band of Tb ion at λ_{exc} = 270 nm of Tb:LuAG (first two) and TbSc:LuAG (last two) epitaxial layers. Emission collected at 543 nm; (data fitted by reconvolution with apparatus function - measured response function for each spectrum - red pulse), concentrations of Tb and Sc ions are noted in the legend in p.f.u. (for further details see [123])

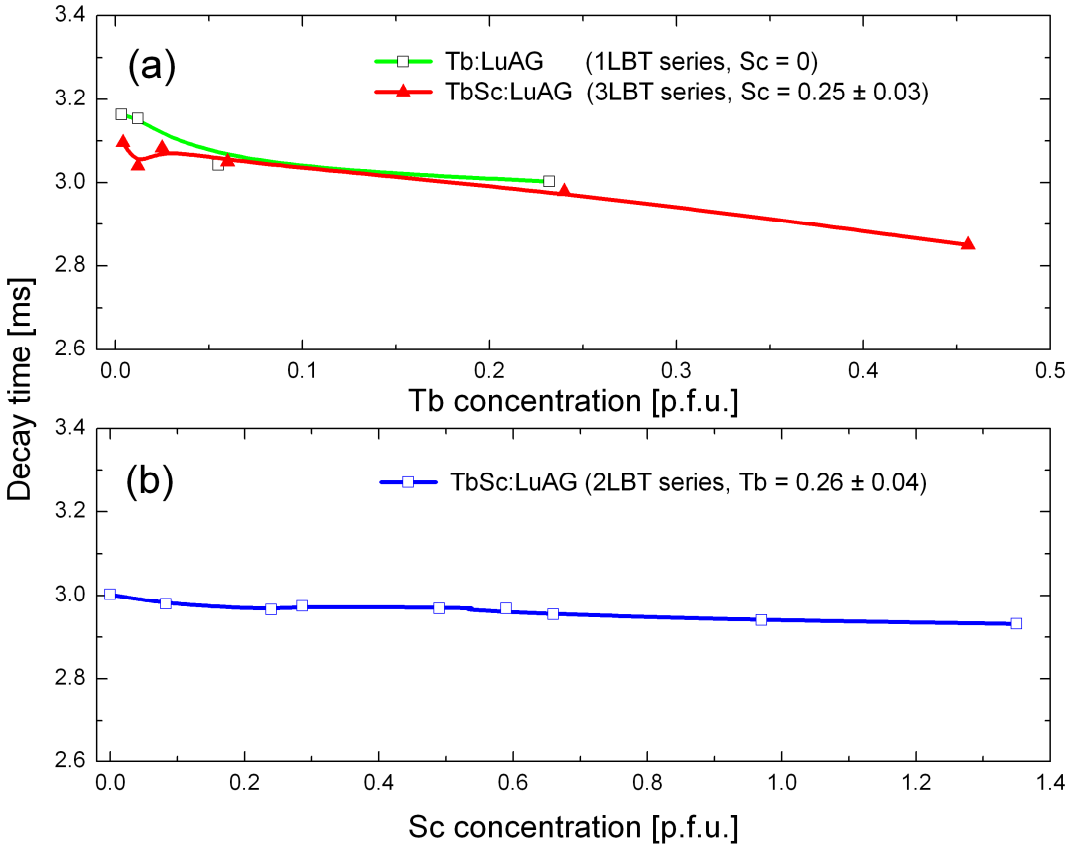

Figure 69: PL decay times of Tb^{3+} at $^5D_4$ emission, λ_{em} = 543 nm and λ_{ex} = 270 nm. The upper curve a) is Tb concentration dependence of decay time for Tb:LuAG and TbSc:LuAG samples of 1LBT and 3LBT series, while the lower curve b) is Sc concentration dependence for TbSc:LuAG samples of 2LBT series, used EPMA measured concentrations for 2 and 3LBT series (concentrations noted in legend are in p.f.u.) (for further details see [123])

5.4.5. Radioluminescence

The RL was measured under X-ray excitation produced by X-ray tube set to 10 kV and 50 mA current. The spectral range was from 200 nm to 670 nm.

The RL spectra in Figure 70 a show reference series of Tb:LuAG with increasing Tb content. Figure 70 b and c depicts the RL spectra of codoped TbSc:LuAG samples. There was either Sc concentration variation, while Tb content was unchanged (Figure 70 b), or Tb content was changed with same Sc content (Figure 70 c). The slits on detection spectrometer were open to 16 nm so the RL spectral resolution was poor. The result was loss of the fine structure in the spectra. The RL intensity of studied samples is clearly much greater compared to the reference BGO crystal.

There is a broad emission band located in the UV region between 250 and 400 nm with a maximum near 300 nm in majority of layers. This was not observed in PL spectra. The band originates from the host lattice defects, since the host lattice

was not excited in the PL. It can originate from antisite defects Lu_{Al} as reported in [6]. There is also a possibility of some unidentified impurities.

From the RL spectra of Tb:LuAG samples with increasing Tb concentration is obvious, that the terbium doping suppresses the host lattice emission. The host contribution is nearly quenched for Tb content above 0.072 p.f.u. From this can be suggested an excitation energy transfer from the host lattice towards Tb^{3+} ions and its consequent release at higher Tb concentrations.

The $^5D_3$ emission is also quenched at higher Tb concentrations much like in the PL due to the cross-relaxation (see Figure 70 a). The effect of increasing Sc content on the RL spectra in codoped TbSc:LuAG samples are shown in Figure 70 b. Even small amount of Sc ions brings back the UV band. It has far lower intensity than in low-doped Tb:LuAG. This new band comes from the Sc related emission center, in other words from radiative recombination of an exciton localized near the Sc ion [125]. This emission intensity is maximal for concentration 0.3 p.f.u. of Sc and higher Sc doping cause decrease in its intensity and increase of the host lattice emission.

The impact of increasing Tb doping on the RL spectra of co-doped TbSc:LuAG samples are shown in Figure 70 c. The concentration of Tb was increased from zero with almost constant Sc content. Sample with no Tb shows a broad UV emission from 250 to 500 nm with maximum at 280 nm (see also previous chapter, 4LBS series). This band originates from recombination of an exciton localized near the Sc ion. The UV emission is gradually quenched with increase of Tb concentration.

The integral intensities of the RL spectra as a function of doping concentration are depicted in the inserted graphs in Figure 70. The black curves represent the integral of whole spectrum (from 200 nm to 650 nm) and the red curves $^5D_4$ emission integral (from 470 nm to 630 nm). The $^5D_3$ transitions represent main contribution in Tb:LuAG samples with low Tb concentration and it is dominant when Tb is at about 0.015 p.f.u. The green $^5D_4$ emission increases its intensity with Tb content, but becomes saturated above 0.07 p.f.u. of Tb (see Figure 70 a). The effect of Sc codoping on the integral RL intensity shows a local maxima at 0.3 p.f.u. of Sc (see Figure 70 b). The integral tends to increase at high Sc doping. This behavior can be explained by reabsorption of part of the UV emission by the Tb^{3+} ions at 270 nm. A dip occurs in the UV band for this wavelength in the RL spectra (see Figure 70 b,c).

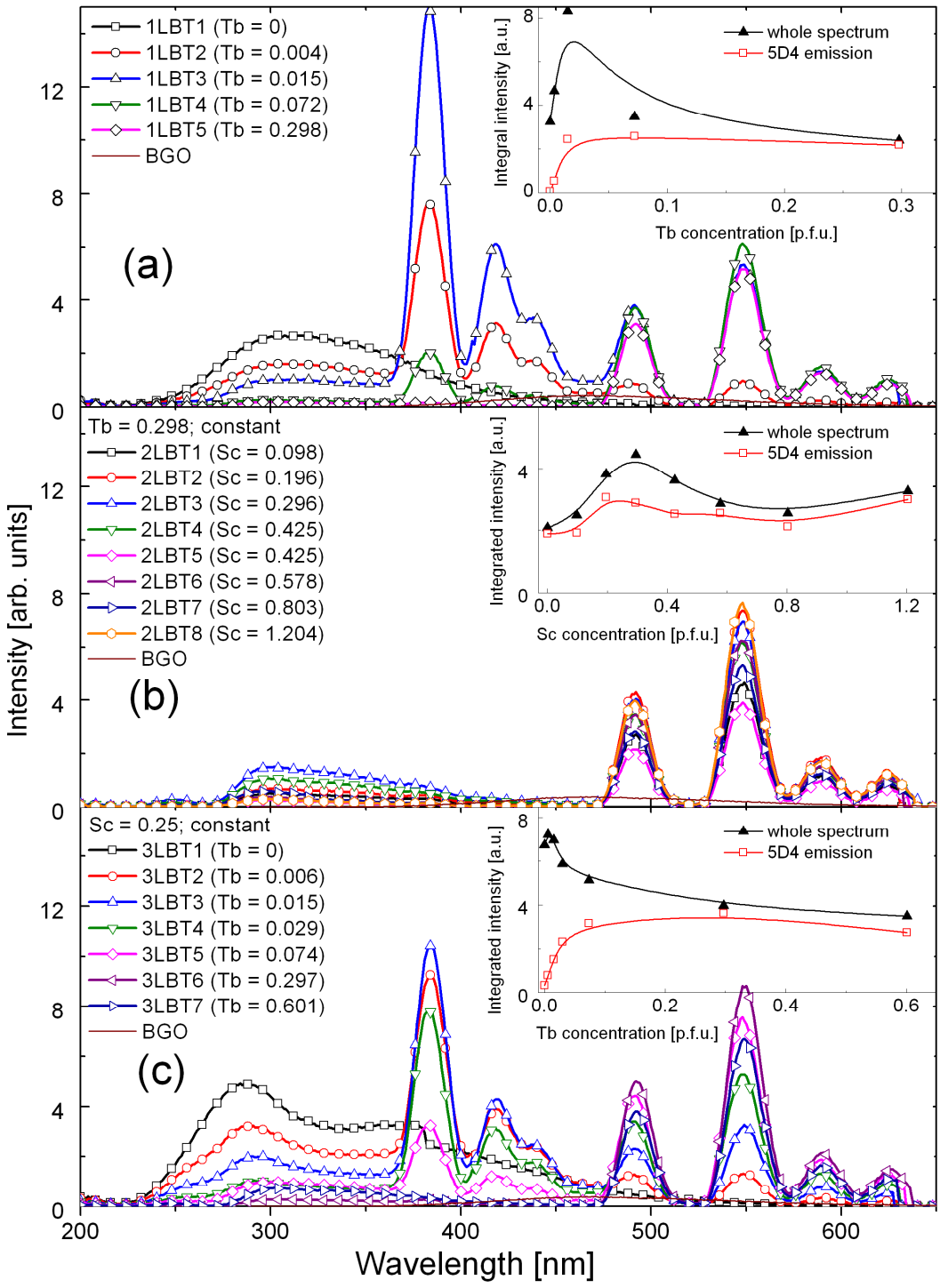

Figure 70: Radioluminescence spectra of a) Tb doped LuAG and b) TbSc codoped LuAG with varying Sc content and constant Tb content and c) TbSc codoped LuAG with varying Tb content and constant Sc content. Concentrations of Tb and Sc are noted in the legend, the reference spectra of BGO crystal plotted for comparison. The inserted spectra are dependencies of integrals RL intensity over the whole spectral range and the $^5D_4$ emission (470 nm – 650 nm) on dopant concentration (noted in legend in p.f.u.); see in [123].

5.4.6. Summary

In this chapter, the growth and characterization of Tb-doped garnet epitaxial films and Sc codoped Tb:LuAG epitaxial layers were performed. Sc doping slightly decrease crystal field splitting of 5d states of Tb ions causing shift of corresponding peaks closer together.

The TbSc:LuAG garnet shows potential for improving the emission using Sc^{3+} codoping. Even high Sc concentrations do not quench PL and RL, instead the integrated RL intensity increases. No apparent loss of energy was observed. The codoped TbSc:LuAG was superior in both PL and RL properties to Tb:LuAG.

The rise and decay time measured at 543 nm peak depends on Tb concentration. The rise time considerably and decay time slightly shortens with Tb content increase. Sc only slightly shortens the luminescence decay time. The host lattice RL emission is quenched with Tb^{3+} doping. The Sc related RL emission in the UV augment Tb green emission via energy transfer.

5.5. Tb:YSO

5.5.1. Sample summary

YSO is great host material for scintillators and scintillator screens. Some parameters are better than in garnets. Presented samples were first try in YSO LPE growth, thus goals of presented work on Tb-doped YSO epitaxial films were optimization of LPE growth technique for YSO material from PbO flux, testing and reasonable improvement of the flux. The BaO flux was also used for growth, but without success. Influence of various doping levels on samples properties was studied. A cross-relaxation phenomenon is observed in Tb:YSO [82], much like in Tb-doped garnets [52].

Summary of prepared samples for this study is listed below. All layers were prepared from PbO-B_2O_3 flux. For evaluation of dopant content in the following tables are used values based on melt composition and estimated from segregation coefficient. The 1S series was grown for the purpose of LPE flux development and conditions optimization. The Tb concentration was low. The composition of melt was substantially changed for 2S series and saturation temperature together with Tb content on temperature dependence was studied. From conducted EPMA analysis mentioned in Table 16 can be deduced, that supercooling temperature plays only little role on Tb content difference. The 4S series was prepared with increasingly high Tb doping concentrations.

Substrates of Ce:YSO were used because of unavailability of pure YSO. Thus a phoswich of Tb:YSO on Ce:YSO was created and studied.

sample	Layer thickness [μm]	substrate	Growth temperature [℃]	x (Tb) [p.f.u.]	EPMA Tb [p.f.u.]
1S series (Tb 1%)					
1S4	2.5	Ce:YSO	959.8	0.016	-
1S5	22.4	Ce:YSO	961	0.016	-
2S series (Tb 2%)					
2S1	9.7	Ce:YSO	959.1	0.032	-
2S2	19.1	Ce:YSO	955.6	0.032	-
2S3	6.0	Ce:YSO	969.3	0.032	0.03172
2S4	41.5	Ce:YSO	969	0.032	-
2S5	10.7	Ce:YSO	983.1	0.032	-
2S6	24.9	Ce:YSO	987.6	0.032	0.03256
2S7	18.0	Ce:YSO	994.7	0.032	0.03176
2S8	14.5	Ce:YSO	975.4	0.032	-
2S9	13.6	Ce:YSO	975.5	0.032	0.0348
4S series (5,10,16%)					
4S1	20*	Ce:YSO	974.6	0.08	-
4S2	15.5	Ce:YSO	979.8	0.16	-
4S3	5.4	Ce:YSO	982.6	0.256	-

Table 16: Table of Tb:YSO – $(Y_{2-x}Tb_x)SiO_5$ samples from $PbO\text{-}B_2O_3$ flux (concentration of Tb was determined from melt content suggesting segregation coefficient $k_{Tb} \sim 0.8$ and is given as atoms per formula unit (p.f.u.); * layer thickness for sample 4S1 estimated based on geometry of the layers as it was not completely submerged)

5.5.2. Absorption

The transmittance was measured in range from 190 to 1100 nm. Calculated optical density spectra of Tb doped YSO in range showing 4f - 5d transitions are shown in Figure 71. The Ce:YSO single crystal was used as a substrate. It was measured too to show its contribution to the absorption of the samples. Its spectra match those mentioned in literature [126]. Any Tb related absorption was not observed in layers, because of the substrate overlap. There remains a clearly distinguished absorption peak after substrate subtraction at 243 nm and increased background absorption below 270 nm. The absorption peak most probably originates from Pb^{2+} ion absorption, discussed in [127]. Transparency varied from sample to sample as the growth conditions were tuned.

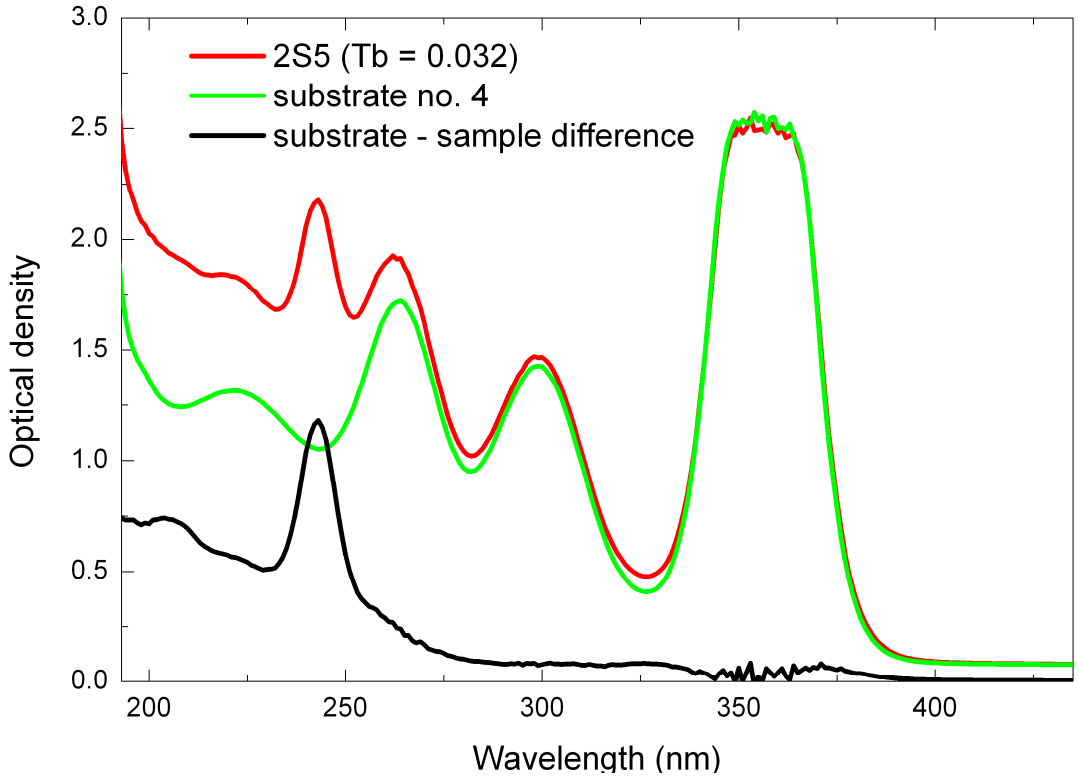

Figure 71: Optical density of Tb:YSO epitaxial layer compared to used Ce:YSO substrate. Concentrations of Tb ions are noted in the legend in p.f.u.

5.5.3. Photoluminescence

The PL emission spectra were measured in range from 300 nm to 700 nm to see both $^5D_3$ and $^5D_4$ transition bands. The excitation wavelength was 272 nm. In Figure 72 are shown samples grown under similar conditions with Tb concentration slightly varied due to different growth temperatures. The Tb content was approximately 0.032 p.f.u. for all depicted samples. Background signal consisting of a broad band that begins at 375 nm and ends before 500 nm comes from PL of Ce^{3+} in Ce:YSO substrate. This background is modulated by structured bands peaking at 385 nm, 413 nm, 434 nm, 456 nm and 484 nm originating from Tb^{3+} ions in layer Tb:YSO. The other band peaks are at 541 nm, 583 nm and 620 nm. The difference in intensity is mainly due to different roughness and concentration variation of each sample. There is also visible a slight fluctuation in ratio between $^5D_3$ (385, 413, 434 and 456 nm) and $^5D_4$ (486, 541, 583 and 620 nm) peaks.

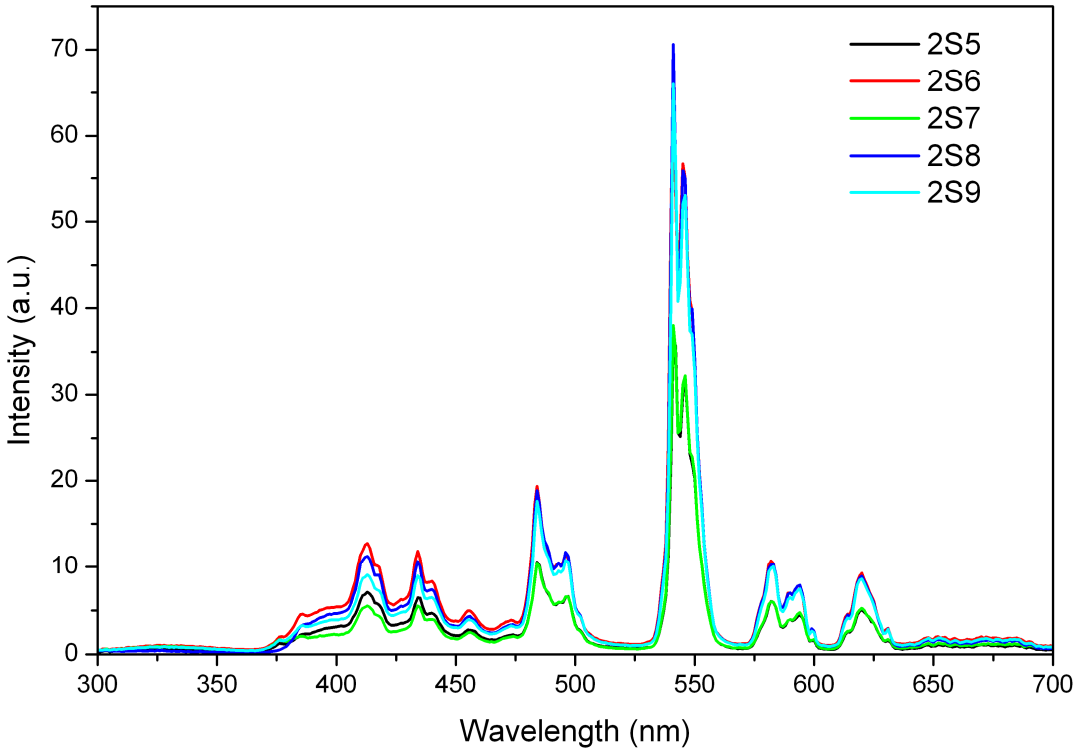

Figure 72: PL emission (λ_{ex} at 272 nm) spectra of equally Tb doped YSO samples. Concentrations of Tb ions in presented layers are roughly 0.032 p.f.u.

In the Figure 73 is shown change in emission spectra induced by Tb concentration increase. The excitation wavelength is also 272 nm. The Tb luminescence at higher doping levels is clearly dominated by $^5D_4$ bands. The Ce:YSO substrate emission is suppressed with higher Tb content along with $^5D_3$ bands. This attenuation is probably connected to strong scattering due to increasingly greater roughness of samples together with increased absorption cross section of Tb^{3+} ions 4f - 5d transitions.

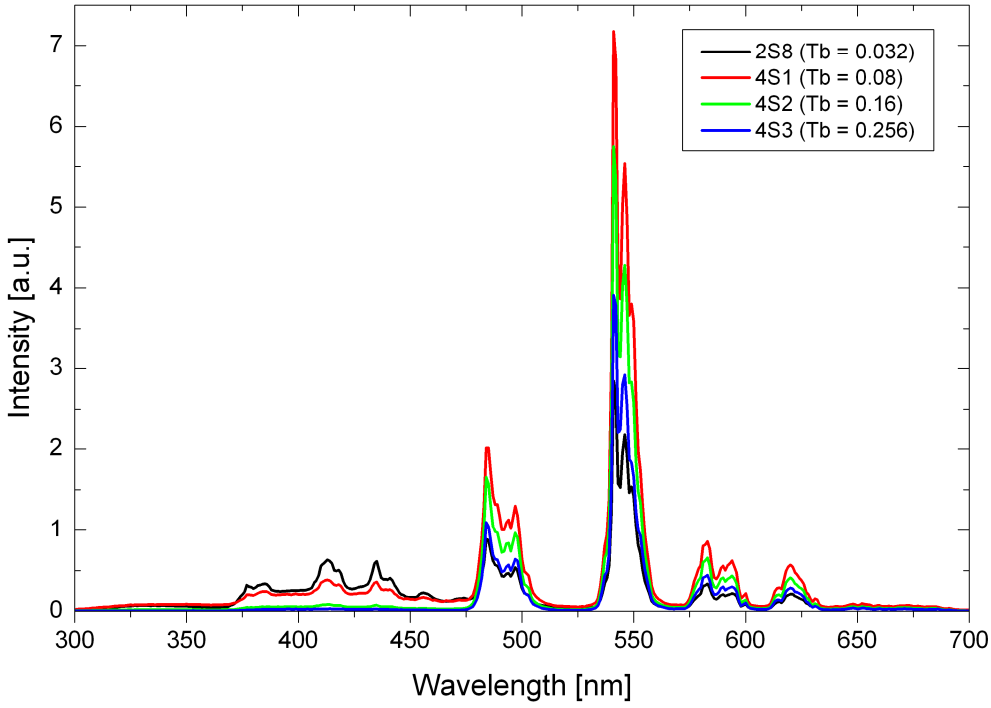

Figure 73: PL emission (λ_{ex} at 272 nm) spectra of Tb doped YSO samples. Concentrations of Tb ions in presented layers are increasing from 0.032 p.f.u. up to 0.256 p.f.u.

5.5.4. Radioluminescence

The RL of the Tb doped YSO samples were measured under X-ray excitation from X-ray tube set at 10 kV and 50 mA current. The spectral range was from 200 nm to 670 nm. Samples were compared to the reference BGO crystal. The RL spectra are shown in Figure 74. Fine structure of peaks was merged together, because the slits on detection spectrometer were open to 16 nm to maximize signal. The RL intensity of measured samples is greater compared to the reference BGO crystal.

The broad band from 360 nm to 521 nm is caused by Ce:YSO substrate and the finer structure originate from Tb luminescence of layers. The strongest emission band is at 546 nm, but its shape is distorted by wide slits. Low and uniform doping is shown in the upper graph in Figure 74. The intensity ratio for band at 546 nm between samples differs from PL equivalent. It is clearly seen in the lower graph in Figure 74 that the $^5D_3$ bands of Tb ions are quenched at higher concentrations. At highest Tb content, the quenching of the $^5D_4$ bands starts. Contrary to the PL spectra, the Ce:YSO band from substrate is strong, forming a peak at 401 nm. This is probably due to low thickness of the layers and high penetration of X-ray excitation causing strong scintillation of substrate. The most intense Tb peak is at 546 nm and strongest Tb RL is achieved at 0.16 p.f.u. concentration. All peaks are slightly shifted compared to Tb:LSO [84]

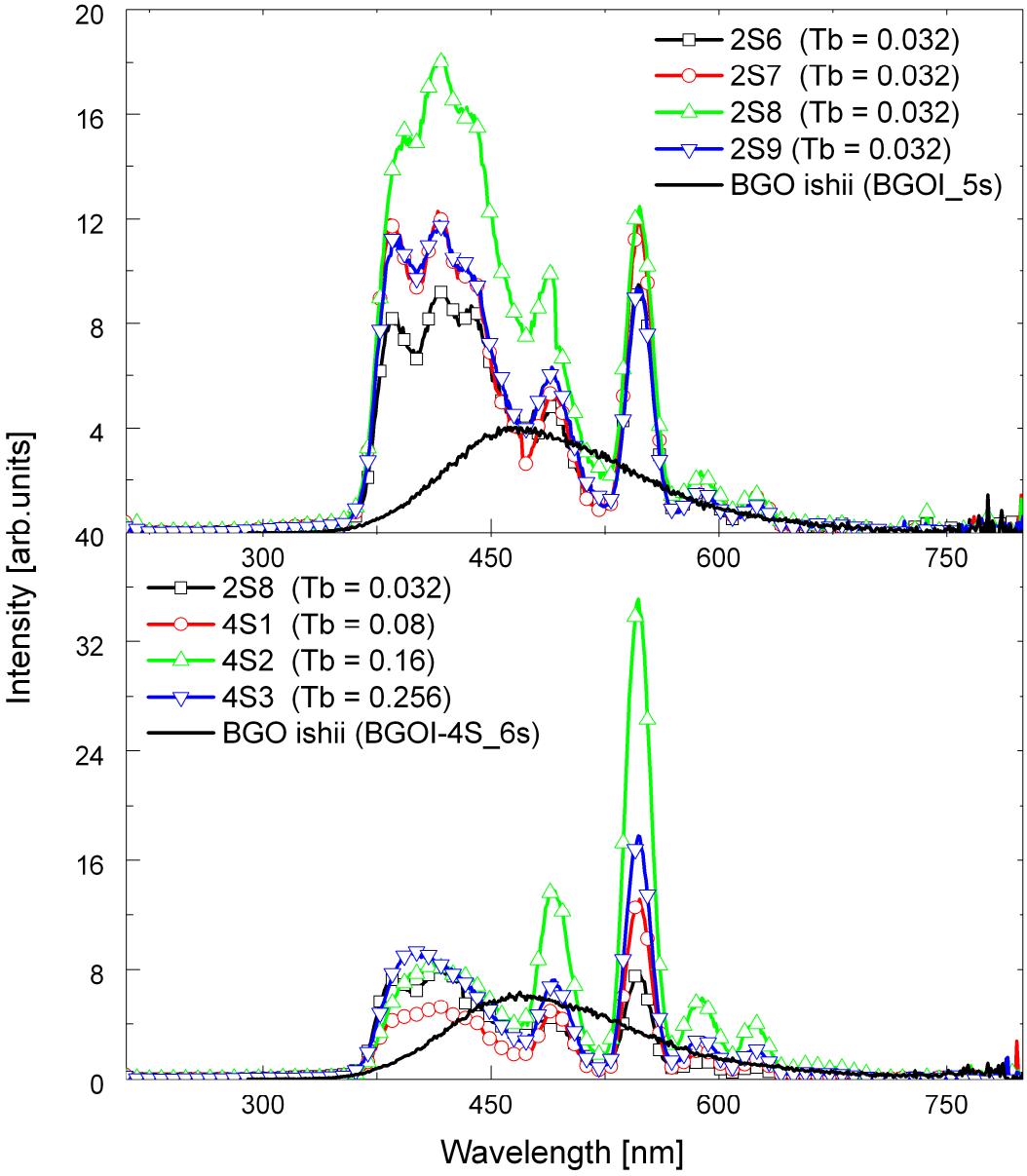

Figure 74: Radioluminescence spectra of Tb doped YSO samples with constant Tb content shown in upper graph and with increasing Tb content in the latter. Concentrations of Tb are noted in the legend in p.f.u., the reference spectra of BGO crystal plotted for comparison.

5.5.5. Summary

This chapter covers the growth and characterization of Tb-doped yttrium oxyorthosilicate epitaxial films. Optimization of LPE growth technique for YSO material from PbO flux was done throughout all series. Measurements were influenced by used substrate of Ce:YSO and by Pb ions from PbO flux. The Tb^{3+} f - f transitions emission is less vulnerable to the Pb ions than 5d – 4f emission of Ce or Pr. The Tb:YSO layers have emission in violet - blue range and also in the range from 475 nm to 650 nm. The emission is separated in bands of sharp line like structures with the most dominant peak at 541 nm. The strongest PL occurs at lower doping, but RL spectra have maxima for higher Tb concentration. The Ce:YSO substrate PL is quenched at high Tb concentrations, the RL has opposite trend. This is probably caused by strong scintillation of substrate due to low thickness of the layers and high penetration depth of X-ray excitation. The surface quality of layers slowly worsened as the Tb concentration increased.

5.6. Ce:YSO

5.6.1. Sample summary

Properties of cerium-doped yttrium oxyorthosilicate single crystal films were studied in this chapter. A summary of prepared samples is shown in Table 17. Goals of presented work were further optimization of LPE growth of YSO from PbO flux, this time for Ce doping, and determination of influence for various doping levels on sample properties. In addition, the influence of growth conditions and codoping by Zr^{4+} ions on samples was studied. The general idea for Zr codoping was to compensate the charge of Pb^{2+} ion impurities. As it can be seen in the results of GDMS analysis in Table 18, the Pb contamination is comparable to the doping level of Ce ions. The inspiration was improvement of characteristics of Ce:YSO (Ce:Y_2SiO_5) by Ca^{2+} and Mg^{2+} codoping used to compensate Ce^{4+} ions which was demonstrated in [78, 81]. Better performance is explained by reduction of shallow traps, which were seen in thermoluminescence. Brief summary of prepared samples for this study is listed below. All were prepared from PbO-B_2O_3 flux. For dopant content in the following table are used values based on melt composition and estimated from segregation coefficient. On first two samples were tested optimal growth conditions and optimal growth temperature was obtained. The samples 1SC3 to 1SC6 were Ce doped YSO layers. Further layers were Ce:YSO codoped with Zr.

sample	Layer thickness [μm]	substrate	Growth temperature [℃]	x (Ce) [p.f.u.]	y (Zr) [p.f.u.]
1SC1	20.0	Ce:YSO	976	0	0
1SC2	23.5	YSO	990	0	0
1SC3	17.5	YSO	989.9	0.0019	0
1SC4	12.7	YSO	995.9	0.0019	0
1SC5	13.7	YSO	989.6	0.0048	0
1SC6	16.1	YSO	994	0.0048	0
1SC7	30.4	YSO	992.6	0.0048	0.0005
1SC8	24.7	YSO	993	0.0048	0.0022
1SC9	21.8	YSO	993.1	0.0048	0.0061
1SC10	12.8	Ce:YSO	986	0.01	0.0058
1SC11	17.4	YSO	994.3	0.01	0.0058
1SC12	8.7	YSO	985.1	0.01	0.0058
1SC13	14.2	YSO	985.4	0.0152	0.0053
1SC14	11.1	YSO	993.5	0.0152	0.0053
1SC15	24.6	YSO	993.4	0.0152	0.0104

Table 17: Table of Ce:YSO – $(Y_{2-x-y}Ce_xZr_y)SiO_5$ samples from PbO-B_2O_3 flux (concentrations of Ce and Zr were determined from melt content suggesting segregation coefficient $k_{Ce} \sim 0.01$ and $k_{Zr} \sim 1$ and is given as atoms per formula unit (p.f.u.)

	O [p.f.u.]	Si [p.f.u.]	Y [p.f.u.]	Pb x 10^3 [p.f.u.]
1SC2	5.06	1.12	1.88	0.88

	O [p.f.u.]	Si [p.f.u.]	Y [p.f.u.]	Ce x 10^3 [p.f.u.]	Pb x 10^3 [p.f.u.]
1SC3	5.05	1.12	1.88	1.58	1.90
1SC4	5.06	1.12	1.88	1.15	0.53
1SC5	5.05	1.12	1.87	3.21	1.49
1SC6	5.05	1.12	1.88	2.46	1.21
1SC7	5.05	1.12	1.88	3.07	1.70
1SC8	5.05	1.12	1.87	2.21	1.68
1SC9	5.06	1.13	1.87	3.05	1.73

Table 18: Table of content analysis for selected Ce:YSO – $(Y_{2-x-y}Ce_xZr_y)SiO_5$ samples, the concentrations are given as atoms per formula unit (p.f.u.); (GDMS analysis, the samples 1SC7-9 contained Zr, but no data about its content were received)

5.6.2. Absorption

The transmittance was measured in range from 190 to 1100 nm. Calculated absorption coefficient and optical density spectra of Ce doped YSO samples in range showing 4f - 5d transitions are shown in Figure 75. The Ce:YSO single crystal was measured for reference. Its spectra match those mentioned in literature [126]. The Ce:YSO was also used as a substrate for sample 1SC1 and 10. Both were test samples for optimization of the growth conditions. The 1SC1 and 2 samples were prepared as pure, undoped YSO. In the inserted graph in the Figure 75 are shown optical density spectra. The surface roughness greatly influences the measurement. It can be seen in the Figure 75 from comparison of calculated absorption coefficient that was corrected for scattered light and the optical density. The more the surface is rough, the less accurate the absorption contribution determination can be. Beginning with 1SC5, the diffraction began to have severe influence. In the spectra are present peaks that originate from used YSO substrate, namely at 208 nm, 246 nm and 259 nm. The absorption coefficient peak at 356 nm in spectra originates from 4f – 5d transition of Ce^{3+}. This peak in samples 1SC6 to 9 indicates roughly equal amount Ce content and it is comparable to the single crystal. Heavy absorption in the UV below 350 nm is probably caused by the presence of Ce^{4+} [78, 128] and charge transfer transition between 2p state of O^{2-} and 4f state of Ce^{4+}. The Ce^{4+} is created as consequence of charge compensation of Pb^{2+} ions.

We also performed annealing as reported in [78-80]. Selected samples were annealed twice in air at 1100°C in order to either decrease volatile Pb ion content and then twice at 650°C in H_2 to reduce the oxidation state of doping ions. The change in absorption was measured after each annealing. The optical density of sample 1SC7 after complete processing is compared to initial after-growth in Figure 76. The difference after each step was negligible as well as between the initial and completely processed stage. The valence of Ce centers was not influenced.

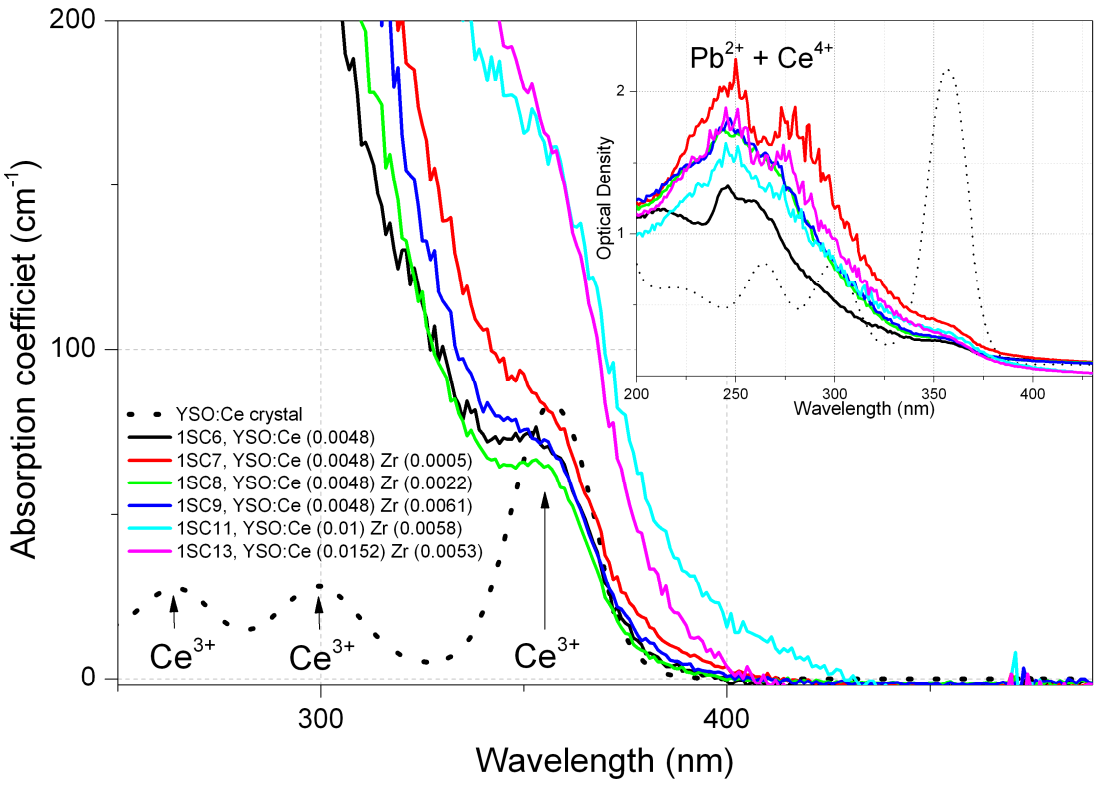

Figure 75: Absorption coefficient and Optical density (inset graph) of Ce:YSO and CeZr:YSO epitaxial layers with Ce:YSO substrate for comparison. Concentrations of Ce and Zr ions are noted in the legend in p.f.u.

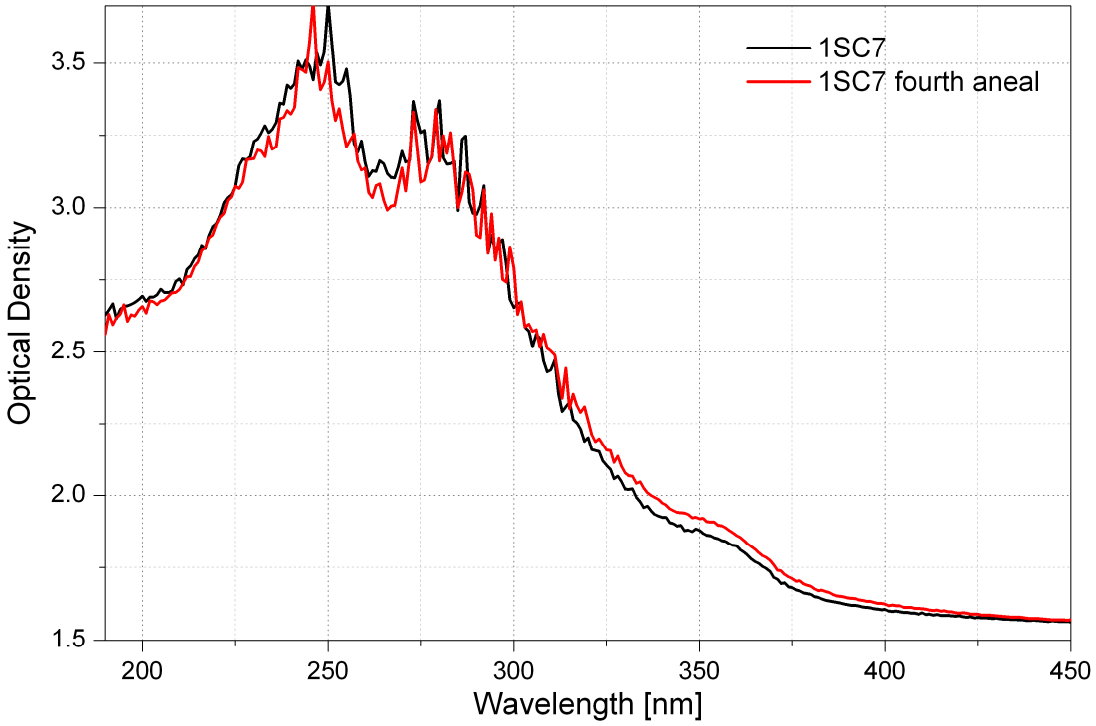

Figure 76: Optical density change of CeZr:YSO epitaxial layer after repeated annealing process, see text for details

5.6.3. Photoluminescence

The PL excitation and emission spectra of the samples were measured in the spectral range 200 to 850 nm. There are two sites available for Ce ions to occupy, as it is mentioned above in chapter 3.2. Measured PL spectra of both centers are shown in Figure 77. They were selectively excited with wavelengths chosen to maximize the separation of contribution from other site. The emission for the Ce1 site was collected at 390 nm, and corresponding excitation peaks are at 263 nm, 300 nm and 358 nm. This site has emission peak at 410 nm when excited at 300 nm. Emission for the Ce2 site was collected at 500 nm, and the corresponding excitation peaks are at 264 nm and 364 nm. The site has emission peak at 442 nm when excited at 325 nm

Comparison to the spectra of Ce:YSO single crystals shown in literature [126, 129] exhibit some major differences. The single crystal excitation spectrum for Ce1 at λ_{em} 390 nm has a parasitic peak superimposed on the 358 nm peak (see the inset graph b in Figure 77). It was not observed in the layers. The single crystal excitation spectrum for Ce2 at λ_{em} 500 nm has much more intense peaks at 324 nm and 372 nm. Finally, the emission spectra for both Ce1 and Ce2 sites have different shape.

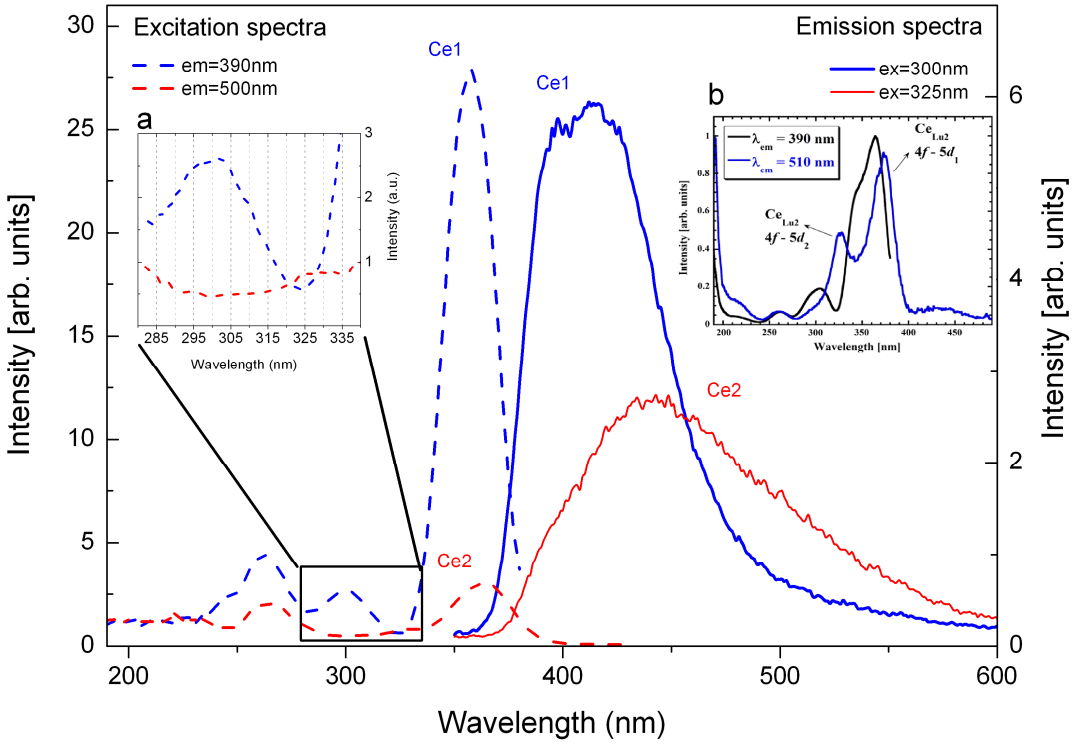

Figure 77: Excitation and emission spectra of the Ce ions at emission wavelengths for both Ce1 and Ce2 sites in CeZr codoped YSO sample 1SC8 (Ce content 0,0048 and Zr 0,0022 p.f.u.); the inset graph a is a close look on an overlap of Ce1 and Ce2 site excitation spectra; the inset graph b shows overlap in a single crystal Ce:YSO, cited from work of Jarý [129]

Epitaxial layers of Ce:YSO were also prepared by Zorenko [127, 130-137]. They were prepared from PbO melt like our samples, but no PL observation was mentioned. From PL spectra shown in Figure 78 is evident a strong negative influence of Pb ions on PL intensity. Samples grown at higher temperature (1SC4,6) have significantly stronger PL despite lower Ce content when compared to their counterparts. The 1SC3 and 5 were grown from the same melt at lower temperature. It was shown in chapter 5.1 that with decreasing growth temperature, the Pb content significantly increases. The Ce^{4+} is created instead of Ce^{3+} as consequence of increased Pb^{2+} concentration and causes observed PL quenching.

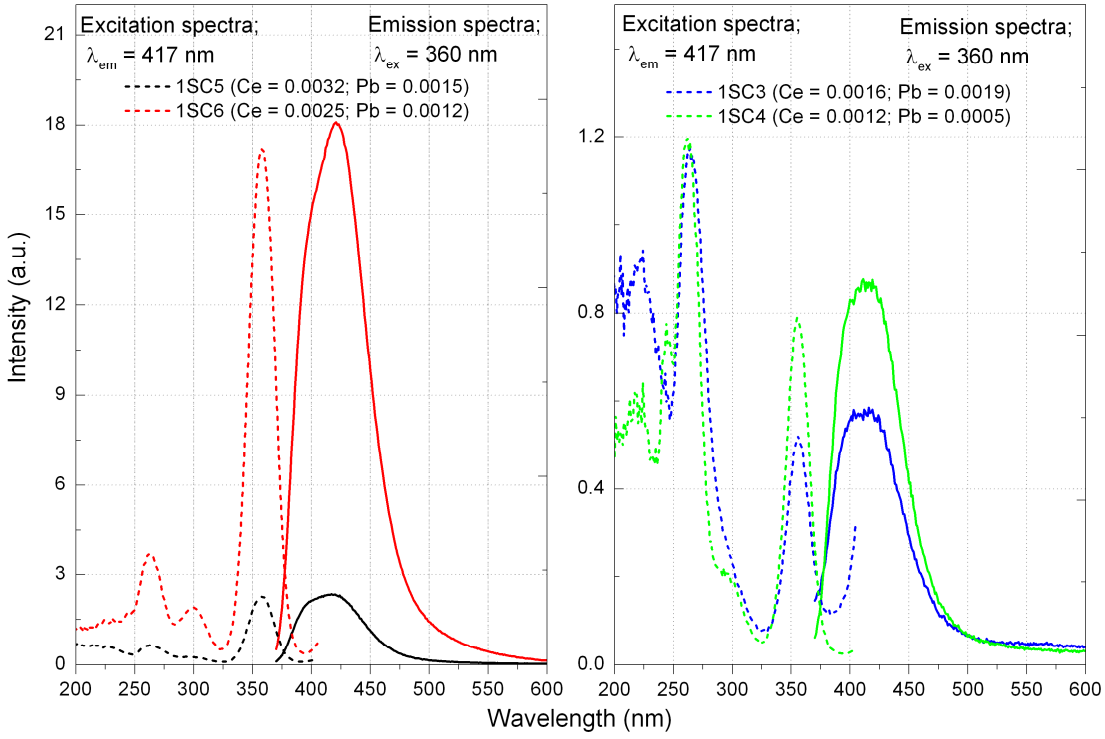

Figure 78: Comparison of emission (λ_{ex} = 360 nm, full lines) and excitation (λ_{em} = 417 nm, dashed lines) spectra of Ce:YSO epitaxial layers in respect to Pb^{2+} content; concentrations based on EPMA analysis noted in legends are in p.f.u.

In the inset a in Figure 77 is shown a detail of Ce1 and Ce2 excitation spectra with peak of Ce2 at 325 nm which do not coincide with any of Ce1 peaks. As it was described in previous paragraph, these were used in further measurements shown in Figure 79 and Figure 80 to distinguish the influence of Zr codoping on the emission of Ce ions. Chosen samples contained, based on EPMA analysis, approximately same concentration of Ce and Pb ions. The emission spectra evolution in the proximity of the Ce2 peak in Ce:YSO and CeZr:YSO epitaxial layers are compared in Figure 79. Showed spectra are normalized to maxima of emission excited at 335 nm. Each spectrum in Figure 80 is normalized to its maximum. There is no sign

of change in curve shape due to Zr doping in viewed interval, where the influence on PL from both centers inverts (see the inset graph a in Figure 77).

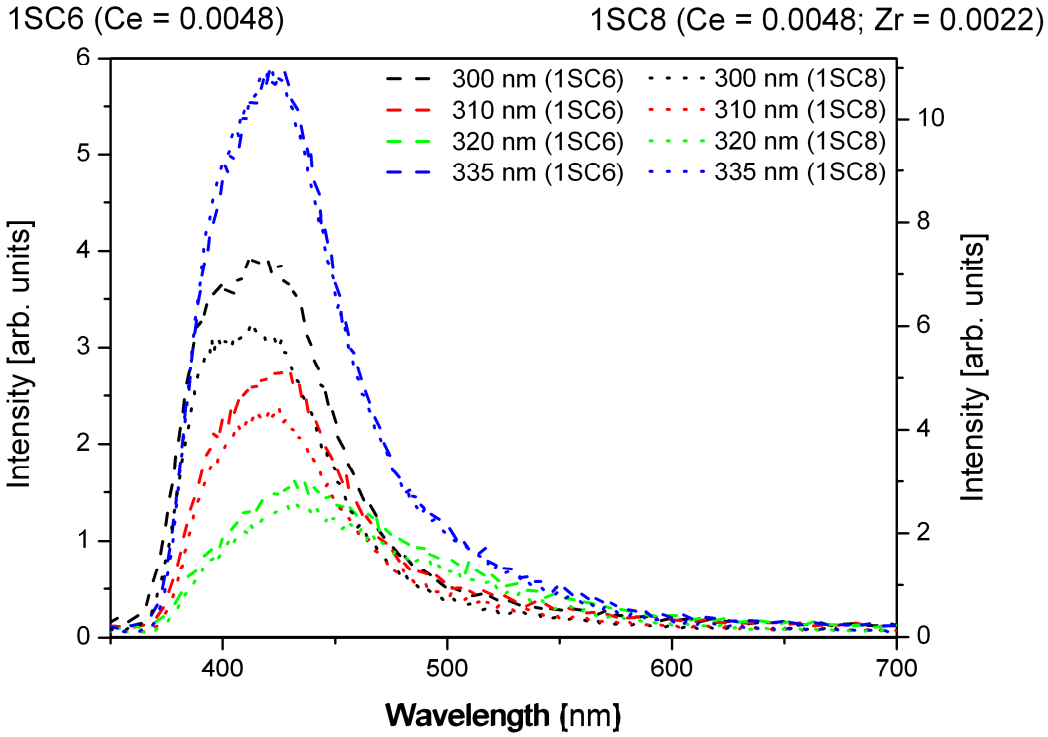

Figure 79: Comparison of emission spectra evolution of Ce:YSO to CeZr:YSO epitaxial layer, normalized to maxima of emission spectra excited at 335 nm.

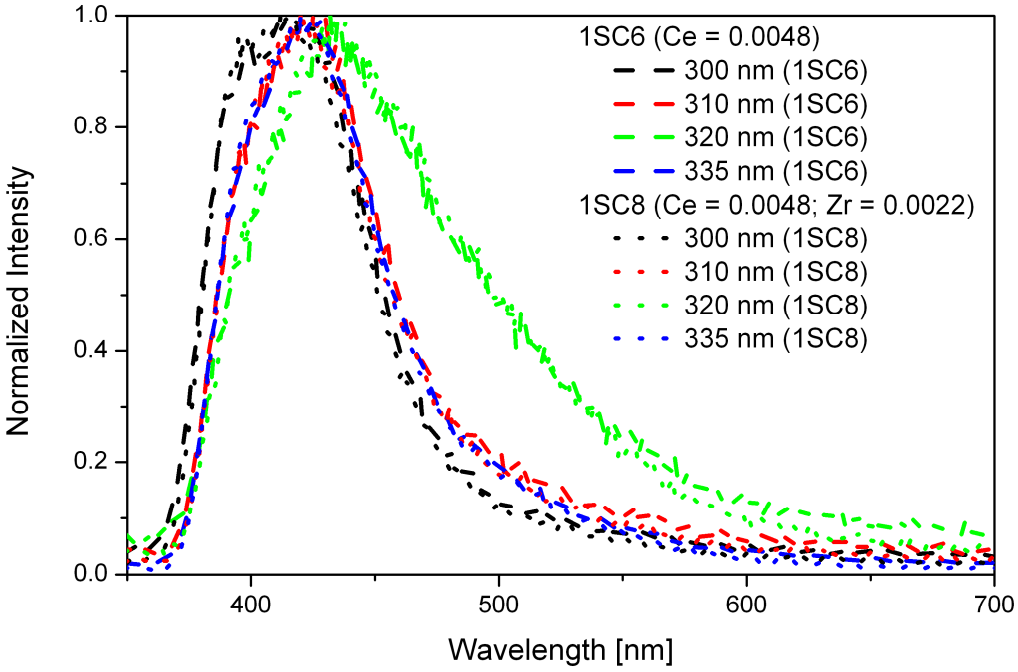

Figure 80: Comparison of emission spectra evolution of Ce:YSO to CeZr:YSO epitaxial layer, normalized to maxima of each emission spectra

The change in PL induced by annealing was also studied. The PL intensity difference was well within the measurement error. Normalized excitation and emission spectra for Ce1 site of unannealed, in air annealed and twice in air and in hydrogen-annealed sample 1SC7 are shown in Figure 81. Only the peak at 300 nm is slightly intensified after first annealing but then decreases again. Like in absorption spectra shown in Figure 76, the spectral change is quite insignificant.

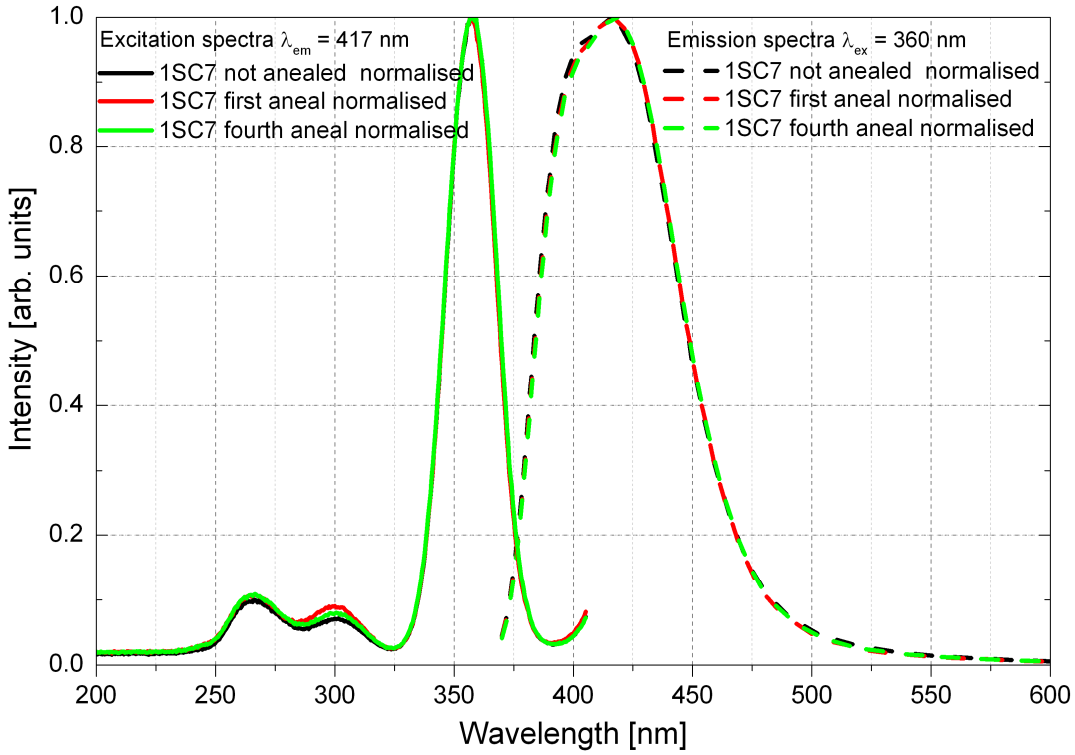

Figure 81: Changes in CeZr:YSO epitaxial layer after repeated annealing process (for Ce1 site)

The change in PL caused by lower Zr doping is shown in Figure 82. Emission spectra of Ce:YSO and CeZr:YSO samples were measured for Ce1 site at 360 nm excitation. Very small Zr doping decreases the PL intensity (1SC7). However, with Zr concentration increase, the PL is doubled. Best performance shows sample 1SC8, with 0.0022 p.f.u. of Zr and 0.0048 p.f.u. of Ce and its excitation spectra were measured over a wide range (see the inset graph in Figure 82). Further increase of Zr content has negative effect on the PL intensity.

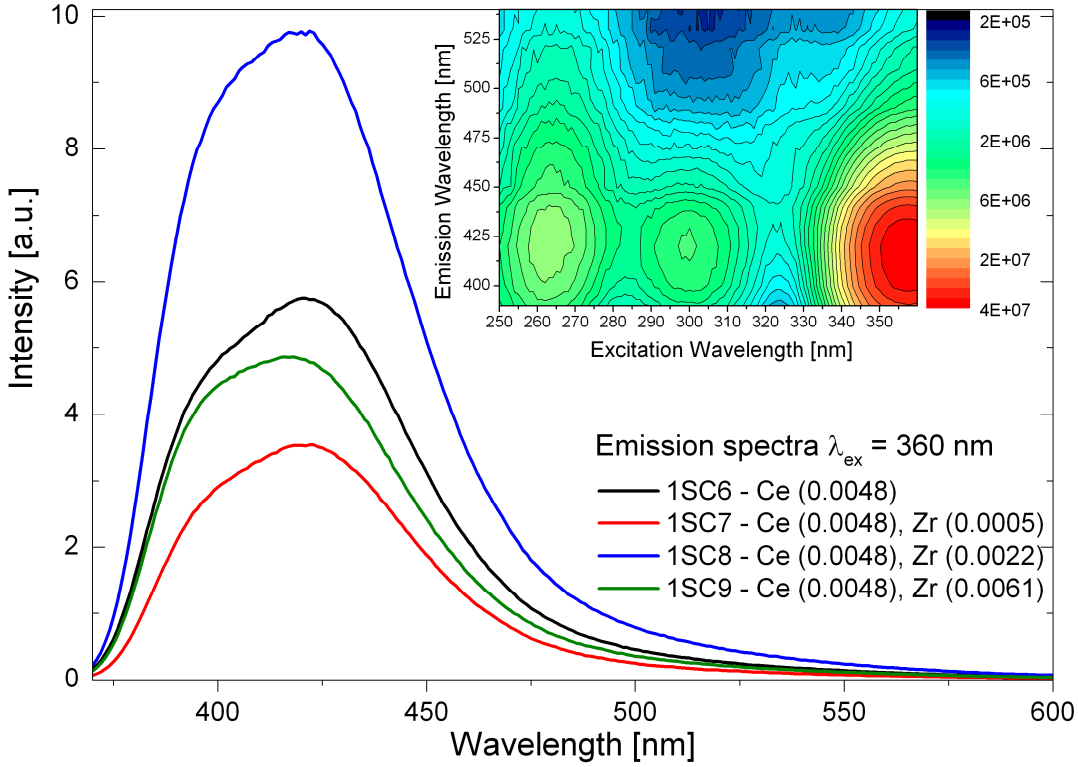

Figure 82: Influence of lower Zr codoping on Ce:YSO epitaxial layers PL; The inset graph is a 3D representation of 1SC8 sample excitation spectra evolution in the range of λ_{em} 410 – 540 nm, the z axis (intensity) is in logarithmic scale

The change in PL caused by higher Zr doping is shown in Figure 83. Excitation and emission spectra of CeZr:YSO samples were measured for Ce1 site. The excitation spectra were measured at emission wavelength 390 nm, the emission spectra at excitation wavelength 300 nm. High concentration of Zr with combination of high Ce content causes deformation of emission spectra and considerable decrease in PL intensity. The 396 nm peak is steadily suppressed by a peak that shifts its maxima from 420 nm to 435 nm. If the Zr concentration is high enough, the PL peak at 435 nm becomes dominant.

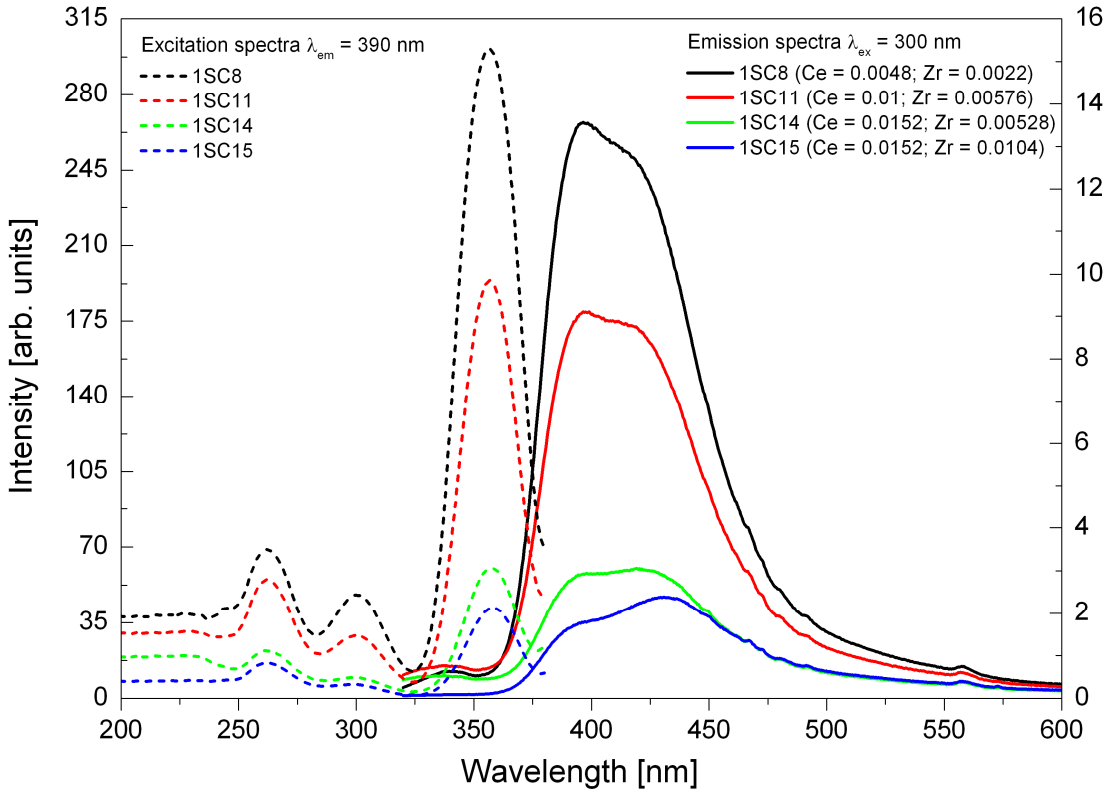

Figure 83: Influence of higher Zr concentrations on CeZr:YSO epitaxial layers PL

5.6.4. Decay kinetics

The decay kinetics for both specific Ce sites was measured in order to obtain more information. The measured data and fitted decay curves are shown in Figure 84. The samples were excited at 362 and 325 nm absorption bands and 5d emission of selected Ce site was collected at 417 nm and 500 nm respectively. The reconvolution fit of the decay curves enabled the determination of decay times in the PL. There are two components for each Ce site present.

The calculated decay times for the Ce1 site consisted of slow component ranging from 32 (1SC4) to 63 ns (1SC8) and fast component ranging from 18 (1SC5) to 25 ns (1SC8) (see the upper graph at Figure 84). The slow one represented up to 30 % from total intensity. No slow component was observed in the samples 1SC3 and 4 and from PL and also RL spectra in Figure 78 and Figure 85 respectively can be seen dominance of 396 nm peak. The peak at 425 nm becomes dominant with increasing Ce concentration (1SC5, 6) and a longer component emerges. The slow component has maximal presence after admixing of Zr in 1SC7. The strongest PL (Figure 82) and RL (Figure 85) is in 1SC8. It has slow component creating only less

than 10 % of total intensity. The slow component is raising again in higher Zr doped samples.

The calculated decay times for the Ce2 site consisted of slow component ranging from 48 (1SC8) to 51 ns (1SC6) and fast component ranging from 12 (1SC6) to 16 ns (1SC8) (see the lower graph in Figure 84). The fast component represented roughly 40 % from total intensity and the ratio did not vary much.

These results are partially in agreement with literature [75, 138], where the observed scintillation decay times were 37 ns for fast component and 82 ns for slow component in Ce:YSO single crystals. But observed PL decay times in [138] for individual Ce centers were 39 ns for Ce1 and 59 ns for Ce2. That is not a big difference from [129], where 34 ns for Ce1 and 55 ns for Ce2 is reported. All PL decays for single crystals found in literature were single exponential. In [133] is reported 16 ns decay time for epitaxial grown Ce:YSO films excited by synchrotron radiation at RT, but the PL was significantly quenched due to Pb^{2+}.

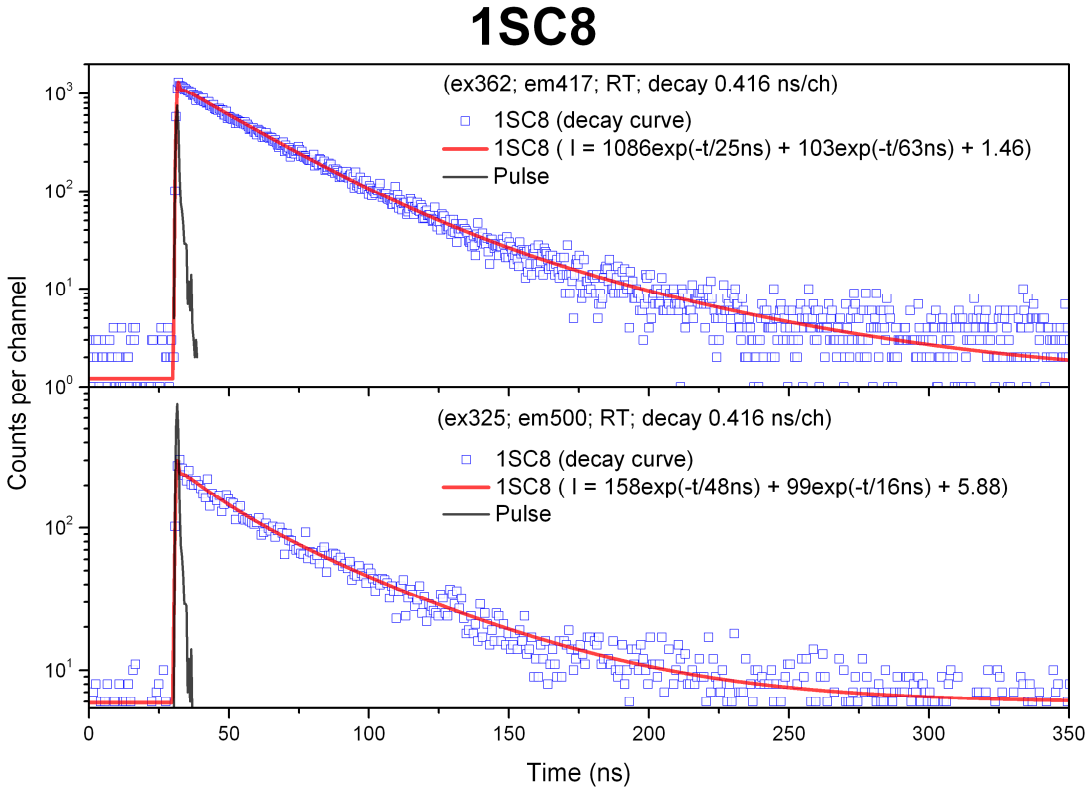

Figure 84: Decay kinetics curves of Ce:YSO epitaxial layers measured for Ce1 site emission on upper graph, λ_{em} = 417 nm and λ_{exc} = 362 nm and for Ce2 site emission on the lower graph, λ_{em} = 500 nm and λ_{exc} = 325 nm. The solid red line is a reconvolution fit of the measured data with the pulse curve representing the instrumental response

5.6.5. Radioluminescence

The RL of the Ce:YSO series was measured under X-ray excitation from X-ray tube set at 10 kV and 50 mA current. The spectral range was from 200 nm to 800 nm. The BGO crystal was measured as reference. The RL spectra are shown in the left graph in Figure 85. The sample 1SC2, pure YSO layer, has negligible intrinsic RL compared to BGO reference. The samples with purely Ce doping (1SC3 vs. 1SC4 and 1SC5 vs. 1SC6) prove, that the RL of Ce:YSO layers is significantly influenced by growth temperature (Pb^{2+} content). Samples grown at higher temperature (closer to the saturation temperature) have stronger RL intensity. The difference of samples 1SC5 and 1SC6 in their RL is not as great as it was in PL (for comparison see Figure 78). There are two peaks, at 396 nm and at 425 nm. The structure is close to what was observed in Ce:LYSO in [129] close to RT (see in the inset graph in Figure 85). The structure of RL is observed and explained in [138] on analogous material GSO as a weighted combination of Ce1 and Ce2 site emission contributions. The Ce1 at shorter wavelength dominates as the temperature increases to RT.

The 396 nm peak is dominant at lower Ce concentration, but both peaks are nearly equal at higher concentrations, or with the 425 nm peak dominance. The Zr codoping can increase the RL intensity as is shown in sample 1SC8 with 0.0022 p.f.u. of Zr. This sample has roughly 8 percent increase in intensity integral over the 1SC6, which has same concentration of Ce. Higher concentrations quickly quench the RL. The trend is similar to what was observed in PL spectra in Figure 82. Overall, the RL of codoped CeZr:YSO was 6 to 10 times greater than of the reference BGO crystal.

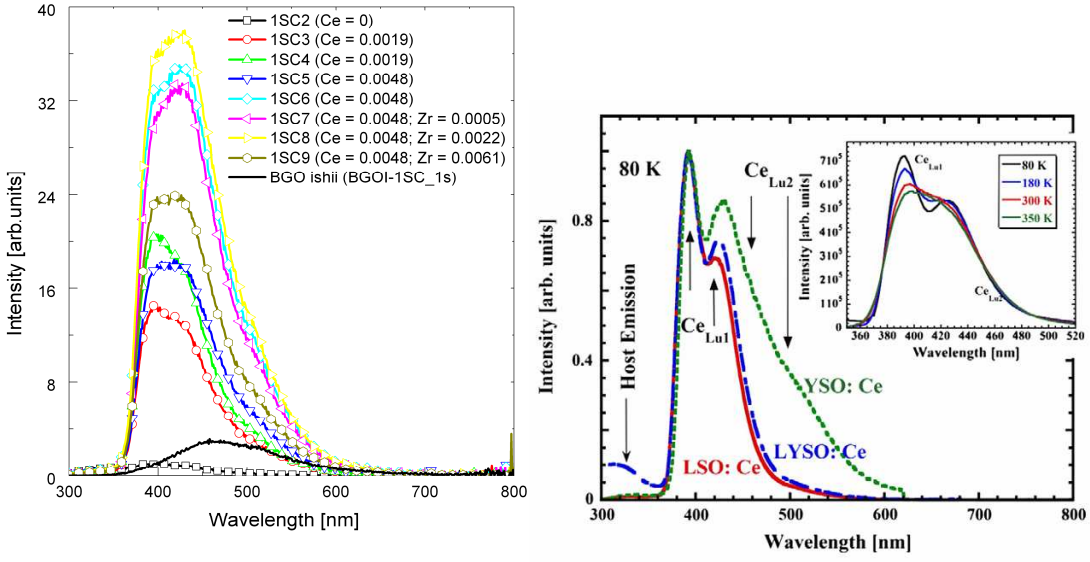

Figure 85: In the left graph is the radioluminescence of CeZr:YSO epitaxial layers in comparison to pure YSO and Ce:YSO layers. Concentrations of Ce and Zr are noted in the legend in p.f.u.; The right graph is a comparison of normalized RL spectra of Ce doped LSO, transitioning LYSO and YSO at cryo temperature (80 K) with inset graph of Ce:LYSO sample at various temperatures, X-ray tube at 40 kV and 15 mA (cited from [129])

5.6.6. Scintillation properties

Scintillation photoelectron yield of Ce:YSO epitaxial layers were studied under alpha particle excitation. Photoelectron yield measurements of samples with best observed overall performance are shown in Figure 86. The photoelectron yield per MeV is in the left graph marked a. There is no increasing trend and it is independent on the shaping time. The scintillation response and all its components are too fast, so the signal is saturated even at the shaping time of 0.5 μs. The signal is quite weak, so the signal to noise ratio is reduced. It can be seen in the graph b that the fluctuation amplitude is less than 1 %, thus close to the measuring device limits.

Comparison of the samples to the Ce:YSO single crystal supplied by CRYTUR shows that the best layers (1SC6 and 8) reach only 65 % of single crystal photoelectron yield measured at 1 μs. It is caused likely by negative impact of Pb^{2+} ions.

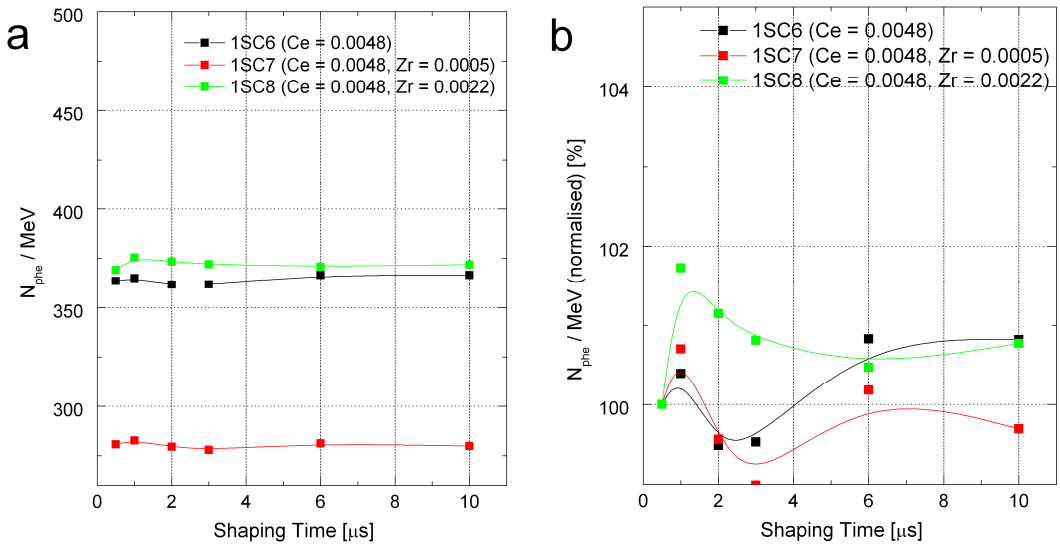

Figure 86: a - Photoelectron yield N_{phe} per MeV as a function of shaping time under alpha particle excitation (source ^{239}Pu) of YSO epitaxial layers doped with Ce and codoped with Zr (concentrations in p.f.u. are noted in the legend); b - Normalized photoelectron yield to the shortest shaping time of 0.5 ms for the same samples.

5.6.7. Summary

In this chapter are presented the results of the Ce-doped yttrium oxyorthosilicate and Zr codoped Ce:YSO layers growth and characterization experiments. The Ce:YSO have strong 5d – 4f UV-blue emission of Ce^{3+} ranging from 370 to 500 nm. Absorption measurements were badly influenced by scattering on the layers and Pb ions causing enhanced absorption in the UV region. Potential improvement by annealing in oxygen or hydrogen was not observed.

PL spectra showed some small differences in peak proportions between our samples and CZ grown single crystals. This is the first time a PL in epitaxial film of Ce:YSO was reported (in literature [131, 133, 135] was PL quenched). Existence of two different Ce centers (Ce1 and Ce2) was confirmed. For optimal Zr and Ce codoping, the PL, RL and the decay time improved. No slow components were observed in photoelectron yield. Too high concentrations of both Ce and Zr lead to quenching of luminescence and enlarging of 435 nm peak in PL and RL spectra. In RL plays key role Pb ions concentration. The higher and closer to the saturation temperature the growth temperature is, the lower Pb^{2+} concentration is and the stronger the intensity of RL is.

The LPE technology was optimized in order to reduce Pb^{2+} content in the layers. The surface quality of layers deteriorated as the Ce concentration increased and best results were obtained close to saturation temperature.

6. Conclusion

The Ce:LuAG layers grown from the PbO flux are easier to prepare with superior crystallographic and surface properties compared to the BaO grown. The Ce concentration can be controlled by adjusting growth conditions. It can be increased with higher supercooling and decreased with higher growth temperature. High concentration of Ce is necessary in the melt due to low segregation coefficient of Ce. Crucial problem of PbO-based flux is the contamination by Pb and Pt ions. These ions cause absorption in the UV range, are the source of nonradiative energy transfer from Ce ions and create trapping states. There is no evidence of Pb^{2+} ion impurities in PL spectra, but PL decay time is shortened up to approximately 35 ns for Ce^{3+} doped garnets together with emerging of a longer component. It means nonradiative loss of excitation energy. The Ce:LuAG films grown from the BaO flux have higher purity than the PbO flux grown. No energy transfer or quenching of luminescence was observed. Layers exhibit high light yield and single exponential Ce decay. High Ce concentration in the layers can be easily achieved in the BaO flux thanks to higher segregation coefficient of Ce. Problem with the BaO flux is complicated film growth caused by very high viscosity and great surface tension of the BaO flux. For the BaO flux grown samples, worse surface morphology of layers is common. Measured PL and scintillation properties are comparable to CZ grown single crystals.

The PrSc:LuAG epitaxial layers with optimized concentrations of Sc and Pr ions and grown from the $BaO–B_2O_3–BaF_2$ flux have radioluminescence and scintillation properties on par with the Czochralski grown single crystals. Samples with Sc concentration in range from 0.24 to 0.575 p.f.u. had 60 – 80 % higher integral radioluminescence compared to the samples without Sc codoping. This is thanks to the combined contribution of Sc and Pr ions in the RL spectra. An energy transfer from Sc^{3+} to Pr^{3+} ions was proven to occur. On the other hand, higher Sc concentrations (more than 0.575 p.f.u.) proved to have opposing effect. Both the PL and RL intensities are reduced and emission is being quenched in highly Sc codoped samples. PL decay time of 5d – 4f transition of Pr^{3+} ions was approximately 18 ns. It was independent of Sc content. The best alpha particle excited photoelectron yield was obtained for low Sc concentration, 0.12 p.f.u. Very desirable effect of Sc codoping was suppression of slow components in favor of the fast components. The fast components have notably higher ratio in such layers when compared to the Czochralski grown crystals. However, the photoelectron yield decreases with high Sc concentrations much like the PL and RL. The slow components also increase, and energy resolution worsen. The Ce codoping decreases performance of PrSc:LuAG layers and quenches Pr emission.

The CePr:GdYAG layers were prepared as a perspective phosphor for white LEDs. The Gd and Pr doping cause red shift of Ce emission and peak at 608 nm

respectively. The purpose is the color gamut of the warm white light replica. A drawback represents strong sensitivity of output light color to viewing angle in as-grown layers. This can be improved by increase of surface roughness, but the cost will be a creation of scattered light.

The TbSc:LuAG garnet shows potential for improving the emission using Sc^{3+} codoping. Sc does not quench 4f - 4f emission in PL and RL and it increases the integrated RL intensity. No apparent loss of energy was observed up to relatively high Sc content of 1.2 p.f.u. The codoped TbSc:LuAG was superior in both PL and RL properties to Tb:LuAG. Sc has minor effect on kinetics of luminescence. The host lattice RL emission is quenched with Tb^{3+} doping. The Sc related RL emission in the UV augment Tb green emission via energy transfer.

The Tb:YSO layers grown on Ce:YSO substrate have strong violet - blue emission along with emission ranging from 475 nm to 650 nm. It is separated in bands of sharp line like structures with dominant peak at 541 nm. The strongest PL occurs at lower doping, at 0.08 p.f.u. of Tb. The RL spectra have maxima for higher Tb concentration, 0.16 p.f.u. The surface quality of layers slowly worsened as the Tb concentration increased. Fine-tuning of the growth process helped against this deterioration.

The Ce:YSO and CeZr:YSO show strong UV-blue 5d - 4f emission of Ce^{3+} ranging from 370 to 500 nm. Heavy absorption in the UV below 350 nm is probably caused by the presence of Ce^{4+}. The Ce^{4+} is created as consequence of charge compensation of Pb^{2+} ions. Potential improvement by annealing in oxygen (air) or hydrogen was not observed. This is the first time a PL in epitaxial film of Ce:YSO was reported (in literature [131, 133, 135] quenched). Optimal Zr and Ce codoping, with 0.0022 p.f.u. of Zr and 0.0048 p.f.u. Ce improved PL, RL and the decay time. Too high doping concentrations of both Ce and Zr lead to quenching of luminescence and enlarging of 435 nm peak in PL and RL spectra. The Ce:YSO has fast decay time between 18 and 25 ns. Photoelectron yield measurements confirmed complete absence of long components. The surface quality of layers deteriorated as the Ce concentration increased despite growth process fine-tuning. Best results were obtained with samples grown close to saturation temperature, when the detrimental effect of Pb^{2+} ions on PL and scintillation properties was minimal.

7. List of abbreviations

ASCR	Academy of Sciences of the Czech Republic
BGO	Bismuth germanate scintillation material, molecular formula: $Bi_4Ge_3O_{12}$
CB	Conduction band
CFL	compact fluorescent light
CZ	Czochralski method
EDS	Energy Dispersive X-ray spectrometers
EDS	Energy-Dispersive X-Ray Spectroscopy
EELS	Electron Energy Loss Spectroscopy in theTransmission Electron Microscope
EPMA	Electron Probe X-Ray Microanalysis
FTIR	Fourier Transform Infrared Spectroscopy
FWHM	Full width at half of the maximum
GAG	gadolinium aluminum garnet
GDMS	Glow Discharge Mass Spectrometry
HREELS	High Resolution Electron Energy Loss Spectroscopy
ICPMS	Inductively Coupled Plasma Mass Spectrometry
ICPOES	Inductively Coupled Plasma-Optical Emission Spectroscopy
LED	Light emitting diode
LuAG	Lutetium aluminium garnet, molecular formula: $Lu_3Al_5O_{12}$
Lu_{Al}	Anti-site defect, Lu resides in the Al site
NMR	Solid State Nuclear Magnetic Resonance
p.f.u.	atoms per formula unit
PET	Positron emission tomography
PL	Photoluminescence
PMT	Photomultiplier tube
RL	Radioluminescence
RT	Room temperature
SEM	Scanning Electron Microscopy
SFM	Scanning Force Microscopy
STEM	Scanning Transmission Electron Microscopy
STM	Scanning Tunneling Microscopy
TCSPC	Time-correlated single photon counting
TEM	Transmission Electron Microscopy
TSL	Thermally stimulated luminescence
UV	Ultraviolet light
VASE	Variable Angle Spectroscopic Ellipsometry
VB	Valence band
WDS	Wavelength Dispersive X-ray spectrometers

XRD	X-Ray Diffraction
YAG	Yttrium aluminium garnet, molecular formula: $Y_3Al_5O_{12}$
YSO	Yttrium oxyorthosilicate, molecular formula: Y_2SiO_5

References

1. Mueller-Mach, R., G. Mueller, M.R. Krames, H.A. Höppe, F. Stadler, et al., *Highly efficient all-nitride phosphor-converted white light emitting diode.* physica status solidi (a), 2005. **202**(9): p. 1727-1732.

2. Hoppe, H.A., *Recent developments in the field of inorganic phosphors.* Angewandte Chemie, 2009. **48**(20): p. 3572-82.

3. Martin, T. and A. Koch, *Recent developments in X-ray imaging with micrometer spatial resolution.* Journal of Synchrotron Radiation, 2006. **13**: p. 180-194.

4. Tous, J., M. Horvath, L. Pina, K. Blazek, and B. Sopko, *High-resolution application of YAG : Ce and LuAG : Ce imaging detectors with a CCD X-ray camera.* Nuclear Instruments & Methods in Physics Research Section a-Accelerators Spectrometers Detectors and Associated Equipment, 2008. **591**(1): p. 264-267.

5. Zorenko, Y., A. Voloshinovskii, V. Savchyn, T. Voznyak, M. Nikl, et al., *Exciton and antisite defect-related luminescence in $Lu_3Al_5O_{12}$ and $Y_3Al_5O_{12}$ garnets.* physica status solidi (b), 2007. **244**(6): p. 2180-2189.

6. Nikl, M., A. Vedda, M. Fasoli, I. Fontana, V.V. Laguta, et al., *Shallow traps and radiative recombination processes in $Lu_3Al_5O_{12}$: Ce single crystal scintillator.* Physical Review B, 2007. **76**(19).

7. *http://www.crytur.cz/*.

8. Blasse, G. and B.C. Grabmaier, *Luminescent materials*. 1994, Berlin: Springer-Verlag.

9. Solé, J.G., L.E. Bausá, and D. Jaque, *An Introduction to the Optical Spectroscopy of Inorganic Solids*. 2005: John Wiley & Sons Ltd.

10. Fox, M., *Optical Properties of Solids*. 2001: Oxford University Press.

11. Lecoq, P., A. Annenkov , A. Gektin, M. Korzhik, and C. Pedrini, *Inorganic scintillators for detector systems*. 2006, Berlin: Springer.

12. Halmshaw, R., *Industrial Radiology Theory and practice Second edition*. 1995, London Chapman & Hall.

13. Elwell, D. and H.J. Scheel, *Crystal growth from high temperature solution*. 2. ed. 2011, London: Academic Press.

14. Karaseva, L.G., N.Y. Konstantinov, and V.V. Gromov, *NATURE OF RADIATION COLOR-CENTERS IN SINGLE-CRYSTALS OF YTTRIUM ALUMINUM GARNET.* Radiation Physics and Chemistry, 1985. **26**(6): p. 723-730.

15. Ashurov, M.K., A.F. Rakov, and R.A. Erzin, *Luminescence of defect centers in yttrium-aluminum garnet crystals.* Solid State Communications, 2001. **120**(12): p. 491-494.

16. Dorenbos, P., *The 5d level positions of the trivalent lanthanides in inorganic compounds.* Journal of Luminescence, 2000. **91**(3-4): p. 155-176.

17. Wu, J.L., G. Gundiah, and A.K. Cheetham, *Structure–property correlations in Ce-doped garnet phosphors for use in solid state lighting.* Chemical Physics Letters, 2007. **441**(4-6): p. 250-254.

18. Nikl, M., *Scintillation detectors for x-rays.* Measurement Science & Technology, 2006. **17**(4): p. R37-R54.

19. Pejchal, J., *Yb^{3+} and Pr^{3+} -doped materials for fast scintillators*, in *Faculty of Nuclear Sciences and Physical Engineering, Department of Nuclear Chemistry*. 2007, Czech Technical University in Prague: Prague.

20. Moszynski, M., M. Kapusta, M. Mayhugh, D. Wolski, and S.O. Flyckt, *Absolute light output of scintillators.* IEEE Trans. Nucl. Sci., 1997(44): p. 1052-1061.

21. van Eijk, C.W.E., *Inorganic scintillators in medical imaging.* Physics in Medicine and Biology, 2002. **47**(8): p. R85-R106.

22. Rodnyi, P.A., *Physical processes in inorganic scintillators*. 1997, Boca Raton: CRC Press.

23. Kuwano, Y., K. Suda, N. Ishizawa, and T. Yamada, *Crystal growth and properties of $(Lu,Y)_3Al_5O_{12}$.* Journal of Crystal Growth, 2004. **260**(1-2): p. 159-165.

24. Blasse, G. and A. Bril, *A NEW PHOSPHOR FOR FLYING-SPOT CATHODE-RAY TUBES FOR COLOR TELEVISION - YELLOW-EMITTING Y3Al5O12-Ce3+*. Applied Physics Letters, 1967. **11**(2): p. 53-&.

25. Blasse, G. and A. Bril, *INVESTIGATION OF SOME Ce3+-ACTIVATED PHOSPHORS.* Journal of Chemical Physics, 1967. **47**(12): p. 5139-&.

26. Tomiki, T., H. Akamine, M. Gushiken, Y. Kinjoh, M. Miyazato, et al., *Ce^{3+} centers in $Y_3Al_5O_{12}$ (YAG) single-crystals.* Journal of the Physical Society of Japan, 1991. **60**(7): p. 2437-2445.

27. Nikl, M., *Wide band gap scintillation materials: Progress in the technology and material understanding.* Physica Status Solidi a-Applied Research, 2000. **178**(2): p. 595-620.

28. Dorenbos, P., *5d-level energies of Ce^{3+} and the crystalline environment. I. Fluoride compounds.* Physical Review B, 2000. **62**(23): p. 15640-15649.

29. Dorenbos, P., *5d-level energies of Ce3+ and the crystalline environment. II. Chloride, bromide, and iodide compounds.* Physical Review B, 2000. **62**(23): p. 15650-15659.

30. Dorenbos, P., *5d-level energies of Ce3+ and the crystalline environment. III. Oxides containing ionic complexes.* Physical Review B, 2001. **64**(12): p. 125117.

31. Dorenbos, P., *5d-level energies of Ce3+ and the crystalline environment. IV. Aluminates and "simple" oxides.* Journal of Luminescence, 2002. **99**(3): p. 283-299.

32. Zorenko, Y., V. Gorbenko, I. Konstankevych, B. Grinev, and M. Globus, *Scintillation properties of $Lu_3Al_5O_{12}$:Ce single-crystalline films.* Nuclear Instruments & Methods in Physics Research Section a-Accelerators Spectrometers Detectors and Associated Equipment, 2002. **486**(1-2): p. 309-314.

33. Kuklja, M.M., *Defects in yttrium aluminium perovskite and garnet crystals: atomistic study.* Journal of Physics-Condensed Matter, 2000. **12**(13): p. 2953-2967.

34. Stanek, C.R., K.J. McClellan, M.R. Levy, and R.W. Grimes, *Extrinsic defect structure of $RE_3Al_5O_{12}$ garnets.* physica status solidi (b), 2006. **243**(11): p. R75-R77.

35. Wang, C.L., D. Solodovnikov, and K.G. Lynn, *Point defects in Ce-doped Y3Al5O12 crystal scintillators.* Physical Review B, 2006. **73**(23).

36. Wu, Y., J. Luo, M. Nikl, and G. Ren, *Origin of improved scintillation efficiency in (Lu,Gd)3(Ga,Al)5O12:Ce multicomponent garnets: An X-ray absorption near edge spectroscopy study.* APL Materials, 2014. **2**(1): p. 012101.

37. Nikl, M., *Energy transfer phenomena in the luminescence of wide band-gap scintillators.* Physica Status Solidi a-Applied Research, 2005. **202**(2): p. 201-206.

38. Zorenko, Y., V. Gorbenko, I. Konstankevych, A. Voloshinovskii, G. Stryganyuk, et al., *Single-crystalline films of Ce-doped YAG and LuAG phosphors: advantages over bulk crystal analogues.* Journal of Luminescence, 2005. **114**: p. 85 – 94.

39. Babin, V., V. Gorbenko, A. Makhov, J.A. Mares, M. Nikl, et al., *Luminescence characteristics of Pb^{2+} centres in undoped and Ce^{3+}-doped $Lu_3Al_5O_{12}$ single-crystalline films and Pb^{2+} to Ce^{3+} energy transfer processes.* Journal of Luminescence, 2007. **127**(2): p. 384-390.

40. Babin, V., V. Gorbenk, A. Makhov, M. Nikl, S. Zazubovich, et al., *The role of Pb2+ ions in the luminescence of LuAG : Ce single crystalline films.* Physica Status Solidi C - Current Topics in Solid State Physics, Vol 4, No 3, 2007. **4**(3): p. 797-800.

41. Zorenko, Y., V. Gorbenko, T. Voznyak, and T. Zorenko, *Luminescence of Pb^{2+} ions in YAG:Pb single-crystalline films.* physica status solidi (b), 2008. **245**(8): p. 1618-1622.

42. Nikl, M., H. Ogino, A. Krasnikov, A. Beitlerova, A. Yoshikawa, et al., *Photo- and radioluminescence of Pr-doped $Lu_3Al_5O_{12}$ single crystal.* Physica Status Solidi a-Applied Research, 2005. **202**(1): p. R4-R6.

43. Eijk, C.W.E.v., P. Dorenbos, and R. Visser, *Nd^{3+} and Pr^{3+} doped inorganic scintillators.* IEEE Trans. Nucl. Sci., 1994. **41**(4): p. 738-741.

44. Drozdowski, W., T. Lukasiewicz, A. Wojtowicz, D. Wisniewski, and J. Kisielewski, *Thermoluminescence and scintillation of praseodymium-activated $Y_3Al_5O_{12}$ and $LuAlO_3$ crystals.* Journal of Crystal Growth, 2005. **275**(1-2): p. e709-e714.

45. Ogino, H., A. Yoshikawa, M. Nikl, A. Krasnikov, K. Kamada, et al., *Growth and scintillation properties of Pr-doped $Lu_3Al_5O_{12}$ crystals.* Journal of Crystal Growth, 2006. **287**(2): p. 335-338.

46. Yoshikawa, A., K. Kamada, F. Saito, H. Ogino, M. Itoh, et al., *Energy transfer to Pr3+ ions in Pr : Lu-3 Al5O12 (LuAG) single crystals.* Ieee Transactions on Nuclear Science, 2008. **55**(3): p. 1372-1375.

47. Ogino, H., A. Yoshikawa, M. Nikl, R. Kucerkova, J. Shimoyama, et al., *Suppression of defect related host luminescence in LuAG single crystals*, in *2008 International Conference on Luminescence and Optical Spectroscopy of Condensed Matter*, G. Boulon, C. Dujardin, and A.M. Jurdyc, Editors. 2009. p. 191-205.

48. Ogino, H., K. Kamada, A. Yoshikawa, F. Saito, J. Pejchal, et al., *Suppression of host luminescence in the Pr : LuAG scintillator.* Ieee Transactions on Nuclear Science, 2008. **55**(3): p. 1197-1200.

49. Robertson, J.M. and M.W. Vantol, *EPITAXIALLY GROWN MONO-CRYSTALLINE GARNET CATHODE-RAY TUBE PHOSPHOR SCREENS.* Applied Physics Letters, 1980. **37**(5): p. 471-472.

50. Ogieglo, J.M., A. Zych, K.V. Ivanovskikh, T. Jüstel, C.R. Ronda, et al., *Luminescence and Energy Transfer in Lu3Al5O12 Scintillators Co-Doped with Ce3+ and Tb3+*. The Journal of Physical Chemistry A, 2012. **116**(33): p. 8464-8474.

51. Potdevin, A., G. Chadeyron, and R. Mahiou, *Tb3+-doped yttrium garnets: Promising tunable green phosphors for solid-state lighting.* Chemical Physics Letters, 2010. **490**(1-3): p. 50-53.

52. Park, J.Y., H.C. Jung, G.S.R. Raju, B.K. Moon, J.H. Jeong, et al., *Solvothermal synthesis and luminescence properties of Tb^{3+}-doped gadolinium aluminum garnet.* Journal of Luminescence, 2010. **130**(3): p. 478-482.

53. Potdevin, A., G. Chadeyron, D. Boyer, and R. Mahiou, *Optical properties upon vacuum ultraviolet excitation of sol-gel based Y3Al5O12 : Tb3+, Ce3+ powders.* Journal of Applied Physics, 2007. **102**(7).

54. G. H. Dieke, H.M.C., *The Spectra of the Doubly and Triply Ionized Rare Earths.* Appl. Opt., 1963. **2**: p. 11.

55. Ogieglo, J.M., A. Zych, T. Juestel, A. Meijerink, and C.R. Ronda, *Luminescence and energy transfer in Lu3Al5O12 scintillators co-doped with Ce3+ and Pr3+*. Optical Materials, 2013. **35**(3): p. 322-331.

56. Kamada, K., T. Endo, K. Tsutumi, T. Yanagida, Y. Fujimoto, et al., *Composition Engineering in Cerium-Doped (Lu,Gd)3(Ga,Al)5O12Single-Crystal Scintillators.* Crystal Growth & Design, 2011. **11**(10): p. 4484-4490.

57. Kamada, K., T. Yanagida, J. Pejchal, M. Nikl, T. Endo, et al., *Scintillator-oriented combinatorial search in Ce-doped (Y,Gd)3(Ga,Al)5O12multicomponent garnet compounds.* Journal of Physics D: Applied Physics, 2011. **44**(50): p. 505104.

58. Yang, H., D.-K. Lee, and Y.-S. Kim, *Spectral variations of nano-sized $Y_3Al_5O_{12}$:Ce phosphors via codoping/substitution and their white LED characteristics.* Materials Chemistry and Physics, 2009. **114**(2-3): p. 665-669.

59. Kottaisamy, M., P. Thiyagarajan, J. Mishra, and M.S. Ramachandra Rao, *Color tuning of $Y_3Al_5O_{12}$:Ce phosphor and their blend for white LEDs.* Materials Research Bulletin, 2008. **43**(7): p. 1657-1663.

60. Zorenko, Y., V. Gorbenko, V. Savchyn, T. Zorenko, A. Fedorov, et al., *Multi-component Ce doped (Gd,Y,La,Lu)3(AlGaSc)5O12 garnets - A new story in the development of scintillating single crystalline film screens.* Radiation Measurements, 2013. **56**: p. 150-154.

61. Zorenko, Y., V. Gorbenko, V. Savchyn, T. Zorenko, A. Fedorov, et al., *Novel Scintillating Screens Based on the Single Crystalline Films of Ce Doped Multi-Component (GdYLu)3(AlSc)5O12 Garnets.* Ieee Transactions on Nuclear Science, 2014. **61**(1): p. 439-442.

62. Nikl, M., A. Vedda, and V.V. Laguta, *Energy transfer and storage processes in scintillators: The role and nature of defects.* Radiation Measurements, 2007. **42**(4-5): p. 509-514.

63. Fasoli, M., A. Vedda, M. Nikl, C. Jiang, B.P. Uberuaga, et al., *Band-gap engineering for removing shallow traps in rare-earth Lu3Al5O12 garnet scintillators using Ga3+ doping.* Physical Review B, 2011. **84**(8): p. 081102(R).

64. Bachmann, V., C. Ronda, and A. Meijerink, *Temperature Quenching of Yellow Ce^{3+} Luminescence in YAG:Ce.* Chemistry of Materials, 2009. **21**(10): p. 2077-2084.

65. Chani, V., *Effect of cation radii on the formation of complex oxide crystals.* Journal of Ceramic Processing Research, 2003. **4**(2): p. 67-70.

66. Strocka, B., P. Holst, and W. Tolksdorf, *Empirical formula for the calculation of lattice constants of oxide garnets based on substituted yttrium-iron and gadolinium-iron garnets.* Philips Journal of Research, 1978. **33**(3-4): p. 186-202.

67. *http://abulafia.mt.ic.ac.uk/shannon/.*

68. Shannon, R.D., *Revised Effective Ionic Radii and Systematic Studies of Interatomic Distances in Halides and Chalcogenides.* Acta Cryst. A, 1976. **32**: p. 751-767.

69. Yousif, A., H.C. Swart, and O.M. Ntwaeaborwa, *Effect of annealing on the structure of $Y_3(Al,Ga)_5O_{12}$:Tb thin films grown by PLD.* The 58th Annual Conference of the South Africa Institute of Physics, 2014.

70. Thiel, M., W.M. Doring, V. Dormenev, P. Drexler, R.W. Novotny, et al., *High-energy photon detection with LYSO crystals.* Ieee Transactions on Nuclear Science, 2008. **55**(3): p. 1425-1429.

71. Melcher, C.L., R.A. Manente, C.A. Peterson, and J.S. Schweitzer, *CZOCHRALSKI GROWTH OF RARE-EARTH OXYORTHOSILICATE SINGLE-CRYSTALS.* Journal of Crystal Growth, 1993. **128**(1-4): p. 1001-1005.

72. Cooke, D.W., K.J. McClellan, B.L. Bennett, J.M. Roper, M.T. Whittaker, et al., *Crystal growth and optical characterization of cerium-doped Lu1.8Y0.2SiO5.* Journal of Applied Physics, 2000. **88**(12): p. 7360-7362.

73. *http://www.scientificmaterials.com.*

74. Gustafsson, T., M. Klintenberg, S.E. Derenzo, M.J. Weber, and J.O. Thomas, *Lu_2SiO_5 by single-crystal X-ray and neutron diffraction.* Acta Crystallographica Section C-Crystal Structure Communications, 2001. **57**: p. 668-669.

75. Moszynski, M., M. Balcerzyk, M. Kapusta, D. Wolski, and C.L. Melcher, *Large size LSO:Ce and YSO:Ce scintillators for 50 MeV range gamma-ray detector.* Ieee Transactions on Nuclear Science, 2000. **47**(4): p. 1324-1328.

76. Melcher, C.L., L.A. Eriksson, M. Aykac, F. Bauer, C. Williams, et al., *Current and future use of LSO: CE scintillators in PET*, in *Radiation Detectors for Medical Applications*, S. Tavernier, et al., Editors. 2006. p. 243-257.

77. Drozdowski, W., A.J. Wojtowicz, D. Wisniewski, P. Szupryczynski, S. Janus, et al., *VUV spectroscopy and low temperature thermoluminescence of LSO:Ce and YSO:Ce.* Journal of Alloys and Compounds, 2004. **380**(1-2): p. 146-150.

78. Blahuta, S., A. Bessiere, B. Viana, P. Dorenbos, and V. Ouspenski, *Evidence and Consequences of Ce4+ in LYSO:Ce, Ca and LYSO:Ce, Mg Single Crystals for Medical Imaging Applications.* Ieee Transactions on Nuclear Science, 2013. **60**(4): p. 3134-3141.

79. Blahuta, S., A. Bessiere, B. Viana, V. Ouspenski, E. Mattmann, et al., *Defects Identification and Effects of Annealing on Lu2(1-x)Y2xSiO5 (LYSO) Single Crystals for Scintillation Application.* Materials, 2011. **4**(7): p. 1224-1237.

80. D.Ding, H.F., G.Ren, M.Nikl, L.Qin, S.Pan ,and F.Yang, *Air atmosphere annealing effects on LSO:Ce crystal.* IEEE Trans. Nucl. Sci. , 2010. **vol. 57**(no. 3): p. 1272–1277.

81. Koschan, M., K. Yang, M. Zhuravleva, and C.L. Melcher, *A comparison of the effect of Ca2+ codoping in cerium doped GSO with that of LSO and YSO.* Journal of Crystal Growth, 2012. **352**(1): p. 133-136.

82. M Salis, C.M.C., R Corpino, A Anedda, P C Ricci, *Investigation of energy transfer in terbium doped Y_2SiO_5 phosphor particles.* JOURNAL OF PHYSICS: CONDENSED MATTER, 2012. **24**.

83. Cecilia, A., A. Rack, P.A. Douissard, T. Martin, T. dos Santos Rolo, et al., *LPE grown LSO:Tb scintillator films for high-resolution X-ray imaging applications at synchrotron light sources.* Nuclear Instruments and Methods in Physics Research Section A: Accelerators, Spectrometers, Detectors and Associated Equipment, 2011. **648, Supplement 1**(0): p. S321-S323.

84. Cecilia, A., A. Rack, P.A. Douissard, T. Martin, T. dos Santos Rolo, et al., *Characterisation of LSO:Tb scintillator films for high resolution X-ray imaging applications.* Nuclear Instruments and Methods in Physics Research Section A:

Accelerators, Spectrometers, Detectors and Associated Equipment, 2011. **633, Supplement 1**(0): p. S292-S293.

85. Cecilia, A., V. Jary, M. Nikl, E. Mihokova, D. Haenschke, et al., *Investigation of the luminescence, crystallographic and spatial resolution properties of LSO:Tb scintillating layers used for X-ray imaging applications.* Radiation Measurements, 2014. **62**: p. 28-34.

86. Kucera, M., K. Nitsch, H. Stepankova, M. Marysko, and P. Reiche, *Growth and characterization of high purity epitaxial yttrium iron garnet films grown from BaO-B_2O_3-BaF_2 flux.* Physica Status Solidi a-Applied Research, 2003. **198**(2): p. 407-414.

87. Tang, H.G., B.J. Garrard, and B.M. Wanklyn, *Solubility and relative supersaturation in the fluxed-melt system La_2O_3-PbO-B_2O_3.* Journal of Crystal Growth, 1982. **58**: p. 111-114.

88. Levin, M.E. and F.H. McMurdie, *The System BaO-B_2O_3,*. U. S. Department of Commerce, National Bureau of Standards, 1949. **42**(Research Paper RPl956): p. 131-138.

89. Capper, P. and D. Elwell, *Appraisal of $BaO/B_2O_3/BaF_2$ fluxes for the growth of yttrium aluminium garnet.* Journal of Crystal Growth, 1974. **26**(1): p. 65-68.

90. Elwell, D., P. Capper, and C.M. Lawrence, *Viscosity and density of $BaO/B_2O_3/BaF_2$ fluxes and solutions.* Journal of Crystal Growth, 1974. **24**(OCT): p. 651-655.

91. Suemune, Y. and N. Inoue, *Crystallization of garnets in BaO-BaF_2-B_2O_3 solvents.* Journal of Crystal Growth, 1974. **24**(OCT): p. 646-650.

92. Blank, S.L. and J.W. Nielsen, *GROWTH OF MAGNETIC GARNETS BY LIQUID-PHASE EPITAXY.* Journal of Crystal Growth, 1972. **17**(DEC): p. 302-311.

93. Robertson, J.M., *LIQUID-PHASE EPITAXY OF GARNETS.* Journal of Crystal Growth, 1978. **45**(1): p. 233-242.

94. Robertson, J.M. and M.W. Vantol, *CATHODOLUMINESCENT GARNET LAYERS.* Thin Solid Films, 1984. **114**(1-2): p. 221-240.

95. Chani, V., K. Shimamura, M.Y. Yu, and T. Fukuda, *Design of new oxide crystals with improved structural stability.* Materials Science and Engineering, 1997. **R20**: p. 281-338.

96. Kucera, M., K. Nitsch, M. Kubova, N. Solovieva, M. Nikl, et al., *Ce-doped YAG and LuAG epitaxial films for scintillation detectors.* Ieee Transactions on Nuclear Science, 2008. **55**(3): p. 1201-1205.

97. Brandle, C.D., *Czochralski growth of oxides.* Journal of Crystal Growth, 2004. **264**(4): p. 593-604.

98. Kucera, M., K. Nitsch, M. Marysko, and H. Stepankova, *Properties of epitaxial yttrium iron garnet films grown from BaO flux.* Journal of Applied Physics, 2003. **93**(10): p. 7510-7512.

99. Kucera, M., K. Nitsch, M. Nikl, M. Hanus, and S. Danis, *Growth and characterization of YAG and LuAG epitaxial films for scintillation applications.* Journal of Crystal Growth, 2010. **312**(9): p. 1538-1545.

100. Scott, G.B. and J.L. Page, *Pb valence in iron garnets.* Journal of Applied Physics, 1977. **48**(3): p. 1342 - 1349.

101. Kučera, M., K. Nitsch, M. Nikl, S. Daniš, and M. Hanuš, *Growth and properties of epitaxial Ce-doped YAG and LuAG films for scintillators.* Journal of Physics: Conference Series, 2010. **249**: p. 012020.

102. Gerhardt, R., *Channel Waveguide Lasers in Epitaxial Garnet Films*, in *Fachbereich Physik*. 2001, Universität Osnabrück.

103. Mares, J.A. and C. D'Ambrosio, *Hybrid photomultipliers - their properties and application in scintillation studies.* Optical Materials, 2007. **30**(1): p. 22-25.

104. Prusa, P., M. Nikl, J.A. Mares, M. Kucera, K. Nitsch, et al., *The alpha-particle excited scintillation response of YAG:Ce thin films grown by liquid phase epitaxy.* Physica Status Solidi a-Applications and Materials Science, 2009. **206**(7): p. 1494-1500.

105. Prusa, P., T. Cechak, J.A. Mares, M. Nikl, A. Beitlerova, et al., *The alpha-particle excited scintillation response of the liquid phase epitaxy grown LuAG:Ce thin films.* Applied Physics Letters, 2008. **92**(4).

106. Mares, J.A., P. Prusa, M. Nikl, K. Nitsch, A. Beitlerova, et al., *Ce^{3+}-doped crystalline garnet films - scintillation characterization using alpha-particle excitation.* Radiation Measurements, 2010. **45**(3-6): p. 369-371.

107. Brundle, C.R., J. Charles A. Evans, S. Wilson, and L.E. Fitzpatrick, *Encyclopedia of Materials Characterization: Surfaces, Interfaces, Thin Films*. 1992, Greenwich: Butterworth-Heinemann, a division of Reed Publishing (USA) Inc.

108. Onderišinová, Z., *Oxide scintillator detectors,* in *Faculty of Mathematics and Physics*. 2015, Charles University in Prague: Prague.

109. Onderisinova, Z., M. Kucera, M. Hanus, and M. Nikl, *Temperature-dependent nonradiative energy transfer from Gd3+ to Ce3+ ions in co-doped LuAG:Ce, Gd garnet scintillators.* Journal of Luminescence, 2015. **167**: p. 106-113.

110. Kucera, M., K. Nitsch, M. Nikl, and M. Hanus, *Defects in Ce-doped LuAG and YAG scintillation layers grown by liquid phase epitaxy.* Radiation Measurements, 2010. **45**(3-6): p. 449-452.

111. Kucera, M., M. Nikl, M. Hanus, and Z. Onderisinova, *Gd3+ to Ce3+ energy transfer in multi-component GdLuAG and GdYAG garnet scintillators* Physica Status Solidi-Rapid Research Letters, 2013. **7**(8): p. 571-574.

112. Nikl, M., E. Mihokova, J. Pejchal, A. Vedda, Y. Zorenko, et al., *The antisite Lu-Al defect-related trap in Lu3Al5O12 : Ce single crystal.* Physica Status Solidi B-Basic Solid State Physics, 2005. **242**(14): p. R119-R121.

113. Robertson, J.M., M.W. Vantol, J.P.H. Heynen, W.H. Smits, and T. Deboer, *Thin Single Crystalline Phosphor Layers Grown By Liquid-Phase Epitaxy.* Philips Journal of Research, 1980. **35**(6): p. 354-371.

114. Prusa, P., M. Kucera, J.A. Mares, Z. Onderisinova, M. Hanus, et al., *Composition Tailoring in Ce-Doped Multicomponent Garnet Epitaxial Film Scintillators.* Crystal Growth & Design, 2015. **15**(8): p. 3715-3723.

115. Yang, H. and Y.S. Kim, *Energy transfer-based spectral properties of Tb-, Pr-, or Sm-codoped YAG : Ce nanocrystalline phosphors.* Journal of Luminescence, 2008. **128**(10): p. 1570-1576.

116. Kučera, M., M. Nikl, P. Průša, J.A. Mareš, K. Nitsch, et al., *Growth and emission properties of Sc, Pr, and Ce co-doped $Lu_3Al_5O_{12}$ epitaxial layers for scintillators.* Journal of Crystal Growth, 2011. **318**(1): p. 813-819.

117. Pejchal, J., M. Nikl, E. Mihokova, J.A. Mares, A. Yoshikawa, et al., *Pr^{3+}-doped complex oxide single crystal scintillators.* Journal of Physics D-Applied Physics, 2009. **42**(5).

118. Ryskin, N.N., P. Dorenbos, C.W.E. Vaneijk, and S.K. Batygov, *SCINTILLATION PROPERTIES OF LU3AL5-XSCXO12 CRYSTALS.* Journal of Physics-Condensed Matter, 1994. **6**(47): p. 10423-10434.

119. Prusa, P., M. Kucera, J.A. Mares, M. Nikl, K. Nitsch, et al., *Scintillation properties of Sc-, Pr-, and Ce-doped LuAG epitaxial garnet films.* Journal of Crystal Growth, 2011. **318**(1): p. 545-548.

120. W. F. van der Weg, T.J.A. Popma, and A.T. Vink, *Concentration dependence of UV and electron-excited Tb^{3+} luminescence in $Y_3Al_5O_{12}$.* J. Appl. Phys., 1985. **57**: p. 6.

121. Nikl, M., N. Solovieva, M. Dusek, A. Yoshikawa, Y. Kagamitani, et al., *Concentration quenching of Tb^{3+} luminescence in $Tb_xA_{3-x}Al_5O_{12}$ (A=Yb, Y) single crystals.* Journal of Ceramic Processing Research, 2003. **4**(3): p. 112-114.

122. Shimamura, K., T. Kito, E. Castel, A. Latynina, P. Molina, et al., *Growth of {Tb3}[Sc2−xLux](Al3)O12Single Crystals for Visible-Infrared Optical Isolators.* Crystal Growth & Design, 2010. **10**(8): p. 3466-3470.

123. Kucera, M., M. Nikl, M. Hanus, Z. Onderisinova, and A. Beitlerova, *Growth, Emission and Scintillation Properties of Tb-Sc Doped LuAG Epitaxial Films.* Ieee Transactions on Nuclear Science, 2012. **59**(5): p. 2275-2280.

124. van der Ziel, J.P., L. Kopf, and L.G. Van Uitert, *Quenching of Tb3+ Luminescence by Direct Transfer and Migration in Aluminum Garnets.* Physical Review B, 1972. **6**(2): p. 615-623.

125. Zorenko, Y.V., *Luminescence of Sc^{3+} and La^{3+} isoelectronic impurities in $Lu_3Al_5O_{12}$ single-crystal films.* Optics and Spectroscopy, 2006. **100**(4): p. 572-580.

126. Jarý, V., *Thermally induced ionization and quenching processes in novel oxide and sulfide scintillation materials*, in *Faculty of Nuclear Sciences and Physical Engineering*. 2014, Czech Technical University in Prague: Prague.

127. Gorbenko, V., A. Krasnikov, E. Mihokova, M. Nikl, S. Zazubovich, et al., *Luminescence of lead-related centres in single crystalline films of Lu2SiO5.* Journal of Physics D-Applied Physics, 2012. **45**(35): p. 355304.

128. Visser, R., C.L. Melcher, and J.S. Schweitzer, *Photostimulated Luminescence and Thermoluminescence of LSO Scintillators.* Ieee Transactions on Nuclear Science, 1994. **41**(4): p. 689-693.

129. Jary, V., M. Nikl, G. Ren, P. Horodysky, G.P. Pazzi, et al., *Influence of yttrium content on the Ce_{Lu1} and Ce_{Lu2} luminescence characteristics in $(Lu_{1-x}Y_x)_2SiO_5$:Ce single crystals.* Optical Materials, 2011. **34**(2): p. 428-432.

130. Zorenko, Y., V. Gorbenko, V. Savchyn, T. Voznyak, B. Grinyov, et al., *Growth and luminescent properties of Lu2SiO5:Ce and (Lu1−xGdx)2SiO5:Ce single crystalline films.* Journal of Crystal Growth, 2011. **337**(1): p. 72-80.

131. Zorenko, Y., M. Nikl, V. Gorbenko, V. Savchyn, T. Voznyak, et al., *Growth and luminescent properties of Lu2SiO5 and Lu2SiO5:Ce single crystalline films.* Optical Materials, 2011. **33**(6): p. 846-852.

132. Zorenko, Y., V. Gorbenko, V. Savchyn, T. Voznyak, V.V. Gorbenko, et al., *Scintillation and luminescent properties of undoped and Ce3+ doped Y2SiO5 and Lu2SiO5 single crystalline films grown by LPE method.* Optical Materials, 2012. **34**(12): p. 1969-1974.

133. Zorenko, Y., V. Gorbenko, V. Savchyn, T. Voznyak, O. Sidletskiy, et al., *Single Crystalline Film Scintillators Based on the Orthosilicate, Perovskite and Garnet Compounds.* Ieee Transactions on Nuclear Science, 2012. **59**(5): p. 2260-2268.

134. Babin, V., V. Gorbenko, A. Krasnikov, E. Mihokova, M. Nikl, et al., *Luminescence and origin of lead-related centers in single crystalline films of Y2SiO5 and Lu2SiO5.* Radiation Measurements, 2013. **56**: p. 124 - 128.

135. Zorenko, Y., V. Gorbenko, V. Savchyn, T. Zorenko, B. Grinyov, et al., *Lu2SiO5:Ce and Y2SiO5:Ce single crystals and single crystalline film scintillators: Comparison of the luminescent and scintillation properties.* Radiation Measurements, 2013. **56**: p. 84 - 89.

136. Zorenko, Y., T. Zorenko, T. Voznyak, and O. Sidletskiy, *Intrinsic luminescence of Lu2SiO5 (LSO) and Y2SiO5 (YSO) orthosilicates.* Journal of Luminescence, 2013. **137**: p. 204-207.

137. Zorenko, Y., V. Gorbenko, V. Savchyn, T. Zorenko, B. Grinyov, et al., *Growth and luminescent properties of Ce and Ce–Tb doped (Y,Lu,Gd)2SiO5:Ce single crystalline films.* Journal of Crystal Growth, 2014. **401**(0): p. 577-583.

138. Suzuki, H., T.A. Tombrello, C.L. Melcher, and J.S. Schweitzer, *UV and gamma-ray excited luminescence of cerium-doped rare-earth oxyorthosilicates.* Nuclear Instruments and Methods in Physics Research Section A: Accelerators, Spectrometers, Detectors and Associated Equipment, 1992. **320**(1–2): p. 263-272.

Thesis-related publications

Kucera, M., K. Nitsch, M. Nikl, M. Hanus, and S. Danis, *Growth and characterization of YAG and LuAG epitaxial films for scintillation applications.* Journal of Crystal Growth, 2010. **312**(9): p. 1538-1545.

Kučera, M., K. Nitsch, M. Nikl, S. Daniš, and M. Hanuš, *Growth and properties of epitaxial Ce-doped YAG and LuAG films for scintillators.* Journal of Physics: Conference Series, 2010. **249**: p. 012020.

Kučera, M., P. Pruša, J.A. Mareš, M. Nikl, K. Nitsch, M. Hanuš, Z. Onderišinová, and R. Kučerková, *Growth and scintillation properties of Sc, Pr, Ce co-doped LuAG epitaxial garnet layers.* IOP Conference Series: Materials Science and Engineering, 2010. **15**: p. 012012.

Mares, J.A., P. Prusa, M. Nikl, K. Nitsch, A. Beitlerova, M. Kucera, M. Hanus, and Y. Zorenko, *Ce^{3+}-doped crystalline garnet films - scintillation characterization using alpha-particle excitation.* Radiation Measurements, 2010. **45**(3-6): p. 369-371.

Prusa, P., J.A. Mares, M. Nikl, M. Kucera, K. Nitsch, and M. Hanus, *Scintillation properties of LuAG:Ce single crystalline films grown by LPE method.* Optical Materials, 2010. **32**(10): p. 1360-1363.

Kučera, M., M. Nikl, P. Průša, J.A. Mareš, K. Nitsch, M. Hanuš, Z. Onderišinová, and R. Kučerková, *Growth and emission properties of Sc, Pr, and Ce co-doped $Lu_3Al_5O_{12}$ epitaxial layers for scintillators.* Journal of Crystal Growth, 2011. **318**(1): p. 813-819.

Prusa, P., M. Kucera, J.A. Mares, M. Nikl, K. Nitsch, M. Hanus, Z. Onderisinova, and T. Cechak, *Scintillation properties of Sc-, Pr-, and Ce-doped LuAG epitaxial garnet films.* Journal of Crystal Growth, 2011. **318**(1): p. 545-548.

Kucera, M., M. Nikl, M. Hanus, Z. Onderisinova, and A. Beitlerova, *Growth, Emission and Scintillation Properties of Tb-Sc Doped LuAG Epitaxial Films.* Ieee Transactions on Nuclear Science, 2012. **59**(5): p. 2275-2280.

Kucera, M., M. Nikl, M. Hanus, and Z. Onderisinova, *Gd3+ to Ce3+ energy transfer in multi-component GdLuAG and GdYAG garnet scintillators* Physica Status Solidi-Rapid Research Letters, 2013. **7**(8): p. 571-574.

Prusa, P., M. Kucera, M. Hanus, J.A. Mares, A. Beitlerova, Z. Onderisinova, and M. Nikl, *Scintillation properties of the Ce-doped multicomponent garnet epitaxial films.* Optical Materials, 2013. **35**(12): p. 2444-2448.

Kucera, M., M. Hanus, Z. Onderisinova, P. Prusa, A. Beitlerova, and M. Nikl, *Energy transfer and scintillation properties of Ce3+ doped*

(LuYGd)3(AlGa)5O12 multicomponent garnets. Ieee Transactions on Nuclear Science, 2014. **61**(1): p. 282 - 289.

Onderisinova, Z., M. Kucera, M. Hanus, and M. Nikl, *Temperature-dependent nonradiative energy transfer from Gd3+ to Ce3+ ions in co-doped LuAG:Ce, Gd garnet scintillators.* Journal of Luminescence, 2015. **167**: p. 106-113.

Prusa, P., M. Kucera, J.A. Mares, Z. Onderisinova, M. Hanus, V. Babin, A. Beitlerova, and M. Nikl, *Composition Tailoring in Ce-Doped Multicomponent Garnet Epitaxial Film Scintillators.* Crystal Growth & Design, 2015. **15**(8): p. 3715-3723.

Kucera, M., Z. Onderisinova, J. Bok, M. Hanus, P. Schauer, and M. Nikl, *Scintillation response of Ce3+ doped GdGa-LuAG multicomponent garnet films under e-beam excitation.* Journal of Luminescence, 2016. 169: p. 674-7

Other publications

Hlásek, T., K. Rubešová, V. Jakeš, P. Nekvindová, J. Oswald, M. Kučera, and M. Hanuš, *Influence of gallium on infrared luminescence in Er3+ doped Yb3Al5−yGayO12 films grown by the liquid phase epitaxy*. Journal of Luminescence, 2015. **164**: p. 90-93.